Defence Forces Technical Research Centre
Puolustusvoimien Teknillinen Tutkimuslaitos
Publications 8

TOOLS AND METHODS FOR RADAR PERFORMANCE EVALUATION AND ENHANCEMENT

Jukka Ruoskanen

Dissertation for the degree of Doctor of Science in Technology to be presented with due permission for public examination and debate in Auditorium S4 at Helsinki University of Technology (Espoo, Finland) on the 21st of October 2005 at 12 o'clock noon.

Helsinki University of Technology
Department of Electrical and Communications Engineering
Applied Electronics Laboratory

Teknillinen Korkeakoulu
Sähkö- ja tietoliikennetekniikan osasto
Sovelletun elektroniikan laboratorio

RIIHIMÄKI 2005

Cover desing:
Pirjo Laurimaa
Jukka Ruoskanen

ISBN 951-25-1600-4
ISSN 1457-3938
Defence Forces Technical Research Centre
Puolustusvoimien Teknillinen Tutkimuslaitos

Edita Prima Oy
Helsinki 2005

Preface

This thesis work has been carried out at Electronics- and information technology section of Finnish Defence Forces Technical Research Centre during years 2001-2005. The research work started out as an evaluation project concerning the feasibility of millimeter wave band for radar applications. It was soon found out, that although open literature contained some reports of clutter and target behaviour at millimeter wave frequencies, very little, if any, of those reports were directly applicable to Scandinavian environment. Therefore a measurement campaign of our own was started.

I wish to thank Professor Pekka Eskelinen for his endlessly innovative work concerning the development and construction of test instrumentation radars and related equipment, without which this work would not have been completed. Also his encouragement and constructive critisism throughout the work have improved the quality of this thesis.

I would also like to thank all my co-workers and colleagues who gave valuable assistance in many practical arrangements and tasks during the thesis work. Numerous succesfull measurement days out in the field would not have been possible without the help of Heikki Heikkilä, Mika Ilvesmäki, Kari Järvinen, Jouni Peltonen, Raimo Jääskeläinen, Leif Holmström, Arvi Serkola and Liisa Terho from FDF and Markku Nieminen and Tero Kiuru from HUT/IDC.

I greatly appreciate the efforts of the pre-examiners of this work, Dr. Edgar Schmidhammer and Dr. Mikko Kuisma, whose valuable comments and suggestions improved this thesis in many ways.

I have received personal research grant for this thesis from The Foundation of Technology (TES), which is warmly appreciated.

I want to thank my parents, who have been very encouraging and supportive throughout my studies. Finally, and especially, I want to thank my lovely fiancée Krista for her care and patience during this work. The true summits of our lives still await us!

Riihimäki, July 20th, 2005

Jukka Ruoskanen

Abstract

The purpose of this thesis has been to create tools for radar performance estimation in true operational environments and to evaluate the feasibility of millimeter wave band for radar applications. Radar wave propagation and backscattering was studied in different environments using real radar data obtained from field measurement campaigns.

Measurement results of radar clutter in typical illumination geometries encountered using a ground-based radar are presented for K_a- and V-band. The low grazing angle ($<5°$) clutter backscattering measurements as well as measurements at perpendicular incidence presented in this work are completely new results, for which comparisons can not be found in open literature. For example, the snow covered ground backscattering coefficient at V-band was found to be on average 12 dB larger than at K_a-band. Additionally, new volumetric backscattering coefficients of rain and snow at K_a-band are given. Also new spectral dependency values for vegetation clutter spectrum at K_a-band are proposed. The cross-over level from Gaussian low-frequency components to Lorentzian high-frequency components for vegetation clutter, according to our measurements, is 5 dB higher than what was previously reported.

Phenomena related to radar wave propagation are discussed and new measurement results concerning clear sky backscattering variations due to meteorological inversion layer are presented. A lens-effect theory proposed by Schneider (1998) is verified to be valid also in connection to long radar ranges up to 3 kilometers and for successive concave and convex terrain profiles. Furthermore, this thesis addresses several details concerning arranging and conducting practical radar measurements in true operational environments, including calibration issues and definition of antenna beamwidth in clutter measurements. A 1.2 dB uncertainty has been achieved in practical field measurements of clutter and target backscattering. Also a novel and easy-to-use approach for radar pulse width optimization has been introduced, taking into account the effect that radar receiver bandwidth has on thermal noise floor and the pulse width to the effective clutter cell area or volume. For example, for rain clutter volumetric backscattering coefficient of $\eta = 5 \cdot 10^{-4}$ m^2/m^3 and target RCS of 100 m^2, the optimal pulse width is found to be 150 ns and the corresponding maximum radar range is 5700 m.

The new measurement results presented in this work provide tools for developing of signal processing algorithms for millimeter wave radar. Several practical tools and methods for radar performance estimation have been given, and new observations of backscattering and radar wave propagation are reported.

List of Publications

This thesis is based on the work presented in the following papers:

[P1] J. Ruoskanen, P. Eskelinen, H. Heikkilä, M. Nieminen, A. Serkola and J. Peltonen, "Millimeter Wave Backscattering Experiments in Arctic Winter", *Proceedings of the* 33^{rd} *European Microwave Conference*, Munich, Germany, Oct. 2003, pp. 1159-1162.

[P2] J. Ruoskanen, P. Eskelinen and H. Heikkilä, "Millimeter Wave Radar with Clutter Measurements", *IEEE Aerospace and Electronic Systems Magazine*, Vol. 18, No 10., October 2003, pp. 19-23.

[P3] J. Ruoskanen, P. Eskelinen and H. Heikkilä, "Target Detection Trials with A Millimeter Wave Radar System", *IEEE Aerospace and Electronic Systems Magazine*, Vol. 18, No. 11, November 2003, pp. 26-30.

[P4] J. Ruoskanen, P. Eskelinen, H. Heikkilä and A. Serkola, "Pulse Width Considerations for a Short Range Millimeter Wave Radar", *IEEE Aerospace and Electronic Systems Magazine*, Vol. 19, No. 1, January 2004, pp. 14-17.

[P5] H. Heikkilä, P. Eskelinen, J. Ruoskanen and P. Hautala, "Upgrading Armored Vehicle Sensor Systems", *IEEE Aerospace and Electronic Systems Magazine*, Vol. 19, No. 1, January 2004, pp. 26-31.

[P6] J. Ruoskanen, P. Eskelinen and H. Heikkilä, "A Light Weight Q-Band Millimeter Wave Radar Master Oscillator", *Proceedings of the European Frequency and Time Forum 2004*, Surrey, United Kingdom, April 2004, 4 p.

[P7] J. Ruoskanen, P. Eskelinen, H. Heikkilä, P. Kuosmanen and T. Kiuru, "A Practical Millimeter Wave Radar Calibration Target", *IEEE Antennas and Propagation Magazine*, Vol 46, No. 2, April 2004, pp. 94-97.

[P8] J. Ruoskanen, P. Eskelinen and H. Heikkilä, "HF radio as a way to synchronize a multistatic radar network", *Proceedings of the 7th Nordic HF Conference*, Växjo, Sweden, August 2004, pp. 7.1.1-7.1.6.

[P9] J. Ruoskanen, P. Eskelinen, H. Heikkilä and A.Serkola, "Ka- and V-Band Clutter Measurements at Grazing Angle Extremes", *Proceedings of the European Radar Conference*, Amsterdam, Netherlands, October 2004, pp. 325-328.

[P10] J. Ruoskanen, P. Eskelinen and H. Heikkilä, "Measuring the Frequency Stability of Mobile Radar Oscillators", *Proceedings of the IEE International Radar Conference 2004*, Toulouse, France, October 2004, 5 p.

[P11] P. Eskelinen, J. Ruoskanen, H. Heikkilä, "Millimeter Radar Propagation Measurements in Long Road Canyons", accepted for publication in *Proceedings of International Radar Symposium 2005*, Berlin, Germany, September 2005.

The author's contribution in [P1 - P11] has been as follows:

Paper [P1] is a result of lenghty collaborative work. The test instrumentation was mainly designed and constructed by Professor Eskelinen, with assistance of Mr. Peltonen, LtCol (eng) Serkola and the author. The measurements were jointly conducted by the author and Professor Eskelinen. Data analysis was performed by the author. The manuscript was written jointly by the author and Professor Eskelinen.

Paper [P2] was mainly contributed by the author. Professor Eskelinen supervised the research work and assisted in writing the manuscript.

Paper [P3] was mainly contributed by the author. Professor Eskelinen supervised the data analysis work and the writing of the manuscript.

Paper [P4] is mainly contributed by the author and Professor Eskelinen. LtCol (eng) Serkola and Maj (eng) Heikkilä assisted during the practical field measurement phase.

Paper [P5] is a result of collaborative work. The author was responsible for the radar signal measurements and analysis. Dr. Kuosmanen and Maj (eng) Heikkilä designed the acceleration measurements with assistance of Professor Eskelinen and the author. The manuscript was written by Maj (eng) Heikkilä, the author and Professor Eskelinen.

Paper [P6] is a result of collaborative work. The oscillator measurements were conducted by Professor Eskelinen and the author. Maj (eng) Heikkilä assisted in practical details concerning the field measurements. The author was responsible for writing the manuscript.

Paper [P7] is a result of collaborative work. The calibration target was designed by Professor Eskelinen and the author. Maj (eng) Heikkilä and Mr. Kiuru assisted in mechanical details. The manuscript was written by the author and Professor Eskelinen.

Paper [P8] was mainly contributed by the author.

Paper [P9] was mainly contributed by the author. Professor Eskelinen, Maj (eng) Heikkilä and LtCol (eng) Serkola assisted in field measurements. Professor Eskelinen supervised the writing of the manuscript.

Paper [P10] is a result of collaborative work. The test arrangements were designed and the measurements were conducted by the author and Professor Eskelinen. Maj (eng) Heikkilä assisted in developing the field measurement set-up. The author was responsible for data analysis and writing the manuscript. Professor Eskelinen supervised the data analysis work and the writing of the manuscript.

Paper [P11] is a result of collaborative work. The paper was written and radar measurements were conducted by the author and Professor Eskelinen.

Contents

Symbols

a	scaling coefficient
	height of a rectangular plate [m]
a_t	non-fluctuating target amplitude [V]
a_1	experimentally determined constant
A	physical area [m^2]
A_c	illuminated area [m^2]
b	width of a rectangular plate [m]
B_n	noise bandwidth of a receiver [Hz]
c	speed of light [m/s]
$C(x)$	Fresnel cosine integral
C/N	clutter-to-noise ratio
D	largest dimension of an antenna [m]
E	electrical field strenght [V/m]
E_0	radiated electrical field strenght [V/m]
E_d	incident electrical field strenght of direct path [V/m]
E_r	incident electrical field strenght of reflected path [V/m]
f	frequency [Hz]
f_c	center frequency of a radar [Hz]
f_D	Doppler frequency [Hz]
f_G	gaussian corner frequency [Hz]
f_L	Lorentzian corner frequency [Hz]
F	noise figure,
	propagation factor
F_r	propagation factor on a path between target and receiver
F_t	propagation factor on a path between transmitter and target
$g(\theta)$	antenna beam shape weighting function
g_3	skewness
g_4	kurtosis
G	gain of an antenna
G_r	gain of a receiving antenna
G_t	gain of a transmitting antenna
G_0	maximum gain of an antenna
h_r	height of a radar antenna from the ground [m]
h_{rms}	root mean square of the surface height irregularity [m]
h_t	height of a target from the ground [m]
$h(t)$	impulse response
i	general index
I	total number of resolution steps
I_0	modified Bessel function of zero order
k	wave number [1/m]

k_B	Boltzmann constant ($= 1,38066 \times 10^{-23}$ JK^{-1})
k_i	imaginary part of wave number [1/m]
k_r	real part of wave number [1/m]
L	largest target dimension [m],
	bistatic radar baseline lenght [m]
L_{atm}	two-way atmospheric attenuation
L_x	general attenuation factor
m	number of samples in a single histogram bin
M	number of samples in the input to correlator
$M_q(x)$	q-th moment about the mean
n	number of pulses
	Lorentzian exponent
n_i	number of samples in i-th bin of a discrete data set
N	number of samples
$p(t)$	pulse shape weighting function
P_d	probability of detection
P_{fa}	probability of false alarm
P_i	incident power on target [W]
P_{in}	detector input power [W]
P_{min}	minimum detectable target echo [W]
$P_n(\theta, \varphi)$	normalized radiated power density of an antenna in spherical coordinates
P_r	received power [W]
P_t	transmitted power [W]
$Q(\alpha, \beta)$	generalized 1^{st} order Marcum Q-function
r	radius of a circle or sphere [m]
r_L	lens factor
R	radar range [m]
R_d	range from radar to taget via direct signal path [m]
R_{far}	far-field range [m]
R_L	radius of local curvature of ground [m]
R_{max}	maximum radar range [m]
R_{opt}	radar range corresponding to the optimal pulse width [m]
R_r	range from target to receiver in a bistatic radar configuration [m],
	range from radar to target via reflected signal path [m]
R_t	range from transmitter to target in a bistatic radar configuration [m]
R_T	transition range [m]
$S(x)$	Fresnel sine integral
S/C	signal-to-clutter ratio
S/N	signal-to-noise ratio
$(S/N)_{min}$	minimum allowed target signal-to-noise ratio
S_r	received power density [W/m^2]
t	time [s]
T_0	reference temperature (290K)
T_{ant}	antenna noise temperature [K]
T_{sys}	system noise temperature [K]
u	video voltage [V]

u_D	detector voltage [V]
U_{out}	video voltage at detector output [V]
U_T	threshold voltage [V]
v_D	Doppler velocity [m/s]
W_0	spectral power density at zero
$W(f)$	spectral power density
x	integration constant
$\bar{x}$	mean value
x_i	individual sample of measured data set
α	attenuation coefficient [1/m]
	argument of Marcum Q-function
	inverse of antenna beam shape correction factor
β	phase constant [1/m],
	bistatic angle
	argument of Marcum Q-function
Γ	total power reflection coefficient
$\delta(t)$	delta function
ϵ	permittivity [As/Vm]
ϵ_r	relative dielectric constant
ϵ_0	permittivity of vacuum ($= 8,85419 \times 10^{-12}$ As/Vm)
ζ	integration variable
η	volumetric scattering coefficient [m^2/m^3]
η_r	antenna efficiency
θ	off-zenith elevation angle in spherical coordinate system
θ_R	north-referenced target azimuth angle from receiving site
θ_T	north-referenced target azimuth angle from transmitting site
$\theta_{1.5dB}$	1.5 dB beamwidth of an antenna main beam
θ_{3dB}	3 dB beamwidth of an antenna main beam
$\theta_{3dB,az}$	3 dB beamwidth of an antenna main beam in azimuthal direction
λ	wavelength [m]
μ	permeability [Vs/Am]
ρ_s	specular reflection coefficient
ρ_F	Fresnel reflection coefficient
σ	monostatic radar cross section [m^2]
σ_b	radar cross section of the background echo [m^2]
σ_{bi}	bistatic radar cross section [m^2]
σ_c	radar cross section of the calibration target[m^2]
σ_{far}	monostatic radar cross section in far-field conditions [m^2]
σ_{meas}	measured radar cross section [m^2]
σ_s	conductivity [1/Ωm]
σ^0	scattering coefficient [m^2/m^2]
τ	radar pulse width
ϕ	grazing angle
Φ	phase angle
φ	azimuth angle in spherical coordinate system
Ψ^2	variance of noise voltage

ω	angular frequency [rad/s]
Ω	solid angle [sr]

Abbreviations

BSS	Backscattering Simulation Software (commercial trade name)
CAD	Computer aided design
CW	Continuous wave
CFAR	Constant false alarm rate
COHO	Coherent oscillator
DC	Direct current
DRO	Dielectric resonator oscillator
DSP	Digital signal processing
DVD	Digital versatile disc
ESM	Electronic support measures
FFT	Fast Fourier transform
FGAN	Forschungsgesellschaft für Angewandte Naturwissenschaften
FMCW	Frequency modulated continuous wave
FSK	Frequency shift keying
IF	Intermediate frequency
ITU-R	International Telecommunication Union - Radiocommunication sector
I/Q	In-phase/quadrature-phase
KREMS	Kiernan Re-entry Measurement Site
LNA	Low noise amplifier
LO	Local oscillator
LPI	Low probability of intercept
MB	Mega byte
MTI	Moving target indication
PC	Personal computer
pdf	Probability density function
PIN diode	Positive-Intrinsic-Negative diode
PPI	Plan position indicator
PRF	Pulse repetition frequency
RCS	Radar cross section
RF	Radio frequency
RPC	Reflected power canceller
RT	Transceiver
Rx	Receiver
SAR	Synthetic aperture radar
STALO	Stable local oscillator
SWR	Standing wave ratio
TDOA	Time-difference-of-arrival
TE	Transverse electric mode
TM	Transverse magnetic mode
T/R	Transmit/receive

TTL	Transistor-to-transistor logic
Tx	Transmitter
UAV	Unmanned aerial vehicle
UHF	Ultra high frequency

Radar frequency bands

L-band	1-2	GHz
S-band	2-4	GHz
C-band	4-8	GHz
X-band	8-12	GHz
K_u-band	12-18	GHz
K-band	18-27	GHz
K_a-band	27-40	GHz
V-band	40-75	GHz
W-band	75-110	GHz

1 Introduction

A century has passed since Christian Hülsmeyer's patent application for the Telemobiloskop on 30^{th} April 1904 [1, p. 8]. The radar engineering community has come a long way from the *"Herzian-wave Projecting and Receiving Apparatus"* to design and construct highly sophisticated and complex radar systems, each specifically tailored to serve the desired purpose. The field of radar engineering grew rapidly during and especially after the World War II [2]. Since then the majority of all ground-based, maritime and airborne radars have operated at S-, C- or X-band with an exception of a small group of special purpose radar systems at UHF-region and at lower end of the K-band. Although the focus of most of the work done on radar technology has always been on microwave frequencies, the research and development of millimeter wave radar started already more than 50 years ago. At millimeter wave frequencies a very good angular resolution can be achieved with a small antenna aperture, and due to the feasible wide bandwidths the range resolution is realizable up to the order of centimeters [3, pp. 36-40]. Furthermore, the tolerance against electronic countermeasures is increased in a millimeter wave radar. Despite the evident advantages of higher frequencies the number of applications suited for millimeter wave radar are limited due to the challenges in generation and radiation of high power, as well as the increased atmospheric gaseous and hydrometeor attenuation of radar signal in comparison with conventional microwave frequencies. However, if we consider the relatively small sizes of RF components and antenna dimensions at millimeter wave frequencies it becomes clear that a millimeter wave radar is an interesting option for applications where the small size and weight of the radar hardware is desired, such as on board small-scale moving platforms or for portable solutions.

1.1 Civilian and military millimeter wave radars

Millimeter wave radars are employed in a wide range of applications for commercial, military and scientific purposes. They are used in connection to different modes of operation, such as in remote sensing, safety and measurement applications. In industrial use the millimeter wave sensors are often superior to infrared sensors due to the ability to penetrate fog, smoke and other obscurants. Some of the most commonly used millimeter wave systems include:

- Automobile Collision Warning sensor
- Altimeters and various height/depth measurements in hostile environments
- Speed and range measurement
- Intrusion detection
- Aircraft collision warning/obstacle detection system for helicopters and UAVs
- Imaging applications
- Cloud- and scattering radars and other meteorological purposes
- Motion sensors for automated systems

The research of vehicular radar started in the 1970's but it was not until mid 1990's when the developments in millimeter wave component technology enabled the automobile industry to introduce small vehicular radars in their cars to perform anticollision and adaptive cruise control functions [4, pp. 263-267]. Some of the early solutions were based on laser technology, but they were gradually abandoned due to the problems caused by weather conditions and dirty cars. Most of the manufacturers have chosen a frequency band in the vicinity of 76 GHz and an FMCW waveform for their radars allowing for precise doppler shift- and range measurements and easier installation of the device into the limited space available in the vehicle.

One of the largest known millimeter wave radars is one of the KREMS radars on Roi-Namur Island [5, 6]. It performs imaging and tracking of ballistic missiles as well as provides information of space debris for the Space Object Identification group. The radar was built by Lincoln Laboratory in collaboration with University of Massachusetts, Radio Corporation of America and Raytheon. The antenna diameter of this huge radar is 13,7 m and it is a dual frequency device, transmitting peak powers of 60 kW at 35 GHz and 1,6 kW at 95,48 GHz. Apart from this US Army operated radar other known operational millimeter wave radars in military use have not been described in the open literature very accurately. Perhaps the most well known military millimeter wave radar is a joint venture of Lockheed Martin and Northrop Grumman called Longbow Fire Control Radar (AN/APG-78), installed on the US Army's Apache AH-64D attack helicopter [7, 8]. The radar antenna, protected with a radome, is mounted atop of the helicopter main rotor. The radar has several modes of operation and it employs highly sophisticated data and signal processing methods. The maximum detection range is 10 km.

Sensor solutions involving the use of millimeter wave radar on ground operating armoured military vehicles have emerged recently. US Army Research laboratory and Northrop Grumman have experimented with a K_a-band radar installed into a M1A2 Abrams battle tank [9]. The radar's main tasks are battlefield identification and surveillance and to establish communication link between ground vehicles. These tasks are achieved by using four active electronically scanned arrays, one at each side of the tank. Dutch Army has an integrated Radar and Fire Control System installed into a Leopard tank to provide scanning and tracking for the anti-aircraft system [10, Ch. 7]. The system consists of X- and K_a-band radars, which both use the same parabolic antenna for transmission and receiption. The same concept is also being used in Dutch naval ships. Russian Khrizantema AT-15 is an anti-tank missile system using laser- and millimeter wave radar homing [11, 12]. The system is installed into a modified BMP-3 infantry combat vehicle chassis and the radar is capable of guiding the missile up to 6 km.

1.2 Scope and contents of this thesis

The scope of the studies presented in this thesis has been to create tools and methods to evaluate the feasibility of millimeter wave band for radar applications. In this thesis the evaluation methods and new observations concerning millimeter wave propagation and scattering close to surface are summarized. Several different instrumentation radars were designed and constructed during the research, because the emphasis has been on real field

experiments and empirical tests, resulting from the desire to use true millimeter wave radar data rather than simulations.

After this short introduction, in Chapter 2 the theoretical basics of radar and radar signal processing are discussed and different main types of radars are presented. In Chapter 3 the developed V-band test radar is presented and some interesting design outlines are discussed including calibration issues. The backscattering measurements of millimeter wave radar signals in Scandinavian environment are presented in Chapter 4. Measured examples of target RCS values are given in Chapter 5 together with discussion of RCS behaviour at millimeter wave frequencies. Chapter 6 discusses the suitability of well known radar signal processing methods to millimeter wave radars. Summary of publications is given in Chapter 7 and conclusions in Chapter 8.

1.3 New scientific results

The work presented in this thesis has produced new knowledge in the following areas:

1) The feasibility of a compact millimeter wave radar has been demonstrated in true environmental conditions.

2) Several hardware solutions have been evaluated in conjunction with practical field measurements.

3) Results of completely new backscattering measurements of soil, vegetation and snow at V-band are presented.

4) New results of K_a-band backscattering measurements of soil, vegetation and snow at extremely small and large grazing angles are presented.

5) New rain and snowfall backscattering measurement results are presented at K_a-band. Completely new radar signal attenuation and backscattering measurement results from explosions of shaped charges are presented.

6) Measurement results showing an unknown phenomenon of variations in clear-sky backscattering of millimeter wave radar signal in correlation with the existence of a low level inversion layer in the atmosphere are presented.

7) A novel and easy-to-use approach for radar pulse width optimization has been introduced.

8) Results of measurements aimed to verify a special radar signal propagation phenomenon called ”lens-effect” presented in open literature are shown and discussed. The suggested theory is shown to be valid and has been extended to cover long radar ranges and multiple successive concave and convex portions of terrain profile.

2 Theoretical fundamentals of radar

2.1 General radar theory

Radar transmits electromagnetic energy into its surrounding environment through a radiating element. The radiated electromagnetic waveform is scattered by objects in the volume within the radar coverage, and the backscattered energy is captured with the same (monostatic operation) or with separate (bistatic operation) radiating element. The main task of a traditional radar is to detect the presence of nearby objects, to determine their range, bearing angle and possible radial velocity [13, Ch. 1]. In case of moving objects the radar might also perform tracking, classification and priorization of detected targets [14]. The amplitude characteristics of the echoes together with Doppler- and polarization fingerprints provide information with which the operator and the data processor, or more often the data processor alone, can make the decision concerning detection and classification of the object in question.

2.1.1 Radar equation

The radar antenna gain compared to an isotropic radiating element is calculated with

$$G = \frac{\eta_r 4\pi}{\iint_\Omega P_n(\theta,\varphi)d\Omega} \quad ; \quad d\Omega = sin\theta d\theta d\varphi, \tag{2.1}$$

where $P_n(\theta,\varphi)$ is the normalized radiated power density of an antenna in spherical coordinates and η_r is the antenna efficiency, a single parameter that includes all unidealities of the antenna such as surface accuracy, profile accuracy and illumination efficiency [15, pp. 813-815]. Surface accuracy is a measure of the RF smoothness of the reflecting surface, and profile accuracy describes how closely the shape of the reflecting element approximates the optimal shape designed for the antenna. Illumination efficiency includes the problems with the antenna feed pattern optimization, like possible overspilling issues and edge tapering effects when trying to achieve uniform illumination of the reflecting aperture. The supporting structures of the feed also reduce the effective collecting area of the antenna [16, pp. 312-316]. Typically the antenna efficiency values for a parabolic dish at millimeter wave frequencies are in the order of 0.5 - 0.6 [17, pp. 512-513]. For a parabolic antenna with one feed the gain can be approximated with

$$G = \eta_r \frac{4\pi A}{\lambda^2} = \eta_r \left(\frac{\pi D}{\lambda}\right)^2, \tag{2.2}$$

where A is the physical area of the antenna, D its largest dimension and λ the wavelength. The power density of the transmitted and backscattered radar signal at the monostatic radar antenna location is

$$S_r = \left(\frac{P_t G_t}{4\pi R^2}\right)\left(\frac{\sigma}{4\pi R^2}\right), \tag{2.3}$$

where P_t is the transmitted power, G_t the gain of transmitting antenna, R radar range and σ the radar cross section (RCS) of the backscattering object [18, Ch. 1]. The RCS represents the effective area with which the object captures and isotropically reradiates the incident power. The radar captures the backscattered power with an antenna having effective aperture $\eta_r A$, which can be expressed in terms of the receiver antenna gain (Eq. 2.2). Now the basic monostatic ($G_t = G_r = G$) radar equation can be written in the form

$$P_r = S_r \cdot \eta_r \cdot A = \frac{P_t G^2 \lambda^2 \sigma}{(4\pi)^3 R^4}. \tag{2.4}$$

In order to be able to estimate the maximum detection range of a radar several additional factors must be considered. The minimum detectable signal power at the input of the radar receiver has to be known. It is a function of the smallest allowable signal-to-noise ratio of the target return echo $(S/N)_{min}$ and the noise figure of the system. The minimum signal power for the target echo can be calculated with

$$P_{min} = k_B T_{sys} B_n (S/N)_{min} = k_B (T_{ant} + (F-1)T_0) B_n (S/N)_{min}, \tag{2.5}$$

where T_{sys} is the system and T_{ant} the antenna noise temperature [19, Ch. 5]. The relation between T_{sys} and T_{ant} is only valid in case a perfect matching of antenna and receiver front-end impedances is assumed. F and B_n are the noise figure and the noise bandwidth of the receiver, respectively. The required signal-to-noise ratio depends on the signal processing methods utilized in the radar system. The amount of individual pulses that are integrated and the methods with which the integrations are performed effect the required signal-to-noise ratio in a complex way. The fluctuations in the RCS of the backscattering object combined with the several types of losses in the RF signal path further complicate the prediction analysis of radar range. For one single pulse the radar range equation in its simple form, having $P_r = P_{min}$, becomes [20, Ch. 3]

$$R_{max} = \left[\frac{P_t G^2 \lambda^2 \sigma}{(4\pi)^3 k_B T_{sys} B_n (S/N)_{min} L_{atm} L_x} \right]^{\frac{1}{4}}, \tag{2.6}$$

where the loss factor L_{atm} is the two-way attenuation of the radar signal due to propagation through lossy medium and L_x includes all other lossess that are significant to the calculation of maximum range.

2.1.2 Propagation

At millimeter wave frequencies the attenuation caused by molecule resonance of atmospheric gases is significantly larger than at lower frequencies. The clear air attenuation is mainly due to oxygen and water vapor molecules, which especially at the vicinity of their characteristic resonance frequencies absorb and reradiate the signal energy. This atmospheric attenuation is a function of air temperature, air pressure and the molecule content of the atmosphere. The amount of water vapor has the strongest effect on the variations of the attenuation value, since the quantities of other gases remain very stable and have very well known altitude profile [21, p. 7]. The semi-empirical model based on spectroscopic parameters of oxygen and water vapor absorption lines by ITU-R provides

means for calculation of atmospheric attenuation [22]. The resonance frequencies are ideally thin and discrete absorption lines due to the quantized nature of the absorption process, but as a result of collisions of the molecules the absorption lines tend to spread and merge into a one single absorption belt [23]. This happens for example for oxygen molecules resonating at frequencies between 50 GHz and 70 GHz. At higher altitudes where the air pressure is low, there is a smaller concentration of oxygen molecules, leading to fewer interactions between the molecules and the electromagnetic wave. With the occurrence of fewer collisions, individual resonance frequencies are distinguishable and result in a smaller total attenuation. On the other hand the high concentration of molecules at the sea level leads to a high rate of interactions between the oxygen molecules and the electromagnetic wave as well as increases the interaction between individual oxygen molecules. Due to the high concentration of molecular collisions, the individual resonance frequencies are not distinguishable any more. Instead, the width of the lines overlaps and causes higher total attenuation [24]. The sea-level attenuation plot at frequencies between 50 - 70 GHz appears broad and smooth (Fig. 2.1).

The radar signal at millimeter wavelengths interacts also with larger airborne particles, such as rain droplets, snow flakes, ice crystals and dust. These particles absorb and scatter the energy of the wave. The absorption attenuation of the signal by a lossy medium can be estimated by introducing a complex dielectric constant into the expression of wave

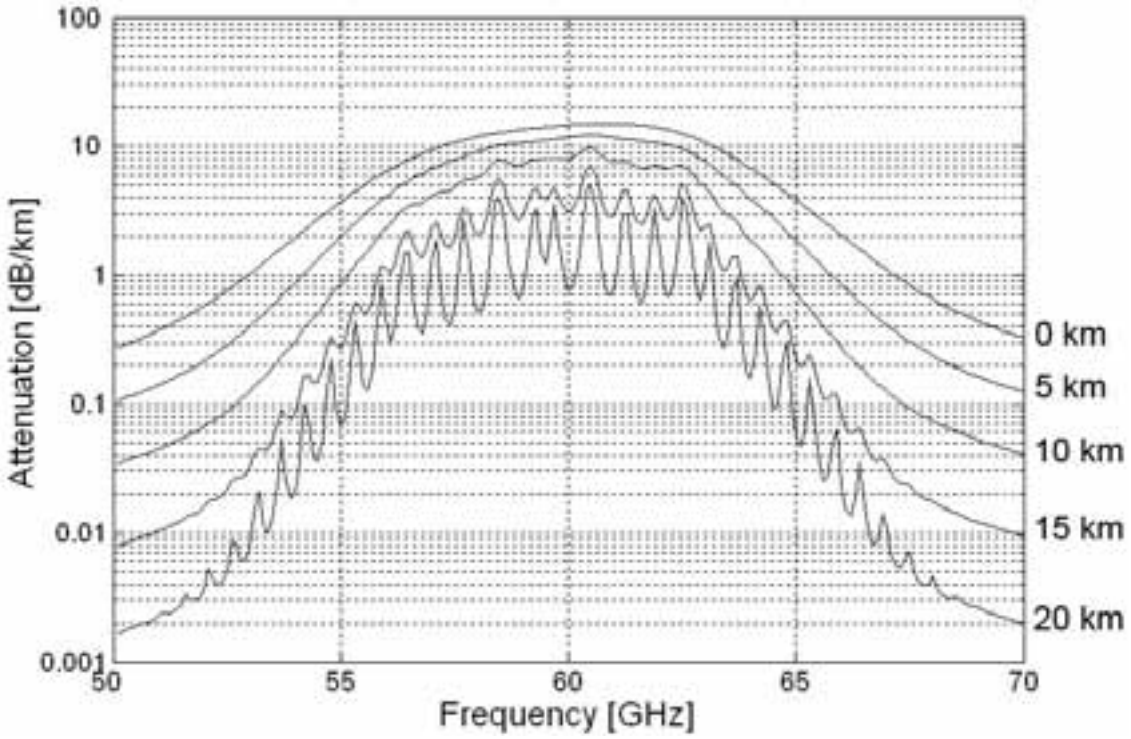

Figure 2.1: *Atmospheric attenuation at frequencies 50-70 GHz computed with the ITU-R model [22]. The graphs from topmost curve downwards represent the altitudes of 0, 5, 10, 15 and 20 km above sea level.*

number:

$$k = k_r + jk_i = \beta - j\alpha = Re\left\{\omega\sqrt{\mu\epsilon}\right\} + jIm\left\{\omega\sqrt{\mu\epsilon}\right\}, \tag{2.7}$$

where

$$\epsilon = \epsilon_r\epsilon_0 - j\frac{\sigma_s}{\omega}. \tag{2.8}$$

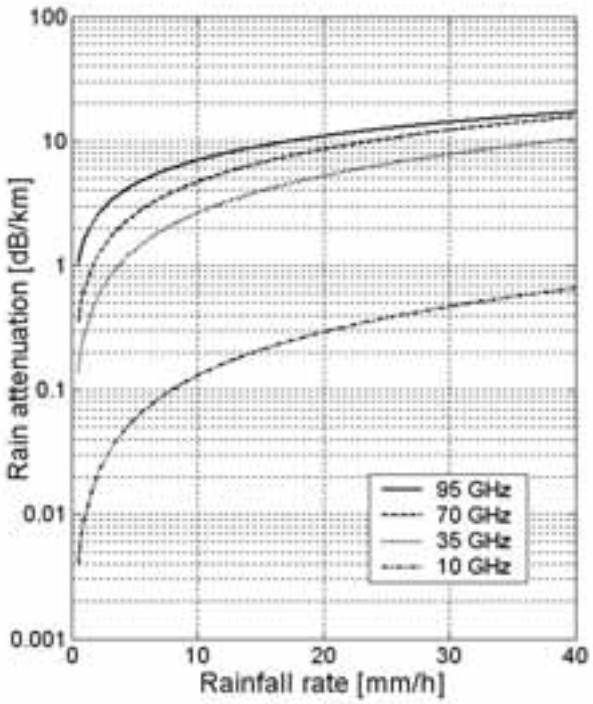

Figure 2.2: *Rain attenuation model as a function of rainfall rate at four frequencies calculated with the model presented in [25].*

The imaginary part of the wave number represents the attenuation (α) and it is usually given in units of dB/km. However, the orientations and dielectric properties as well as the size distributions and densities of the particles are usually difficult to estimate reliably. Therefore most of the mathematical expressions of different hydrometeor attenuations are empirical models derived from real radar measurements and they usually are power law functions that best fit the collected attenuation data. One example of such rain attenuation functions is a model created as a result of three individual measurement campaigns presented in [25]. The rain attenuation for four frequencies as a function of rainfall rate based on the model is plotted in Fig. 2.2.

The complex permittivity, and therefore also the reflection coefficient, of soil varies slightly as a function of frequency. The reflection coefficient of different types of soil is also affected by the roughness of the surface as well as by the instantaneous moisture content and vegetation cover of the specific area [26, pp. 285-287]. If we assume a relatively flat surface illuminated at very low grazing angles ($\phi < 2°$), the power reflection coefficient of most typical soil and other types of surfaces is approximately one with the electric field experiencing a phase change of 180°, regardless of the slight local variations of dielectric properties of the soil substance. This approximation is valid for vertical and horizontal polarizations as can be seen from Fig. 2.3, where the power reflection coefficients are calculated using Fresnel reflection coefficient equations [27, p. 302]. The radar waves scattered from a rough surface undergo phase and amplitude changes which results in a reflected field that consists of specular and diffuse components. The ideal smooth surface reflection coefficient is diminished by specular scattering coefficient, which according to [28, p. 85] is a function of standard deviation of the surface height irregularity (h_{rms}) and grazing angle (ϕ), and is given by

$$\rho_s = \exp\left[-\left(\frac{4\pi h_{rms}}{\lambda}\sin\phi\right)^2\right]. \tag{2.9}$$

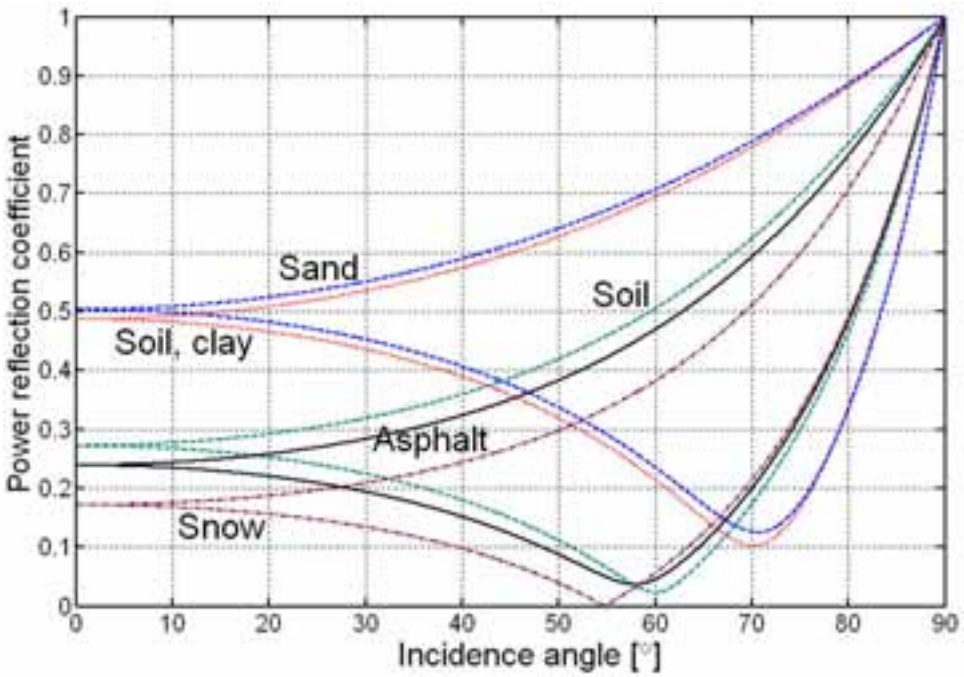

Figure 2.3: *The power reflection coefficient of different ground types as a function of incidence angle of the wavefront for an ideal smooth surface. The upper curve in each of the curve pairs represents the TE-mode and the lower the TM-mode.*

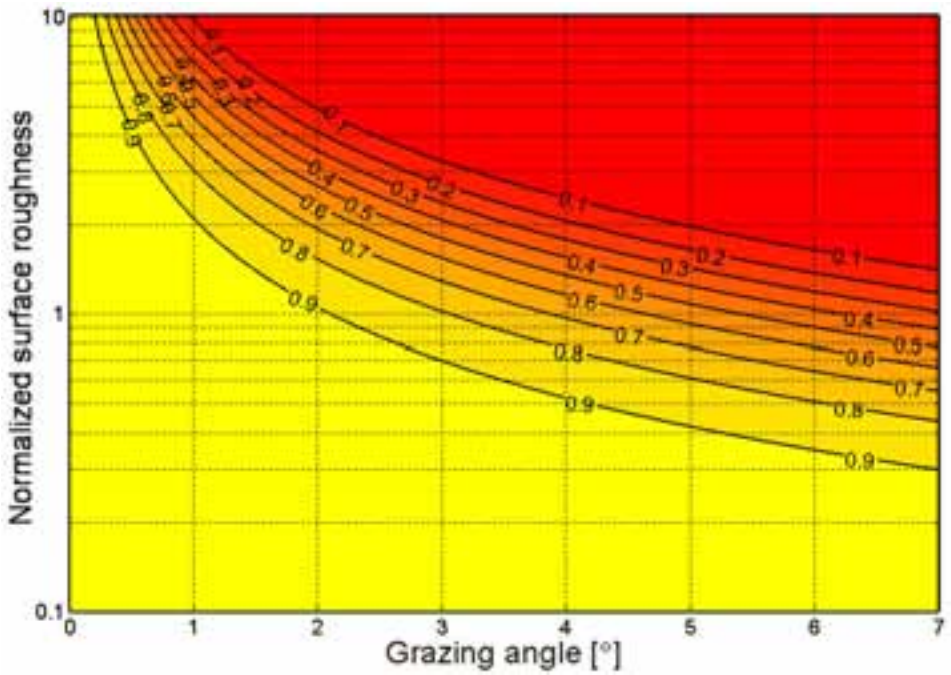

Figure 2.4: *The specular reflection coefficient as a function of grazing angle and normalized surface roughness (h_{rms}/λ) calculated from Eq. 2.9. For example, when the normalized surface roughness is 1 and the grazing angle is 2°, the specular reflection coefficient is 0.9.*

The behaviour of this coefficient is plotted in Fig. 2.4, where the contour lines represent the value of the specular reflection coefficient. The total surface power reflection is a product of two factors: the square of the magnitude of Fresnel reflection coefficient and the square of the magnitude of specular reflection coefficient ($\Gamma_{(h,v)} = \left|\rho_{F,(h,v)}\right|^2 \left|\rho_{s,(h,v)}\right|^2$) [29]. The vegetation factor should also be taken into account, but the empirical models at millimeter wave frequencies are insufficient, thus making it very difficult to be able to reliably evaluate the vegetation effect. It can be seen in [26, p. 287] that at X-band a thin grass can reduce the reflection by 10 dB. Fig. 2.4 clearly shows how quickly the specular component is deteriorated as the normalized surface roughness (h_{rms}/λ) increases. However, at very long radar ranges ($\sim R > 100h_t$) when the grazing angle approaches zero, the specular component dominates even though the surface roughness increases. Surfaces can be treated as smooth if they satisfy the Rayleigh roughness criterion

$$2h_{rms} \sin\phi > \lambda/4, \tag{2.10}$$

such as a rough asphalt at microwave and millimeter wave frequencies having $h_{rms} = 0.9$ mm and a Gaussian distribution [30].

The geometry of multipath propagation is shown in Fig. 2.5. The geometry is for flat Earth, since the radar ranges are assumed to be short. The radar antenna and target elevations are h_r and h_t, and the target is located at range R. The radar signal will reach the target and reflect back to the receiving antenna via two paths, R_d and $R_r = R_{r1} + R_{r2}$, creating altogether four different signal paths. For radar applications, such as fire or missile control, the primary effect of multipath is to displace the targets from their correct elevation. In the elevation plane when the grazing angles are very shallow and a specular reflection occurs, the targets appear somewhere between the real target and the image, or even below the ground surface.

The sum of the direct and reflected signals at the location of the target is

$$E(R) = \frac{E_0 e^{-jkR_d}}{4\pi R_d}\left(1 + \frac{R_d}{R_r}\rho_F e^{j\Phi}\rho_s e^{-jk(R_r - R_d)}\right). \tag{2.11}$$

The constructive and destructive interference of the electromagnetic waves caused by multipath can be described with a propagation factor. In general, the propagation factor is a term used to characterize wave propagation when free space conditions are not met. In case of a nearly horizontally looking radar the multipath propagation effects dominate in the formation of the propagation factor. The one-way propagation factor, the so called path gain factor, for the multipath propagation conditions of Eq. 2.11 is

$$F = \left|\frac{E_d + E_r}{E_d}\right| = \left|1 + \rho_F e^{j\Phi}\rho_s e^{-jk(R_r - R_d)}\right|, \tag{2.12}$$

because $R_d/R_r \approx 1$. Using the geometry of Fig. 2.5 and truncated binomial series expansion (assuming $R \gg h_r, h_t$) the range difference can be written as [31, pp. 295-298]

$$\begin{aligned} R_r - R_d &= \sqrt{R^2 + (h_t + h_r)^2} - \sqrt{R^2 + (h_t - h_r)^2} \\ &\approx R + \frac{(h_t + h_r)^2}{2R} - \left(R + \frac{(h_t - h_r)^2}{2R}\right) \\ &\approx \frac{2h_r h_t}{R}. \end{aligned} \tag{2.13}$$

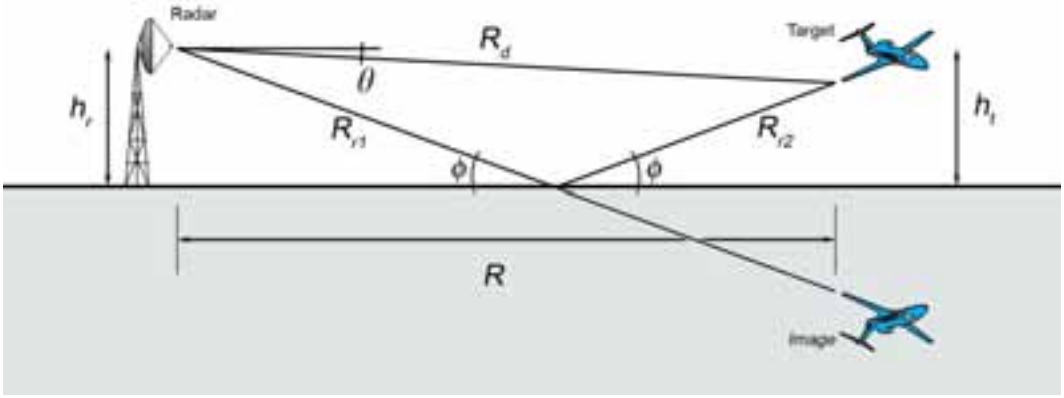

Figure 2.5: *The geometry of multipath propagation, a flat Earth approximation.*

Furthermore, for a smooth surface the product of Fresnel- and specular reflection coefficients at very small grazing angles ($\phi \leq 2°$) of the multipath signal from the surface is -1. Substituting this coefficient and the result of Eq. 2.13 into Eq. 2.12 yields

$$F = \left|1 - e^{-j\left(\frac{4\pi h_r h_t}{\lambda R}\right)}\right| = 2\left|\sin\frac{2\pi h_r h_t}{\lambda R}\right|. \tag{2.14}$$

Using reciprocity of the multipath propagation geometry, the power at the radar can be calculated by multiplying the radar equation (Eq. 2.4) with the factor F^4. Since the sine function (Eq. 2.14) varies between 0 and 1 depending on the phase difference between the direct and reflected signal paths, the signal power arriving to the radar will vary between 0 and 16. Taking into account the fourth power relationship between the target range and the echo signal power, the radar range varies between 0 and 2 times the range of the same radar in free space due to multipath propagation factor. Thus, the presence of a conducting flat ground plane causes the radar elevation beam to break up into a lobed structure. If a target is in the lobe, it will ideally be detected at twice the range than in free space, whereas precisely in between the lobes it theoretically will not be detected at all. When the distance between a target, having a constant altitude, and a radar changes, the target passes through a number of lobes. The resulting power variation as a function of range is depicted in Fig. 2.6. When the range from the radar is increasing, the last maximum of the factor F^4 occurs at range $R_T = 4h_r h_t/\lambda$, which is called the transition range [32, pp. 40-41]. Beyond that range the received power is proportional to R^{-8}, and the basic form of radar equation (Eq. 2.4) can be approximated with

$$P_r = \frac{4\pi P_t G^2 \sigma}{\lambda^2 R^8}(h_r h_t)^4, \tag{2.15}$$

by using $\sin x \approx x$ for small x in Eq. 2.14. The transition range increases rapidly when the altitude of either the radar antenna or the target is elevated. In the example of Fig. 2.6 the altitudes of the target and the radar relative to each other are unfavorable, and therefore the transition range is only $R_T = 2100$ m. In practical situations the non-uniform vegetation and the curvature of the Earth that diverges the rays cause uncontrollable variations in the propagation factor, thereby making the maxima and minima less intense.

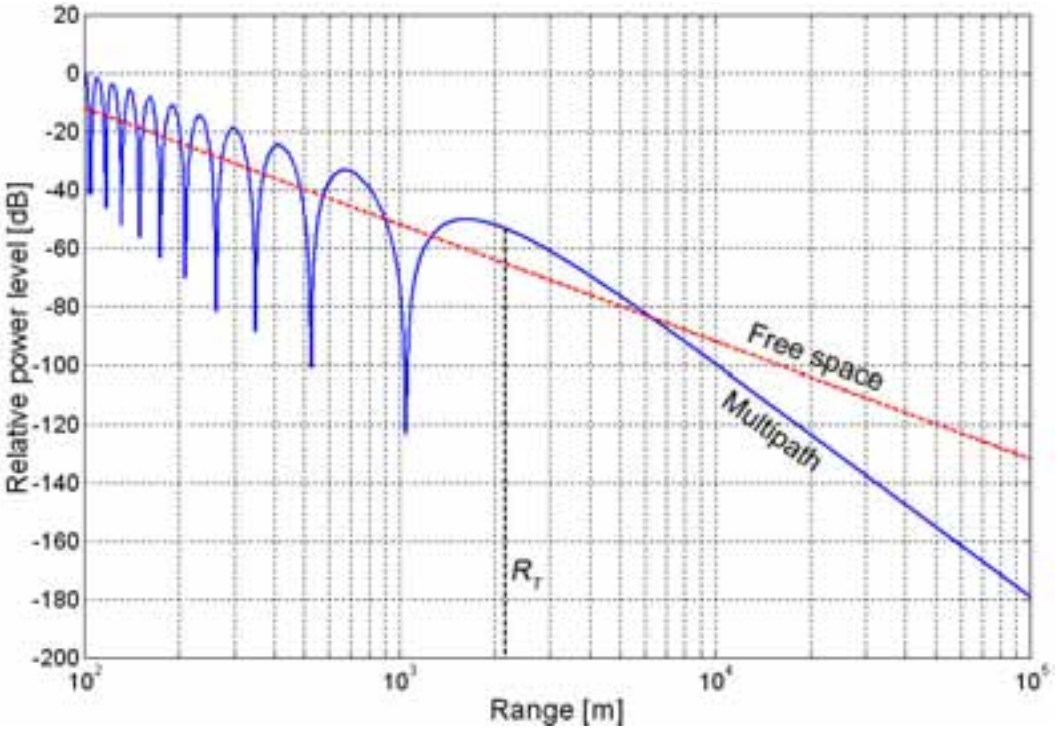

Figure 2.6: *The received power variation of a constant altitude target as a function of range compared to free space propagation. In this 35 GHz radar example $h_r = 3$ m, half of the total target height $h_t = 1.5$ m and the power level is normalized so that the values are relative to the power level at $R = 100$ m. After the transition range the power level is proportional to R^{-8}.*

2.1.3 Discussion of radar cross section and far-field criterion

Radar targets are described with a term radar cross section (RCS), which in monostatic radar operation relates the amount of power that hits the target to the amount of power that is reflected back into the radar receiver. RCS can be generalized also for bistatic operation (see paragraph 2.2.3). The RCS is a range independent characteristic feature of a target only when the target is in the far field of the radar antenna, which can be seen from the theoretical definition of RCS:

$$\sigma = \lim_{R \to \infty} 4\pi R^2 \left(\frac{P_r}{P_i} \right), \tag{2.16}$$

where P_r and P_i are the backscattered power at the radar receiver and the incident power at the target, respectively. By definition, the far-field condition for RCS is dictated by the precision with which the field incident on the target is required to approximate a plane wave in phase behaviour. The transverse phase deviation of the incident field must be within a specified tolerance, which traditionally has been set to be equal or less than 22.5° across the illuminated area. Based on this value the far-field condition is fulfilled when $R \geq 2D^2/\lambda$. In practice it is common to have a situation where the antenna is much smaller than the target, at which time it is possible to define the far-field condition based on the maximum dimension of the target rather than the antenna. At millimeter wave

frequencies the far-fields of many targets, such as ground vehicles and aircrafts, may be in the order of tens of kilometers. The impact of the huge target far-field criterion on the RCS measurement accuracy is demonstrated in the following discussion. If we consider a target to be a cylinder with length L viewed from broadside, the reduction in observed RCS due to a phase taper across the target compared to the real (far-field) RCS is [33]

$$\frac{\sigma_{meas}}{\sigma_{far}} = \frac{\lambda R}{L^2}\left|\int_0^{L/\sqrt{\lambda R}} e^{-j(\pi/2)t^2}dt\right|^2 = \frac{\lambda R}{L^2}\left[C^2\left(\frac{L}{\sqrt{\lambda R}}\right) + S^2\left(\frac{L}{\sqrt{\lambda R}}\right)\right], \tag{2.17}$$

where $C(x)$ and $S(x)$ are the Fresnel cosine and sine integrals. The result of this equation is shown in Fig. 2.7 for a case of $L/\lambda = 500$. The graph illustrates, that for a specular type scatterer with its largest dimension exceeding that of the radar antenna the phase tapering across the target results in a several decibels deviation of the measured RCS from the far-field RCS unless the far-field condition is determined based on the target's "aperture".

Most of the real targets at millimeter wave frequencies have their dimensions much larger than the wavelength ($L > 500\lambda$) and they can be thought of as consisting of a great number of individual scatterers. Therefore the RCS of a target is highly dependent on the aspect angle, and it is typical for the RCS measurement data to have irregular maxima and minima with narrow lobewidths. One goal of RCS measurements of a specific target is to obtain some key figures that characterize the visibility of a target at a certain wavelength. One of these figures is the average RCS of the target. Because of averaging, there is no need to preserve the precise phase coherence between the individual scatterers. Therefore the most important factor that determines the average RCS measurement accuracy is the amplitude tapering across the target. It was found in [34], that when a large target is illuminated with a narrow radar beam, the resulting amplitude tapering across the target caused larger error than too small range ($R < 2L^2/\lambda$). It was shown in [33], that for a thin and long target with its main axis perpendicular to the normal of the antenna beam, and the density of the individual point scatterers obeying a uniform distribution on the target length, the ratio of the observed average RCS to the true average RCS of a target is

$$\frac{\sigma_{meas}}{\sigma_{far}} = \sqrt{\frac{\pi}{2\ln 2}}\frac{R\theta_{3dB}}{L}\ \mathrm{erf}\left(2\sqrt{\ln 2}\frac{L}{R\theta_{3dB}}\right), \tag{2.18}$$

where the error function is given by

$$\mathrm{erf}(t) = \frac{1}{\sqrt{2\pi}}\int_0^t e^{-\frac{x^2}{2}}dx. \tag{2.19}$$

The term θ_{3dB} is the 3 dB beamwidth of a Gaussian shaped antenna main beam. The Eq. 2.18 is plotted in Fig. 2.8 for different $R\theta_{3dB}/L$ -ratios. The minimum acceptable measurement range for a particular target can be determined with Eq. 2.18, when the target length and the radar beamwidth are known.

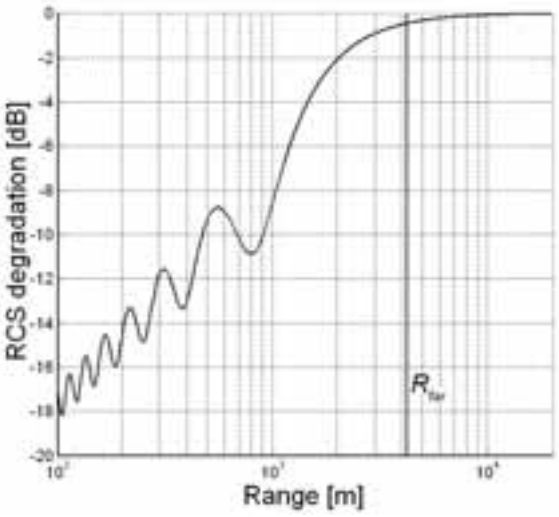

Figure 2.7: *The reduction in measured RCS due to a phase taper across the target compared to the real (far-field) RCS for a cylinder with $L/\lambda = 500$ [33]. The far-field range is marked with R_{far}.*

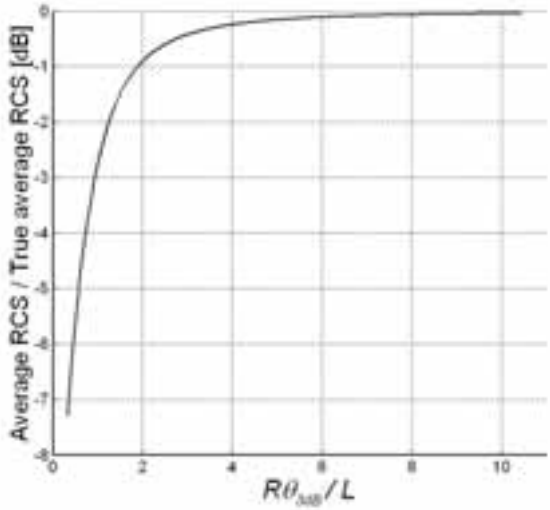

Figure 2.8: *The ratio of the measured average RCS to the true average RCS of a thin and long target with main axis perpendicular to the radar [33].*

2.2 Types of radars

Radar systems are often sorted into different categories according to their specific function and installation platform. These include for instance surveillance, navigation, fire-control and imaging radars, which can be ground based, naval, airborne or even spaceborne applications. Because radars observe the environment within the constraints of frequency, polarization and illumination geometry of the emitted electromagnetic waves, they can also be further classified by their characteristic features into i.e. short-range, polarimetric or phased array radar classes. Nevertheless, it is customary to divide the different radar systems into two major categories based on the waveform they use, regardless of the specific function of the radar. The two categories are continuous-wave (CW) and pulsed radar. The illumination arrangement and geometry in use further yields to monostatic, bistatic or even multistatic system.

2.2.1 CW radars

A basic CW radar (Fig. 2.9) employs a continuous transmission that results in a continuous echo signal from the objects within the illuminated volume. The long available integration time of the CW waveform radars allows to use low power transmitters, since the peak power is almost equal to the average power. Therefore CW radars possess low probability of intercept (LPI) features, since they are difficult to detect by intercepting devices. Because of the simultaneous transmitting and receiving operation of a CW radar, the separation of the weak echo signal from the strong transmitted signal must be based upon the Doppler frequency shift produced by moving targets. The detection of stationary

targets is almost impossible because of clutter echoes and leakage from the transmitter into the receiver. To avoid the CW receiver from being saturated by it's own transmit signal, a reflected power canceller (RPC) is used to suppress the zero Doppler signal in the receiver path [35]. However, due to FM noise sidebands of the transmitted signal, targets with a low radial velocity (<0.5 m/s) are lost as well. Excellent isolation properties of an RPC have been demonstrated up to X-band, but it is difficult to implement an RPC at millimeter wave frequencies due to the complex nature of the design and the need for high precision vector modulator [36]. Without additional filtering, the achievable isolation between transmitter and receiver is only 20-30 dB for CW radars with a single antenna using a ferrite circulator as a duplexer. In short-range, low-power solutions the 20-30 dB dynamic range in the power budget may be enough, but in order to improve the sensitivity of the radar system separate transmission and receive antennas must be used. This may prevent the use of CW radar on small-scale moving platforms due to the increased size and weight associated with having two antennas.

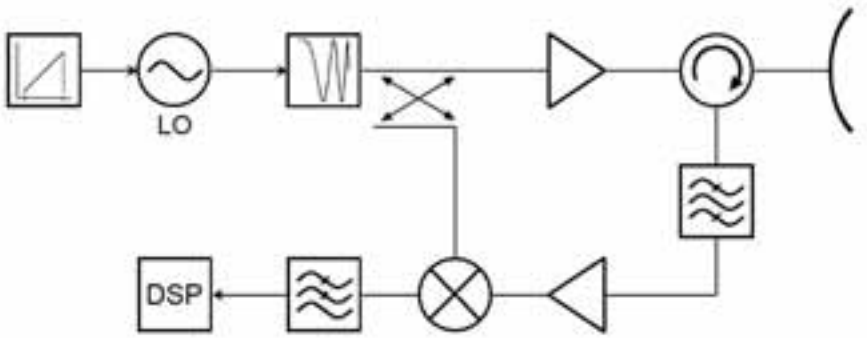

Figure 2.9: *A block diagram of a simple homodyne frequency-modulated CW radar using a single antenna for transmitting and receiving. A sample of the LO signal in this diagram is fed to the receiver with a directional coupler, but in many practical applications where the RPC-technique has not been implemented, the LO signal is directly fed to the receiver through the circulator. These systems are referred to as autodyne [37, p. 16].*

Besides low power transmitters, the primary advantage of CW radar is the ability to perform unambiguous Doppler measurement. On the other hand the target range measurements are entirely ambiguous since the continuous nature of the radar waveform does not permit accurate estimation of unique range information. This limitation can be overcome by adding timing marks into the transmission, which is usually realized by changing the frequency of the transmitted signal in a predetermined way. Such a radar is called frequency modulated CW (FMCW) radar. The modulating frequency is usually swept in a linear fashion, following a periodic triangular or saw-tooth waveform [38], but other modulation schemes, such as sinusoidal frequency sweep or frequency shift keying (FSK), have also been used. The frequency deviation and modulation period have a direct effect on the range and doppler resolution as well as on the bandwidth requirements of the hardware. When decreasing the deviation of the modulating signal the requirement of hardware bandwidth is also decreased and thus sources with lower phase noise are available. On the other hand in this trade-off the range resolution gets worse as well [39]. In

future vehicular radar applications, such as collision avoidance and autonomous driving systems, the simultaneous target range and velocity measurement with high resolution and accuracy is required also in situations when multiple targets are present. To meet these requirements with traditional FMCW waveforms would lead to unacceptably long measurement times. Therefore, more sophisticated waveforms have been proposed [40], which supports the dominating position of FMCW radar as a technological solution for vehicular radar also in the future.

2.2.2 Pulse radars

A majority of all surveillance, navigation and weather radars are pulse radars that use a waveform consisting of repetitive short-duration pulses (Fig. 2.10). Due to the short duration of the transmitted RF energy the peak power of the transmitter must be kept high. The typical duty cycle of pulse radars (<1%) results in smaller average transmitted power than in CW radars.

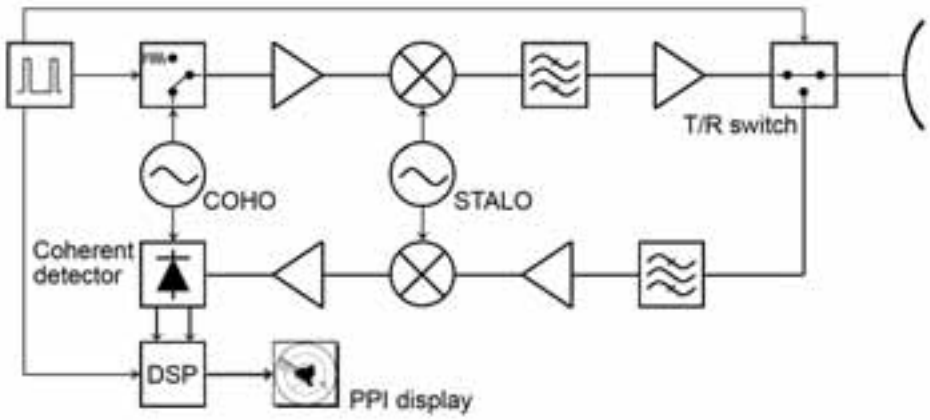

Figure 2.10: *A simplified block diagram of a pulse radar.*

The pulse repetition frequency (PRF) is the rate, in pulses per second, with which the RF pulses are sent. To avoid range ambiguity, the PRF must be such that the echoes from the expected maximum distance are allowed to return to the receiver before the next pulse is transmitted. If the PRF is set to correspond the desired radar coverage, the range determination is performed by measuring the time delay of the echo with respect to the transmitted pulse. In coherent radar systems the PRF represents also the rate at which the radar takes samples of the phase of the echo pulses, changes arising from the relative motion of the radar and the target [41]. To keep the velocity measurement unambiguous, the maximum allowable phase shift between successive pulses is $\pm\pi$ rad, which corresponds to a Doppler frequency of

$$f_D = \pm PRF/2 \tag{2.20}$$

and radial velocity of

$$v_D = \pm PRF \cdot \lambda/4. \tag{2.21}$$

Therefore the Doppler shifts generated by most airborne targets are folded down into the insufficient Doppler frequency band of typical long-range surveillance radars, and the

true radial velocity information is lost. The selection of suitable PRF is not only a choice between unambiguos range and velocity, but it depends also on the desired velocity resolution and scanning method of the radar. Since the detection propability of a single pulse is rather low, integration of successive target echoes is performed in all practical radar applications. Ideal coherent integration of n pulses increases the signal-to-noise ratio by the factor of n [42]. Because the number of pulses available for integration is a function of PRF and target illumination time, the selection process of radar antenna scanning speed and PRF is a compromise between several requirements. The dilemma is illustrated in Fig. 3 of [P6]. A common practice to unfold the aliased Doppler frequencies or to cope with multiple-time-around echoes is to use PRF staggering [43]. The changing of the pulse repetition interval on a pulse-to-pulse basis (or in larger groups) in a regular pattern provides means to solve the unambiguities in range or velocity measurement [44, 45]. In radars using the moving target indication (MTI) -filtering technique the PRF staggering pushes the first null of the MTI-canceler further in the velocity response curve thus improving the detection probability [46].

The detection capability of a pulse radar depends on the energy transmitted in the radar pulses. Transmitting longer pulses increases the average transmitted power, but at the same time degrades the range resolution of the radar. The increasing of the average transmitted power can be accomplished without compromising the range resolution by modulating the radar pulses. Since the range resolution depends on the bandwidth of the pulse, a technique called pulse compression is widely used in pulse radars to increase the bandwidth of transmitted pulses [47, p. 530]. A great number of pulse compression techniques has been developed, of which linear frequency modulation and binary phase coding are most widely used [48, 49]. In the radar receiver the echo pulses are compressed in the time domain by correlating the received signal with a replica of the transmitted pulse, resulting in a finer range resolution than would be achieved with an unmodulated pulse. The main drawback in the use of pulse compression is the appearance of range sidelobes around the main signal peak, which cause overspilling of target echo power into adjacent range gates [50]. In addition to the amplitude masking caused by the range sibelobes, they also contaminate the phase information of the signal in the range gates they fall in.

2.2.3 Monostatic, bistatic and multistatic configurations

In previous sections describing the CW and pulse radar it was assumed that the transmitter and receiver share a common antenna, forming a monostatic radar system. A bistatic radar consists of separately located transmitting and receiving sites, and a multistatic system may have several transmitters and receivers located at considerable distances from each other (Fig. 2.11). Most of the measurements presented in this thesis are made with a monostatic radar.

Bistatic radar systems have been studied and built since the earliest days of radar, and in fact the very first radars were based on bistatic configuration, because devices such as ferrite circulator or T/R switches were not available yet. However, when more sophisticated means of achieving signal isolation between the transmitter and receiver emerged, the research and development of bistatic radar has reduced, and the main focus has been

Figure 2.11: *Radar illumination geometries: monostatic (left), bistatic (center) and multistatic (right) configuration.*

on monostatic radars. Nonetheless, the geometry of bistatic radar generates a number of advantages that a monostatic radar is unable to provide [51].

The operation of a bistatic radar is defined by a coordinate system on a plane containing the transmitter Tx, receiver Rx and the target [52] (Fig. 2.12). The concentric ellipses with foci at receiver and transmitter locations represent the isorange contours and the hyperbolas the constant time-difference of arrival (TDOA) contours of a bistatic radar system (Fig. 2.13). In a multistatic network the azimuth angle of a target (θ_R) as seen from a receiving site is provided by the directive receiver antenna. The target-to-receiver range is more complicated issue that has to be solved from the bistatic triangle. To accomplish this the baseline length (L) and the range sum ($R_t + R_r$) have to be known. The solution of the target-to-receiver range is of the form [P8]

$$R_r = \frac{(R_t + R_r)^2 - L^2}{2(R_t + R_r + L\sin\theta_R)}. \tag{2.22}$$

In order to be able to calculate the range R_r it is necessary to provide some form of synchronization between the transmitter and receiver [53]. Several synchronization techniques are available, of which a cable or fiber link is the most accurate alternative. A cable connection, however, is not suitable for mobile bi- or multistatic radar networks, and they must instead establish the timing reference through direct radio, optical connections or via satellite link [54]. A radio connection is the most feasible solution for mobile multistatic radar systems, because the use of a satellite link makes the radar dependent on an external system and the use of optical synchronization requires uninterrupted line-of-sight between transmitter and receiver.

Despite of the challenge in the technological solution of proper synchronization method, the transmitting and receiving systems of bistatic radars are potentially simple and cheap. Moreover, the receiving sites in a multistatic network are passive and hence undetectable by means of electronic support measures (ESM). Bistatic configuration may also possess a counterstealth capability, since target shaping specifically designed to reduce the monostatic RCS will not in general reduce the bistatic RCS. The bistatic radar equation is

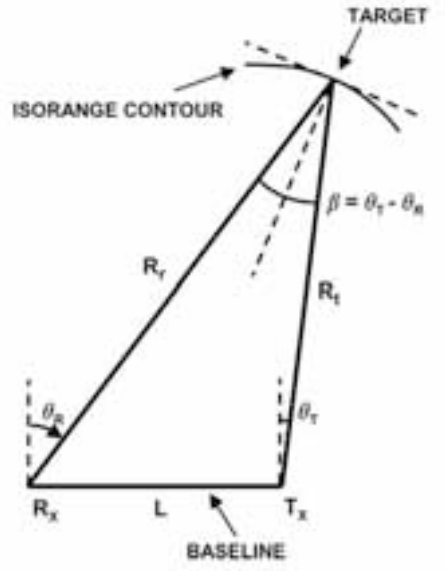

Figure 2.12: *The bistatic coordinate system. The bistatic triangle in this figure is shown in a north-referenced coordinate system.*

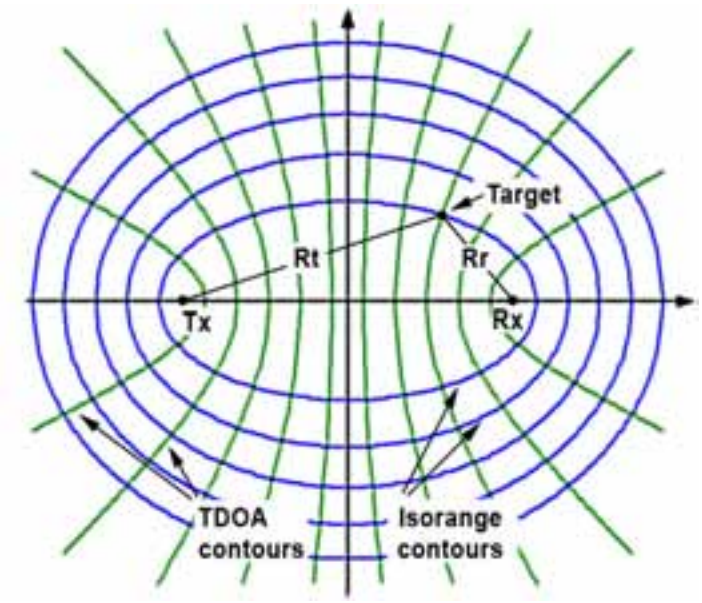

Figure 2.13: *The isorange contours (concentric ellipses) and time-difference-of-arrival (TDOA) contours (concentric hyperbolas) on the bistatic plane.*

derived in the same manner as the monostatic radar equation (2.15), yielding:

$$P_r = \frac{P_t G_t G_r \lambda^2 \sigma_{bi}}{(4\pi)^3 R_t^2 R_r^2} F_t^2 F_r^2. \tag{2.23}$$

The bistatic radar equation shows, that the bistatic RCS has the same effect on the received power level than the backscattered RCS in monostatic configuration. Thefore it is beneficial for multistatic radar networks, that the bistatic scattering coefficient of land clutter at moderate bistatic angles ($20° < \beta < 120°$) is generally reduced from the value of backscattering direction. Although low grazing angle measurements of clutter bistatic scattering coefficients have not been extensively reported in literature, the few measurement campaigns described in [55] show a maximum decrease in the order of 10 dB in land clutter relative to the monostatic value. In addition to that, the illuminated clutter cell area at small grazing angles ($\phi \leq 2°$) in bistatic geometry is smaller than in monostatic case approximately by a factor of $\sim \cos^2(\beta/2)$. This combined with the small ground scattering coefficients reduces the received ground clutter power levels 5-15 dB thereby making the signal-to-land clutter ratio of bistatic radar system equal or better than in monostatic radar system.

2.3 Basic signal processing issues

Radar signal processing is a field that covers numerous tasks ranging from tracking algorithms to antenna sidelobe cancelling. One of the main purposes of a radar signal processing unit is to extract the desired targets from raw radar echo signals. These radar

targets must be detected against the noise and clutter background, which will vary with range, antenna bearing angle and time. The detection algorithms are based on the amplitude and phase information of the received signal, and depending on radar hardware also polarimetric properties can be utilized. The detection process consists of two main tasks: a filtering stage where noise and clutter interference is suppressed, and a detection stage where the decision concerning the presence of a target is made. Although this thesis does not specifically deal with radar signal processing, in the following some elementary issues concerning radar detection will be briefly discussed.

For a moving ground-based or airborne radar the changes in clutter reflectivity and statistical behaviour are continuous and rather unpredictable, whereas for fixed radars the knowledge of the surrounding clutter environment can be used as a subsdiary tool for target detection, as for example in a form of a frequently updated spatial clutter map [56]. When considering the detection performance of a radar, the amplitude of backscattered clutter echo can not be given a unique value, as it depends on the specific RCS and phase associated with individual scatterers within the illuminated area or volume. Therefore the amplitude behaviour must be described statistically.

Commercially available modern coherent radars employ quadrature detection to create their baseband signals. After quadrature detection, the signal consists of bipolar in-phase and quadrature-phase signals, the so called I- and Q-channels. The probability density function (pdf) of radar signal amplitude is composed from unipolar envelope signal [57], which corresponds to the magnitude of the phasor vector whose components the two quadrature channels are. The radar signal vector in I/Q-plane is a vector sum of all backscattered signals from a given resolution cell plus thermal noise. Therefore, depending on the relative amplitudes and phases of the signals, the desired target signal may occur anywhere in the I/Q-plane within the constraints of the dynamic range of radar video voltage. The detection threshold should be set to provide an acceptable level of false alarms and maximize the probability of detection [58]. The relationship between probability of false alarm (P_{fa}) and probability of detection (P_d) and their dependence on the probability density functions of target echoes and noise is illustrated in Fig. 2.14.

A false alarm occurs when signal voltage (u) exceeds the threshold voltage (U_T) when noise alone is present in the receiver. The receiver noise is assumed to be Gaussian due to its thermal nature. When it is passed through a narrowband filter, the pdf of the envelope of the noise voltage output can be shown to follow a Rayleigh probability density function. Therefore the probability of false alarm can be determined by integrating the pdf:

$$P_{fa} = \int_{U_T}^{\infty} \frac{u}{\Psi^2} \exp\left(-\frac{u^2}{2\Psi^2}\right) du = \exp\left(-\frac{U_T^2}{2\Psi^2}\right), \tag{2.24}$$

where Ψ^2 is the variance of noise voltage [59]. The probability of detection is defined in an analogous manner, being the probability of a signal exceeding the threshold voltage in a case a target is present at the resolution cell. Assuming a non-fluctuating target with an amplitude of a_t, the probability of detection can be found by integrating the Ricean

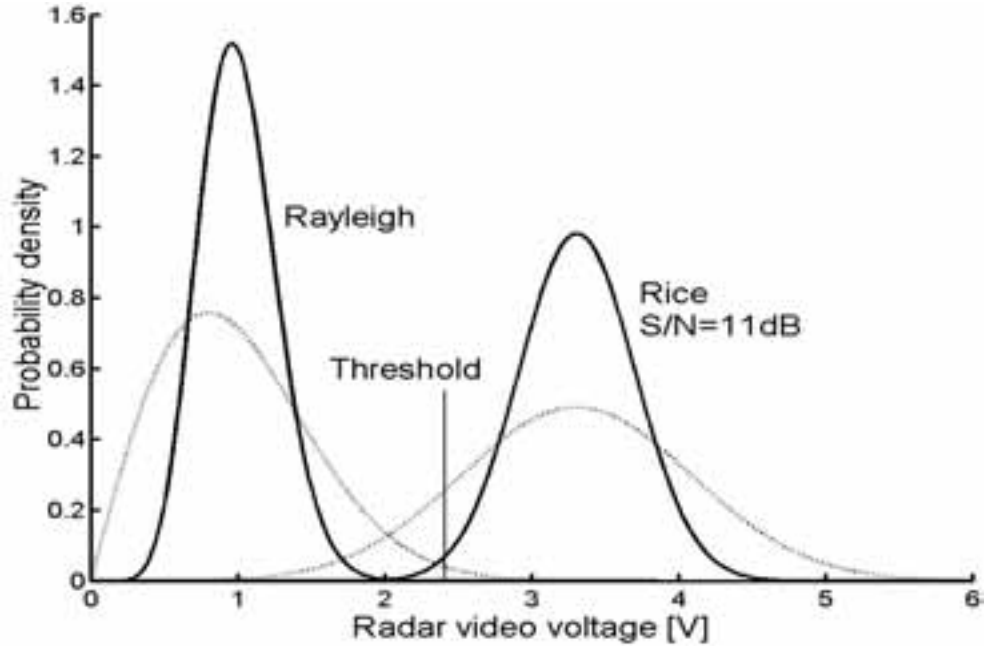

Figure 2.14: *A graphical example of the relationship between probability of false alarm and probability of detection. Probability density functions for one pulse are shown with dotted line and for five integrated pulses with solid line. The noise alone follows Rayleigh distribution whereas a non-fading target echo, whose average signal-to-noise ratio is 11 dB, and Rayleigh distributed noise together are characterized with a Ricean pdf. The voltage threshold was initially set for one pulse to provide* $P_{fa} = 10^{-2}$ *and* $P_d = 0.90$. *After integration the detection performance was increased to* $P_{fa} = 2 \cdot 10^{-6}$ *and* $P_d = 0.98$.

distribution function

$$P_d = \int_{U_T}^{\infty} \frac{u}{\Psi^2} \exp\left(-\frac{u^2 + a_t^2}{2\Psi^2}\right) I_0\left(\frac{u a_t}{\Psi^2}\right) du, \tag{2.25}$$

where $I_0(x)$ is the modified Bessel function of the zero order and the threshold voltage is $U_T = \sqrt{2\Psi^2 \ln(1/P_{fa})}$ [60]. The equation of P_d can not be be evaluated in a closed form, and therefore numerical techniques or a series approximation must be used. The equation (2.25) can be described with a Marcum Q-function:

$$P_d = Q\left(\sqrt{\frac{a_t^2}{\Psi^2}}, \sqrt{2 \ln\left(\frac{1}{P_{fa}}\right)}\right). \tag{2.26}$$

The generalized Marcum Q-function of order 1 is defined by the integral [61]

$$Q(\alpha, \beta) = \int_{\beta}^{\infty} \zeta I_0(\alpha\zeta) e^{-(\zeta^2+\alpha^2)/2} d\zeta. \tag{2.27}$$

In Fig. 2.15 the detection probability is plotted as a function of single pulse signal-to-noise ratio for several false alarm probabilities. The graph was created by using an algorithm

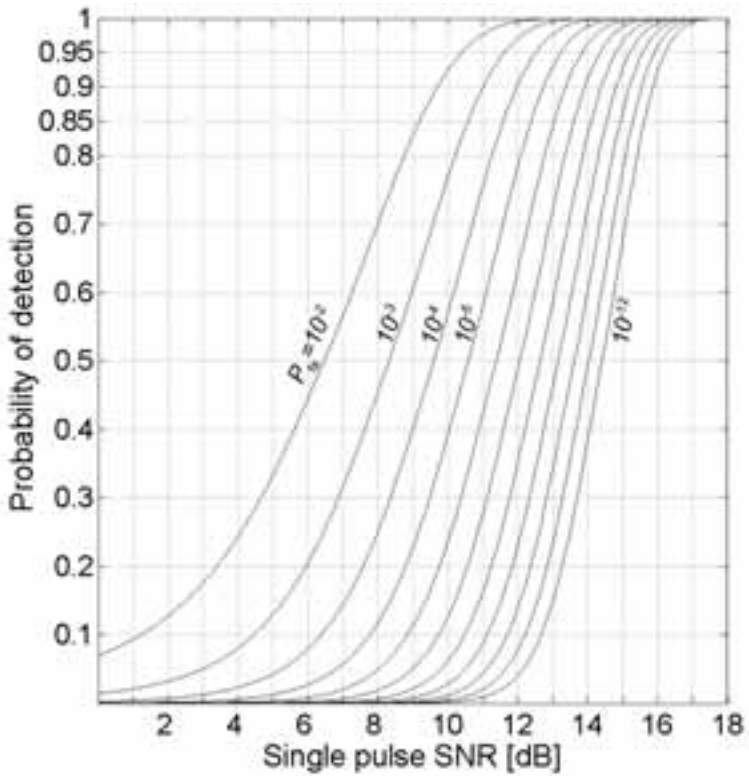

Figure 2.15: *The probability of detection as a function of single pulse signal-to-noise ratio with probability of false alarm as a parameter. Practical radars require a performance of at least* $P_{fa} > 10^{-6}$ *and* $P_d > 0.95$*, which corresponds to a minimum single pulse* $(S/N) > 13.65$ *dB. It is not possible to achieve the required* (S/N) *in all situations, and therefore integration of pulses is carried out in all pulsed radar systems. The graph was computed by using a numerical algorithm [61] for Equation (2.26).*

for numerical computation of Eq. (2.26) presented in [62]. Figure 2.15 illustrates the need for pulse integration in order to achieve the desired levels of P_{fa} and P_d, which for most of the practical radar applications can not be achieved just by detecting a single pulse. The pdf of echo signals will be modified by the integration process (see Fig. 2.14). For n independent identically distributed variates the pdf of their sum after non-coherent integration is an n-fold convolution of the single pulse pdfs [63]. For thermal noise the samples from pulse to pulse are assumed independent, but in case of clutter the successive pulses are often correlated [64]. Therefore, in order to obtain independent samples from clutter echoes, the decorrelation times of specific clutter types should be known to adjust the integration time accordingly [65]. Furthermore, the equation (2.25) above assumes a non-fluctuating target echo during the integration period. However, it is obvious that the RCS of any moving target will have temporal fluctuations as the target's yaw angle as seen by the radar changes.

To properly account for target and clutter fluctuations, both the probability density functions and the correlation properties with time must be known for a particular target and clutter type. Ideally, these characteristics should be measured for different targets and target trajectories, but such measurement campaigns are not easily realizable. A more practical approach has been to formulate a reasonable model for target fluctuations and to analyse the effects mathematically. The radar community has widely accepted the four fluctuation models proposed by Swerling [66] already in 1960 to describe the RCS behaviour of man made targets. For clutter backscattering, on the other hand, there are no models that are widely applicable for different situations, despite of the numerous measurement campaigns described in the literature [67, 68, 69]. The empirical models based on actual measurement data have not provided reliable description of low grazing angle

clutter above X-band. Furthermore, the semi-empirical models based on measurement data collected at one place fail to describe the clutter behaviour in another geographical location. Therefore clutter backscattering measurements have to be conducted separately for different radar types and clutter environments. Still, the empirical models are based on average conditions and are developed to enable average radar performance estimations and comparisons between different signal processing methods. On a given day of radar operation the conditions can vary significantly from the average predictions. Moreover, when trying to derive an exact relationship between false alarms and detection probability one needs to bear in mind that the disturbing effect caused by false alarms depends on the radar application. In systems, where the radar data is rapidly updated (the scanning rate and/or the scanning geometry is such that the target area is illuminated tens or even hundreds of times every minute) the false alarms can be eliminated by simply correlating the data from successive scans thereby making the single scan false alarm probability requirements less severe. Also depending on the level of automation the needs concerning false alarm rate may be very different from radar to radar. Human observer is much more tolerant against false alarms than an automatic algorithm [70].

As can be found from Fig. 2.15, the probability of false alarm is very sensitive to the setting of the detection threshold voltage. In practical situations the nonstationary clutter background means that a fixed detection threshold is not useful and therefore adaptive techniques are required to maintain a constant false alarm rate (CFAR) in all circumstances [71]. There are several different implementations of constant false alarm rate

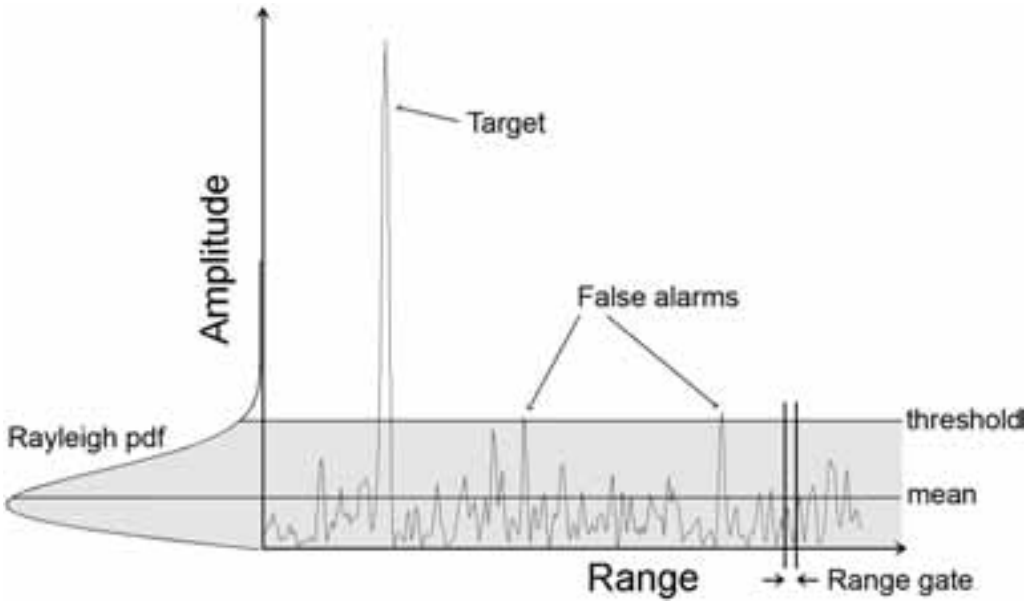

Figure 2.16: *An illustration of the constant false alarm principle depicted in an A-type radar display. In this case only Gaussian noise and one target are present, and a threshold of desired probability of false alarm is set according to Rayleigh pdf. In case the signal level would rise, a new threshold would be estimated locally for each range gate. In this case the selected value of* P_{fa} *is too low, allowing for two false alarms to occur.*

processors [72], which all establish a detection threshold by estimating the characteristic features of reference cells surrounding the actual cell under test, see Fig. 2.16. A CFAR processor operates by examining a window of range- or cross-range cells or an area around the test cell. Usually CFAR processing is applied for signal amplitude, but similar methods can also be employed in connection with Doppler frequency or even polarization fingerprints [73, 74].

A cell averaging CFAR is an adaptive procedure that estimates the clutter mean level around the test cell. It assumes that the clutter is uniformly distributed and that the reference cells are good representatives of the local clutter level. For air surveillance radars these assumptions are not a problem as the area around an aircraft is generally empty, and good background statistics can be obtained [75, pp. 494-497]. However, for ground targets a uniform clutter situation within the reference window is hardly ever maintained due to sudden changes in clutter characteristics. This is made worse by the fact that ground vehicles often hide at the edges of clutter boundaries to reduce the probability of detection. In order to reduce the strong and non-uniform clutter while maintaining a constant false alarm rate, several CFAR processors have been developed in which the clutter statistics are modeled as Pearson [76], Weibull [77], log-normal [78] and K-distributions [79]. These detection schemes are suitable for traditional microwave radars up to X-band, but for millimeter wave radar there are no reports of effective CFAR solutions. When the wavelength of the radar signal approaches the dimensions of the subscatterers, the clutter echoes become more spiky and the spatial intensity variations between resolution cells can be as high as 20-30 dB. This kind of clutter behaviour at millimeter wave frequencies makes the use of CFAR-type of algorithms more challenging than at lower frequencies.

In addition to the amplitude information of a radar signal, a coherent radar can also utilize the phase information. The signal processing methods that use the phase information can operate parallel to the amplitude-based techniques, and the outputs of the two processing paths can be correlated to give the final detection decision. If such parallel processing has not been implemented into a radar system, the phase information is usually treated first.

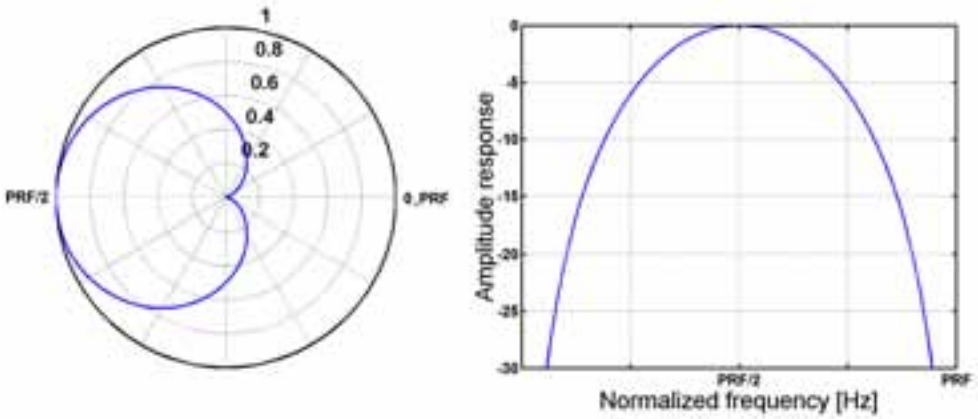

Figure 2.17: *Normalized frequency response of a three pulse MTI-canceller (delay line coefficients [1 -2 1], see Eq. (2.28)) on an I-Q -plane (left) and frequency-plane (right).*

The two methods that are able to discriminate moving targets from stationary objects are moving target indication (MTI) and Fast Fourier Transform (FFT)-based Doppler filter bank [80]. MTI is based on the fact that the clutter spectrum is typically concentrated around DC and multiple integers of the radar PRF. Therefore the stopband of an MTI-filter should be selected so that the clutter power from stationary echoes is attenuated to desired level and on the other hand so that the elimination of slow velocity targets is minimized. A basic three pulse canceler impulse response is given by

$$h(t) = \delta(t) - 2\delta(t - 1/PRF) + \delta(t - 2/PRF), \tag{2.28}$$

where $\delta(t)$ is the delta function. The respective frequency response is shown in Fig. 2.17. In the FFT-based Doppler processing method a spectral analysis of the return echoes is performed for each range cell. The radar signal is analyzed by applying the fast Fourier transform, which performs a sophisticated coherent integration of successive echoes. Contrary to MTI-processing, in Doppler processing the entire frequency information is preserved, which allows target detection also in circumstances where the radar resolution cell is occupied by both the target and volume clutter having a non-zero radial velocity. The difference in output information of MTI and Doppler processor is illustrated in figure 2.18. As this illustrative example shows, FFT-processing does not make "decisions" concerning detection, since it preserves all information, whereas MTI may accidentally cancel out slowly moving or velocity aliased targets that fall on the stopband.

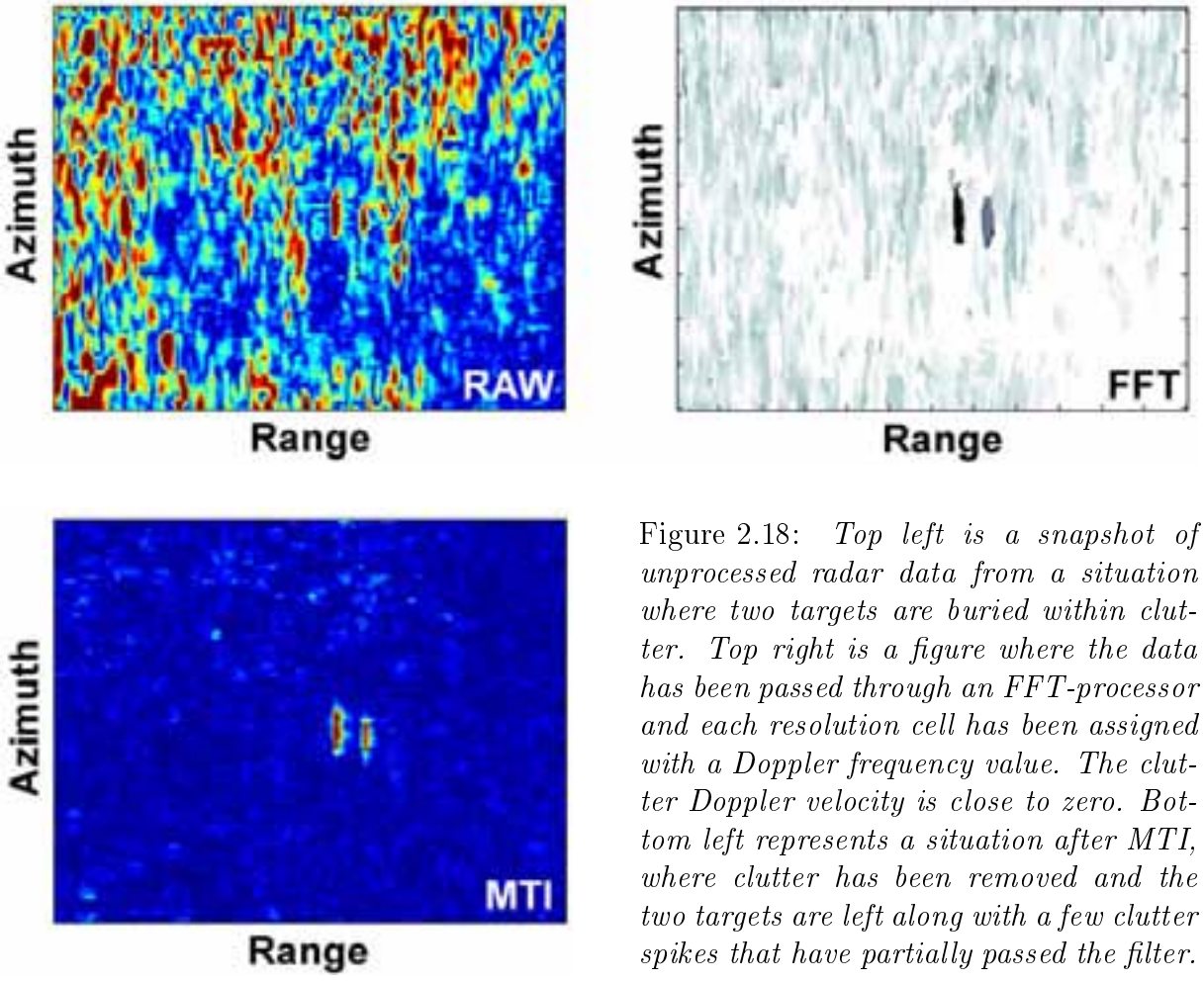

Figure 2.18: *Top left is a snapshot of unprocessed radar data from a situation where two targets are buried within clutter. Top right is a figure where the data has been passed through an FFT-processor and each resolution cell has been assigned with a Doppler frequency value. The clutter Doppler velocity is close to zero. Bottom left represents a situation after MTI, where clutter has been removed and the two targets are left along with a few clutter spikes that have partially passed the filter.*

3 Millimeter wave test instrumentation radar

In order to be able to evaluate millimeter wave radar operation in real environmental conditions and to empirically study the clutter background at millimeter wave frequencies, several different instrumentation radars were designed and constructed during the thesis work. In this chapter some design outlines and calibration issues are discussed and a V-band instrumentation radar is presented in more detail.

3.1 Design outlines due to field test requirements

For practical reasons, one of the main requirements for the design and construction of the instrumentation radar systems was resistance against severe weather conditions at the test sites. A fixed test station could not be considered due to the desire to be able to meet different kinds of environments (terrain profile, vegetation) as well as have an ability to make RCS-measurements in a flexible manner. Therefore, the radar hardware had to be designed to withstand all weather conditions without any shelters or additional heating. Furthermore, for some of the test systems a possibility for unattended operation and data recording over long time periods had to be taken into account. Meaningful recordings over long periods of time extended the reliability requirements to cover also the data logging system. Proper test sites for prolonged operations, in which unwanted human interference could be minimized, were not always equipped with reliable power sources, and the survivability of radar hardware and data logging system in case of temporary loss of primary power had to be ensured. Furthermore, due to lack of proper sheltering and guarding at the test sites, the possibility of equipment loss or damage could not be excluded and therefore expensive millimeter wave laboratory instruments were out of question.

Portability was another key factor in the design of the test instrumentation radars. Many millimeter wave instrumentation radars presented in literature seem to be rather large, and therefore only limited mobility between interesting locations is available with these systems [81, 82]. To ensure flexible mobility, the radar system as well as all necessary equipment was required to fit inside a regular station wagon car. Some of the remote test sites were not reachable by car, so in order to set up the equipment into a desired location the radar had to be carried by hand for the last tens or hundreds of meters. Therefore the size and weight of the hardware had strict requirements. Fortunately these requirements could be met, since recent advances in modern millimeter wave communication systems and the related development of cost-effective semiconductor devices enabled a rather compact design.

Keeping in mind the definite requirements related to portability and expected weather conditions as well as the estimated budget, the desired radar performance figures were

outlined. The intended use of the different test radar systems involved backscattering measurements of surface and volume clutter, research work concerning millimeter wave radar signal propagation and an ability to carry out RCS measurements. A suitable antenna for these tasks should have its beamwidth in the order of one degree, which would be in good agreement with a true operational radar. Due to the research nature of the radar system there was no need to implement any kind of scanning control or electrical steering function. The mechanical structure of the radar mounting pedestal was designed to be firm and stable to ensure consistent illumination of a selected area as well as to enable precise alignment of the antenna main beam even without servo control.

The pulse repetition frequency was designed to be adjustable from very low values up to 100 kHz. The wide PRF selection range would allow to use values corresponding to different kinds of operational modes of millimeter wave radars, ranging from very high update rate systems intended for nearby environment monitoring tasks to long range surveillance systems. The PRF selection also has an impact on the unambiguous Doppler range of the test instrumentation radar. The adjustment option made it possible to set the PRF according to the anticipated Doppler-frequencies during the specific testing period. The flexibility was further added by making the transmitted pulse width selectable within the IF bandwidth limits as well.

3.2 Optimization of beam shape and pulse width

By definition it is assumed that an object with a specific radar cross section is a point target from the viewpoint of the observing radar. Therefore it is not practical to use radar cross section when dealing with surface or volume clutter, because in most operational situations the radar instantaneously illuminates the vast clutter sources in such a way, that the radar range cell (volume) or the cross section of the antenna beam is completely filled with e.g. rain or land. Therefore the backscattered clutter power is dependent on the specific radar antenna beamwidth and pulse width. To overcome the system dependent definitions surface clutter is characterized by surface reflectivity per illuminated area, the scattering coefficient σ^0:

$$\sigma^0 = \sigma / A_c, \tag{3.1}$$

where the illuminated area A_c is a function of radar antenna beam shape, pulse width and grazing angle. In typical ground-based radar geometry the antenna beam footprint on the surface in range direction exceeds the projected range resolution (set by the pulse width) of the radar. This situation is defined to be a pulse-limited illumination geometry, and the received power for such a case is [83, pp. 752-753]:

$$P_r = \frac{P_t G_0^2 \lambda^2}{(4\pi)^3 L_{atm}} \int_{A_c} g(\theta) p\left(t - \frac{2R}{c}\right) \frac{\sigma^0 dA}{R^4}, \tag{3.2}$$

where $p(t)$ is a weighting function that accounts for pulse shape variations and $g(\theta)$ antenna beam shape variations. For beamwidths in the order of 1° and pulse widths less than a few hundred nanosecons the variations of σ^0 and R^4 can be assumed to be negligible across the illuminated area [84]. Furthermore, if a radar in use has its unmodulated pulse shape approximately rectangular (the rise- and fall-times of the pulse being short),

the pulse shape weighting function equals unity. Therefore the illumination integral is expressed solely by the gain variation in across-range direction. From the illumination geometry one can derive an approximation for the area of the instantaneously illuminated radar footprint at small grazing angles ($\phi < 10°$) to be [68, pp. 42-43]

$$A_c = \frac{1}{2} c\tau R\theta_{3dB,az} \sec\phi. \tag{3.3}$$

The notion of using 3 dB antenna beamwidth is a traditional way to describe radar illumination. This obviously results in 6 dB power level reduction at the edges of the radar footprint compared to beam maximum, and especially small targets situated at footprint edges are buried under the thermal noise floor. If we choose to define the illuminated area by using 1.5 dB antenna beamwidth points instead, the two-way power falloff from the edges of the footprint is reduced to 3 dB. The respective reduction in the illuminated area corresponds more properly to the actual effective beam area from which the majority of the backscattered power originates. The difference between using 1.5 dB beamwidth instead of traditional 3 dB points when measuring uniformly distributed clutter is well below 2 dB.

A parabolic antenna mainlobe pattern follows a $\cos^2$-function (Fig. 3.1). By solving the illumination integral, a beam shape correction factor $1/\alpha$ to account for nonuniform beamwidth illumination can be calculated. By choosing the correction factor to correspond with the 1.5 dB beamwidth, a relation between correction factor and illumination integral can be written as:

$$2 \int_0^{\frac{1}{2}\theta_{1.5dB}} \cos^2\left(\frac{\theta}{a}\right) d\theta = \frac{1}{\alpha}\theta_{1.5dB}, \tag{3.4}$$

where the scaling coefficient $a = 2\theta_{3dB}/\pi$ is expressed in terms of the 3 dB beamwidth. As a result the beam shape correction factor becomes

$$\frac{1}{\alpha} = \frac{1}{2} + \mathrm{sinc}(\pi - 2) \approx \frac{1}{1.11}. \tag{3.5}$$

With these definitions the scattering coefficient in pulse-limited geometry at small grazing angles ($\phi < 10°$) is

$$\sigma^0 = \frac{(4\pi)^3 R^3 L_{atm} 2\alpha}{G^2\lambda^2 c\tau\theta_{1.5dB}\sec\phi}\left(\frac{P_r}{P_t}\right). \tag{3.6}$$

In case of perfectly perpendicular incidence the effective illuminated area simply becomes

$$A_c = \frac{\pi R^2}{4\alpha^2}\theta_{1.5dB}^2, \tag{3.7}$$

where a parabolic antenna with equal azimuth and elevation beam patterns is assumed. From this the expression for the scattering coefficient in perfectly perpendicular illumination geometry is

$$\sigma^0 = \frac{256\pi^2 R^2 L_{atm}\alpha^2}{G^2\lambda^2\theta_{1.5dB}^2}\left(\frac{P_r}{P_t}\right). \tag{3.8}$$

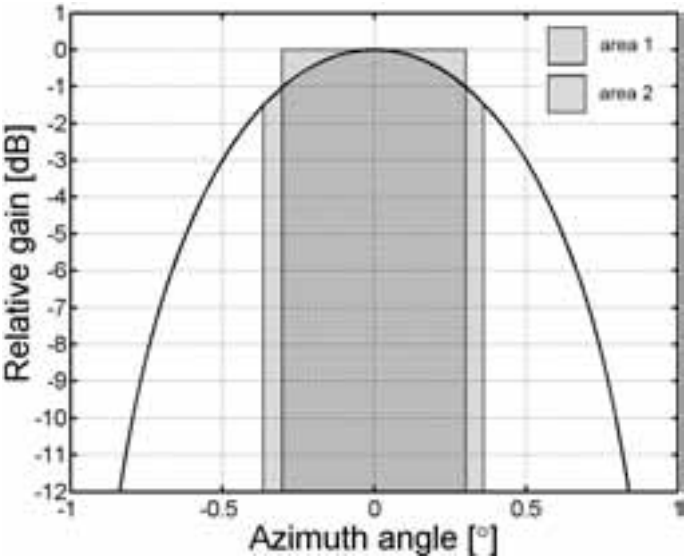

Figure 3.1: *The width of the radar footprint at across-range dimension is defined by the 1.5 dB points of the mainbeam. A correction factor is calculated with the illumination integral to account for the nonuniform illumination. The shaded areas 1 and 2 are equal. As a result of the correction factor the effective footprint area for beamshapes following cos^2-function can be calculated using the 1 dB points.*

A volumetric resolution cell for a parabolic antenna with equal azimuth and elevation beam patterns is obtained by multiplying Eq. (3.7) with $c\tau/2$ [67], resulting in volumetric scattering coefficient equation:

$$\eta = \frac{512\pi^2 R^2 L_{atm} \alpha^2}{G^2 \lambda^2 \theta^2_{1.5dB} c\tau} \left(\frac{P_r}{P_t}\right). \tag{3.9}$$

A radar system should be designed to give a reasonable combination of thermal noise performance, clutter reduction, spatial resolution and tolerance against jamming. These topics are coupled through the processing bandwidth of a pulse radar. Very narrow bandwidths will generally give low noise levels, whereas the observed clutter amplitude increases if we employ longer pulses. The radar pulse width selection has typically been closely connected to the maximum target dimension due to the general assumption that the target-to-clutter ratio is maximized when mathcing the pulse width to the largest target dimension. The desired range resolution in most cases will also be achieved when this traditional pulse width selection process is followed.

Modern DSP-technology enables real-time implementation of complex signal processing algorithms, which may even allow target detection in situations where the signal-to-noise ratio is less than one. The backscattered clutter power effectively increases the noise floor in the radar receiver thereby degrading the minimum detectable RCS. The amount of received clutter power is, among other parameters, a function of pulse width. The limits that clutter returns and thermal noise alone set on the maximum range of detection for a specific target RCS can be calculated for different radar pulse widths. These maximum range curves converge to produce a solution for the optimal pulse width for a radar configuration in given clutter conditions. This kind of method does not respond to requirements related to range resolution or survivability under electronic interference, but provides an effective way to manage the complicated relation between noise performance and clutter backscattering. The use of such pulse width selection tool gives the radar engineer an insight into radar performance in certain operational environment.

The thermal noise-limited maximum range of a radar as a function of pulse width can be calculated using Eq. (2.6) for specific target RCS. In the equation the time-bandwidth product ($B_n\tau$) is chosen to correspond with the IF lowpass filter shape and transmitted pulse shape, and the lowest allowable signal-to-noise ratio is selected according to the signal processing performance. The clutter-limited maximum range can be similarly estimated by setting:

$$\sigma = \sigma^0 \frac{1}{2\alpha} c\tau R\theta_{1.5dB} \sec\phi \quad \text{surface clutter} \tag{3.10}$$

$$\sigma = \eta \frac{\pi R^2}{4\alpha^2} \theta^2_{1.5dB} \frac{c\tau}{2} \quad \text{volume clutter} \tag{3.11}$$

and solving each case for R. The behaviour of thermal noise-limited and volume clutter-limited maximum ranges as a function of pulse width and target RCS is illustrated in Fig. 3.2 for arbitrary radar characteristics. The two cases each define a surface on which the maximum radar range lies. The intersection of the two surfaces defines a curve which represents the optimal solution for the radar pulse width for different target RCS values.

To determine the optimal pulse width for our instrumentation radars, we estimated a generic set of radar and clutter parameters. Cost-effective hardware components, that would satisfy the initial test radar performance requirements, indicated transmitted power at the output stage in the order of +23 dBm and +10 dBm and system noise temperature of 350 K and 850 K for K_a- and V-band, respectively. The antenna gain used for both frequency bands was 40 dBi. Furthermore, the lowest allowable signal-to-noise ratio was set to 0 dB and a matched filter receiver was assumed ($B_n\tau = 1$). With these definitions the thermal noise-limited radar range could be calculated for selected RCS-values. In the design stage of the test radars there was no self-acquired clutter data available for the desired frequencies, so the surface and volume scattering coefficient values were looked up from open literature. Since the literature is almost completely lacking low grazing angle ground clutter data at millimeter wave frequencies, very generic values were used. The figure 3.39 in [67] suggests approximately $\sigma^0 = -20$ dB(m^2/m^2) at K_a-band and $\sigma^0 = -17$ dB(m^2/m^2) at V-band, which were selected to represent typical ground clutter

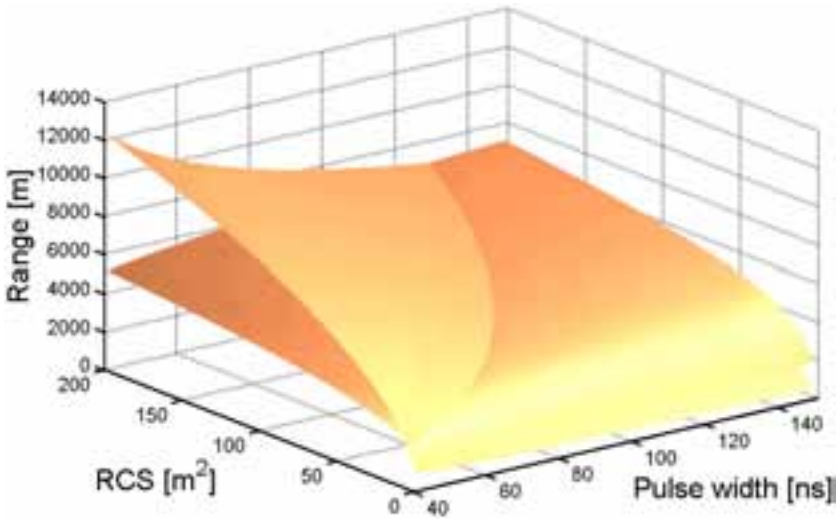

Figure 3.2: *Thermal noise and volume clutter-limited maximum ranges define surfaces whose intersection curve marks the optimal radar pulse width for different target RCS values. This figure illustrates the pulse width optimization method, and therefore the specific parameters used to create the graph are not of interest here.*

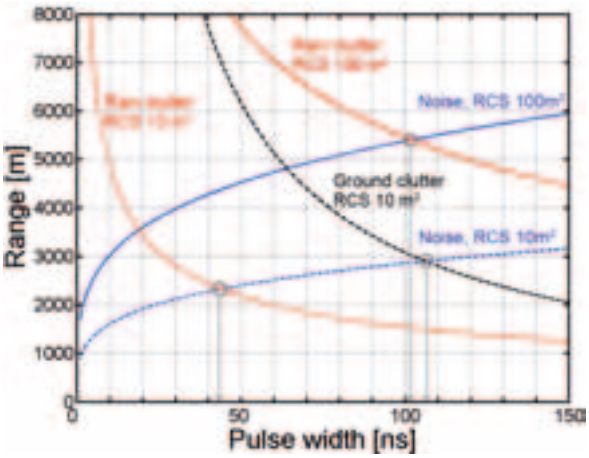

Figure 3.3: *Obtainable radar range for various pulse widths at K_a-band. Solid lines describe a case for target RCS of 100 m^2 and dashed lines for 10 m^2. Blue curves represent the noise-limited, red curves the rain clutter-limited and black curve ground clutter limited case. The ground clutter limited case for target RCS of 100 m^2 is outside of the graph area.*

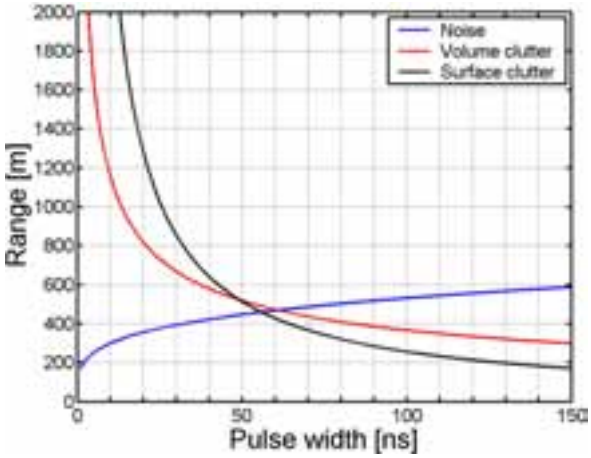

Figure 3.4: *Obtainable radar range for various pulse widths at V-band. The target RCS is 1 m^2. Blue curve represents the noise-limited, red curve the rain clutter-limited and black curve ground clutter limited case. Atmospheric attenuation has not been taken into account in this graph. If desired, it can be included as a scaling factor for the range axis.*

values. Rain backscatter data at millimeter wave frequencies is more readily available. The volume scattering coefficient was calculated using least square fit equation based on Ballistic Research Laboratory (USA) measurements [85] to give $\eta = -30.2$ dB(m^2/m^3) at K_a-band and $\eta = -26.8$ dB(m^2/m^3) at V-band for rain intensity of 10 mm/h.

Once the parameters were defined, graphs for pulse width optimization could be calculated. Figures 3.3 and 3.4 show obtainable radar ranges for different pulse widths for K_a- and V-bands. As indicated in Fig. 3.3, ground clutter does not limit the maximum radar range for targets having RCS = 100 m^2 when using pulse widths below 150 ns, whereas for target RCS of 10 m^2 the optimal pulse width in ground clutter conditions is 107 ns at K_a-band. Rain backscattering (with rain intensity of 10 mm/h) starts to limit the maximum range when pulse widths are above 102 ns and 43 ns for target RCS of 100 m^2 and 10 m^2, respectively. At V-band the situation with the selected parameters seems to be more straightforward. Against a one square meter target the ground- and rain clutter curves indicate optimal pulse width values 56 ns and 61 ns, and for a 100 m^2 target (not plotted in Fig. 3.4) the maximum radar range is not affected at all by clutter returns when using pulse widths shorter than 150 ns. Real targets at V-band have RCS far beyond 1 m^2, so the pulse width selection at this frequency band is not based on the optimization against clutter returns, since the thermal noise floor and atmospheric attenuation are the critical limiting factors of the radar range.

Due to the absence of exact knowledge of volume- and surface clutter backscattering coefficients, the pulse width optimization process can be further elaborated by sweeping

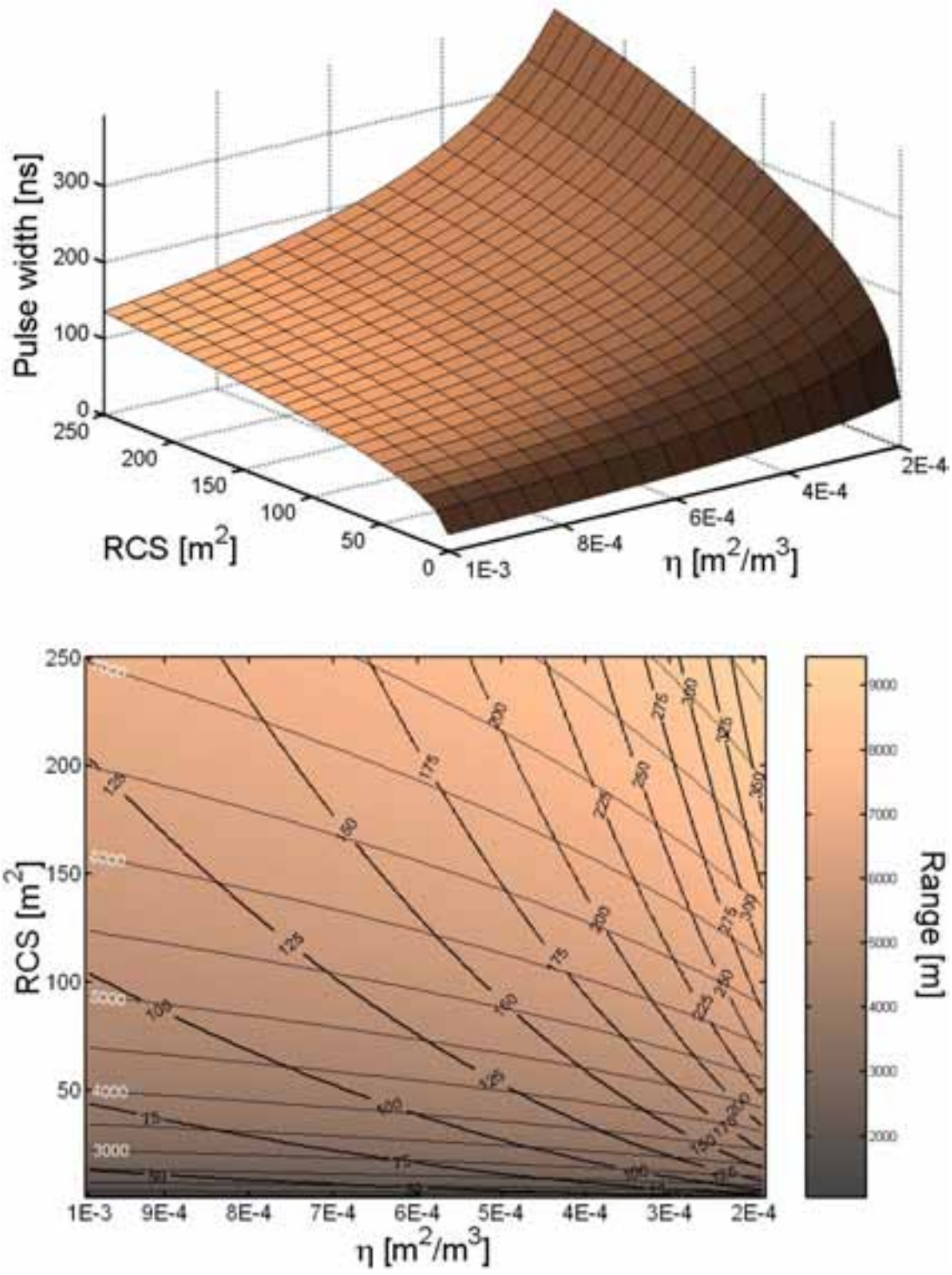

Figure 3.5: *A solution for the optimal pulse width as a function of target RCS and volumetric backscattering coefficient for K_a-band. On the lower graph the optimal pulse width-surface is represented with a set of labeled isocurves. The corresponding radar range is presented with colours at the background. The isocurves for range are presented with narrow contour lines, and the labels are with white font.*

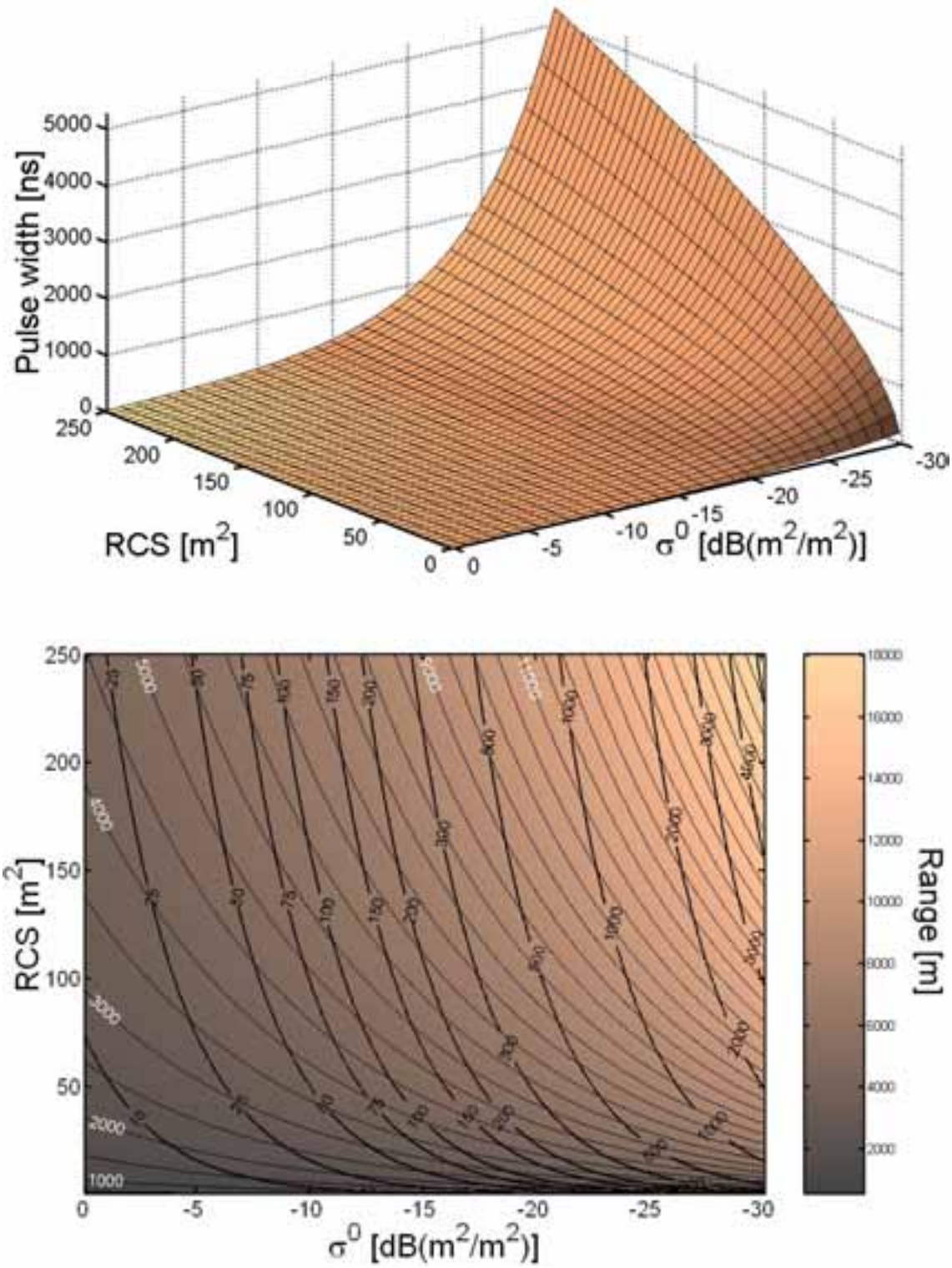

Figure 3.6: *A solution for the optimal pulse width as a function of target RCS and surface backscattering coefficient for K_a-band. On the lower graph the optimal pulse width-surface is represented with a set of labeled isocurves. The corresponding radar range is presented with colours at the background. The isocurves for range are presented with narrow contour lines, and the labels are with white font.*

η and σ^0 over a range of values. If the target RCS is also allowed to vary, the solution for the optimal pulse width as a function of the two variables (η and σ for volume clutter case and σ^0 and σ for surface clutter case) defines a surface (see topmost plot of Figures 3.5 and 3.6). An apparent drawback of the method is the complicated interpretation of the results, since the radar range information is missing from the surface plot. The pulse width optimization process for a given set of radar parameters involves a simultaneous management of four interrelated factors, namely the backscattering coefficient, radar range, target RCS and pulse width. Therefore a graphical representation of the optimal pulse width as a function of the remaining three factors is problematic, since the solution would be a four-dimensional surface. An attempt towards a more appropriate visualization of our results is shown in the lowermost images of Figures 3.5 and 3.6. The optimal pulse width-surface (as a function of target RCS and backscattering coefficient) is represented with a set of labeled black isocurves for K_a-band. In the background of the image the corresponding radar range is presented as a coloured plane. The colourbar on the right relates the different shades of colour to the range values. To enhance the readability of the range values additional thin contour lines have been added and marked with white labels.

The essential information to aid pulse width selection process is contained in Figures 3.5 and 3.6. The optimal pulse width for a specific clutter situation can be read from the graphs for a selected target RCS value. Additionally, the obtainable radar range is readily available for the selected parameter combination. It should be noted, however, that even though an optimal pulse width can be found for all cases, it is not always a resonable value from the viewpoint of other constraints, such as hardware realization or range resolution requirements. Furthermore, for pulse widths above several hundred nanoseconds the variation of range within the radar footprint on the ground has to be taken into account in the calculation of the illumination integral in Eq. (3.2). The optimal pulse width point marks the radar range at which the minimum detectable RCS equals the RCS produced by the clutter echoes. At ranges beyond that point the clutter echoes do not degrade the radar sensitivity whereas at shorter ranges the clutter starts to dominate increasing the minimum detectable target echo level. When the range corresponding to the optimal pulse width for a given scattering coefficient and target RCS has been determined, the signal-to-clutter ratio for that RCS as well as the clutter-to-noise ratio for other ranges using that pulse width can be calculated from:

$$\frac{S}{C} = \frac{C}{N} = 10 \log \left(\frac{R_{opt}}{R} \right)^3 \quad \text{[dB], surface clutter} \tag{3.12}$$

$$\frac{S}{C} = \frac{C}{N} = 10 \log \left(\frac{R_{opt}}{R} \right)^2 \quad \text{[dB], volume clutter} \tag{3.13}$$

By examining Fig. 3.5 one can see, that for example with $\eta = 6 \cdot 10^{-4}$ m^2/m^3 and $\sigma = 150$ m^2 the optimal pulse width is 159 ns and the obtainable range with these parameters is 6350 m. Furthermore, using Eq. (3.13) one can calculate the signal-to-clutter ratio for a target having RCS of 150 m^2 at desired range or for instance the range at which the clutter power saturates the receiver.

Due to the nature of Figs. 3.5 and 3.6, the range information in the backgound represents the thermal noise-limited radar range. This provides an additional feature of the graph for a radar engineer. By ignoring the scattering coefficient values on the x-axis one can estimate the obtainable radar range in clutter-free situation. The minimum detectable target RCS is marked by the intersection points of range and pulse width contours, providing for instance a possibility to fix two of the three values to obtain the third one.

Since one the main functions of the test instrumentation radars was to collect backscattering data, the pulse widths for the K_a- and V-band systems in fact should not be exactly optimized from the viewpoint of target detection. Instead, the pulse width selection process indicated a use of slightly suboptimal pulse widths in order to produce clutter levels from reasonable distances that would be conveniently within the dynamic range of the receiver.

3.3 Practical test system for V-band

A V-band instrumentation radar was designed and constructed within our research group using partly commercial and partly home-made components. The main elements of the radar are the transmitter, receiver and the IF-part, which each have been assembled as separate physical units. The whole system is enclosed within an aluminium frame to protect the hardware against dust and rain and to provide a sufficient level of electromagnetic shielding. A simplified block diagram for enhanced clarity of the V-band test system is shown in Fig. 3.7.

The millimeter wave signal is produced in the transmitter-unit by multiplying the 7.256

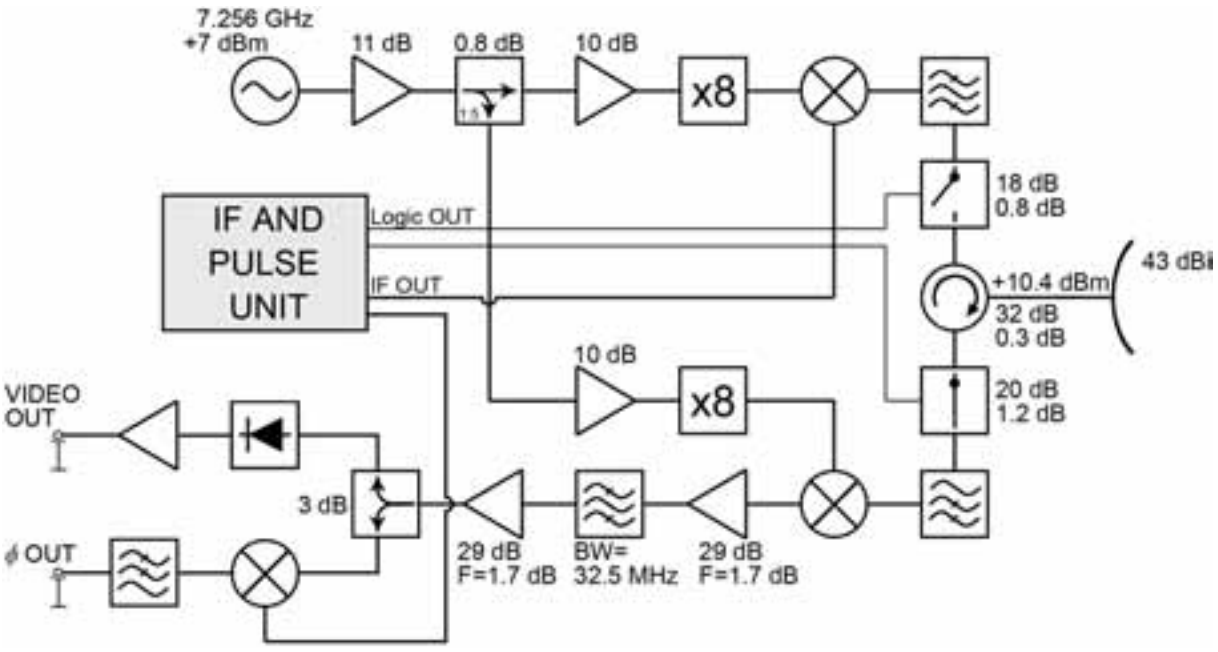

Figure 3.7: *A simplified block diagram of the V-band instrumentation radar.*

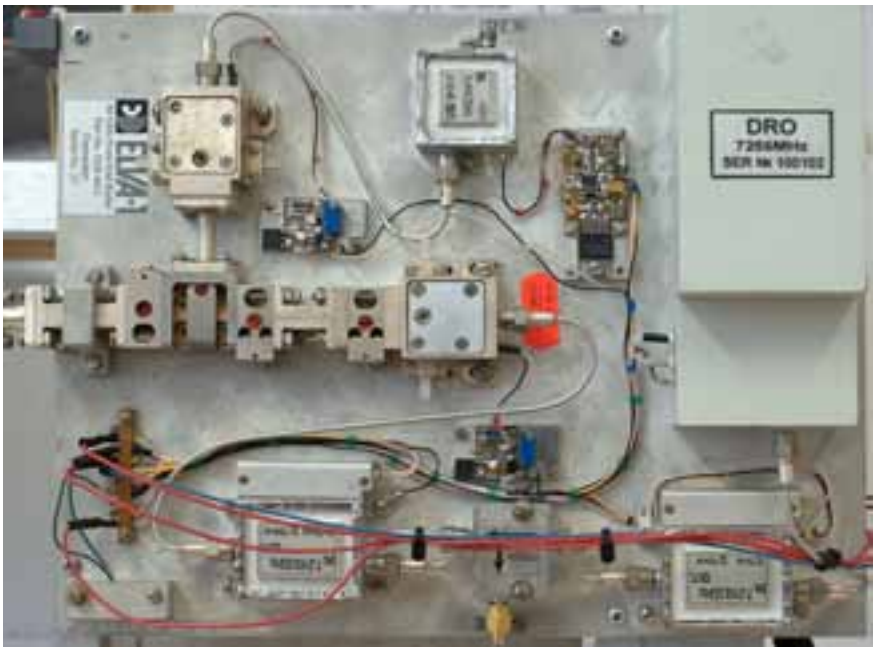

Figure 3.8: *The transmitter unit of the V-band instrumentation radar. Most of the hardware blocks are from ELVA-1 company.*

GHz DRO output with a factor of eight. Before multiplication, a sample of the original DRO-signal is fed to the receiver-unit through a 1:5 power divider. After the frequency multiplier the 58.048 GHz signal is mixed with a modulated IF to produce the actual waveform. The lower sideband of the upconverted spectrum is suppressed by a waveguide-type bandpass filter. The transmitted frequency can be selected within the passband of the filter by tuning the IF frequency. However, the IF frequency is selected to be in the high end of the tuning range to ensure sufficient attenuation of the lower sideband. A photograph of the transmitter unit is shown in Fig. 3.8.

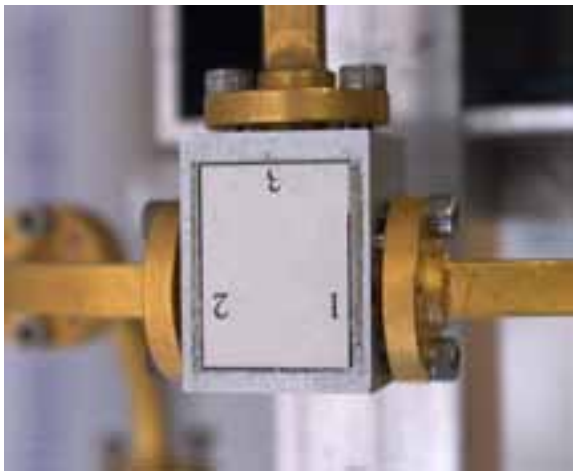

Figure 3.9: *The V-band ferrite circulator.*

The T/R-duplexer consists of three parts. The transmitter and receiver are connected to the duplexer with PIN-diode switches. These are further connected to a ferrite circulator, whose third port is the antenna-waveguide interface. The measured isolations of the switches are 18 dB (Tx) and 20 dB (Rx), and insertion lossess 0.8 dB and 1.2 dB, respectively. The circulator provides 32 dB isolation between transmitter and receiver (ports 1 and 2), and causes 0.3 dB attenuation to pass direction in both branches. A photograph of the ferrite circulator is shown in Fig. 3.9. The transmitted signal power at the antenna waveguide port is +10.4 dBm, and the transmitted

pulseform, measured with a diode detector, is shown in Fig. 3.10. The signal level could be increased by adding a power amplifier between radar front-end and the antenna, but this was not done because the desired radar range for clutter measurements could be achieved with current setup, and furthermore the benefit gained from the increased power level would not have been in line with the increase of cost. The antenna of the instrumentation radar is a parabolic reflector with a Cassegrain-type feed, see Fig. 3.11. The feed arrangement includes also the transition from WR-15 waveguide to a circular horn. In order to suppress the sidelobes, the antenna is equipped with a cylindrical collar.

In the receiver-unit the received radar signal is downconverted to the intermediate frequency using the eight times multiplied 7.256 GHz DRO output as a local. The signal is filtered using an interdigital stripline bandpass filter. As a result the instantaneous IF bandwidth is 32.5 MHz. At the end of the receiver chain the signal is divided into amplitude and phase channels using a Wilkinson 3 dB power splitter. In the amplitude channel a diode detector and a video amplifier are used to produce a unipolar video voltage from the envelope of the radar signal. The noise floor of the V-band instrumentation radar is at -94 dBm and the dynamic range of the receiver is 30 dB. A voltage proportional to the phase difference between the radar signal and the coherent local from the IF and pulse-unit is obtained from the IF port of a double balanced mixer. After lowpass filtering the bipolar video represents the phase of the radar signal. The decision of using amplitude and phase channels instead of quadrature detection is mainly based on minimization of IF hardware. Also the fact, that the instrumentation radar is intended for research work concerning clutter amplitude (scattering coefficient) behaviour, motivates the use of separate amplitude and phase channels. This arrangement enables the use of higher sampling rate in radar signal aquisition system compared to situation where two channels (I and Q) would be sampled simultaneously. Still, the phase information is available if needed.

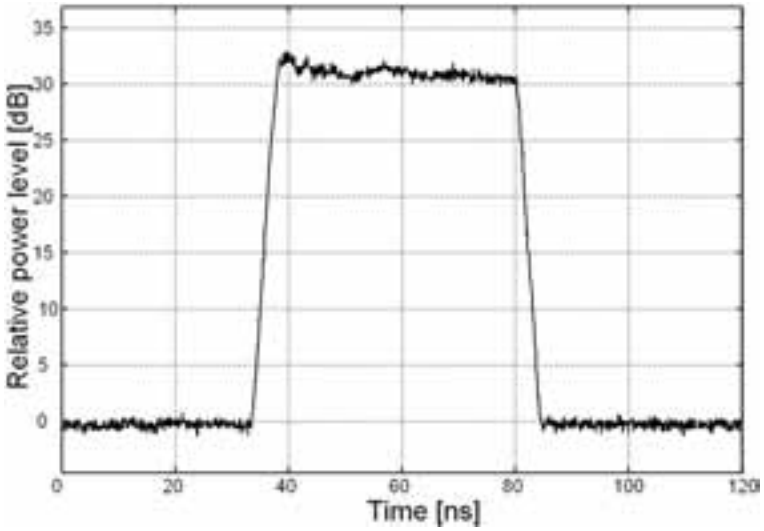

Figure 3.10: *The transmitted pulse of the V-band instrumentation radar. Dynamics is limited by the detector of the measuring device, and does not represent the true dynamics of the transmitted pulse.*

Figure 3.11: *The antenna of the instrumentation radar is shown left. It is a parabolic reflector with a cylindrical collar to suppress the side- and backlobe level. The photograph on the right shows the Cassegrain-type feed. The feed arrangement includes also the transition from WR-15 waveguide to a circular horn.*

The IF frequency and pulse modulation are generated in the IF and pulse-unit, and the IF frequency as well as the pulse repetition frequency are tunable. Because of the desire to record all radar returns down to zero Doppler frequency, special attention has to be paid to the pulse modulator characteristics. Particularly, any leakage of signal might be harmful for the receiver processing functions. The achieved ON/OFF ratio of the modulator is better than 110 dB (Fig. 3 of [P2]), which can not be seen in Fig. 3.10 due to the limited dynamics of the measurement device. As mentioned earlier, the unmodulated IF frequency is also used to coherently downconvert the radar signal to baseband at the phase video channel. Also the duplexer switches are controlled by TTL pulses originated in the logic circuit of the IF and pulse unit. They are realized with an Schottky-type circuit to ensure the fast rise- and fall times of the transmitted pulse.

3.4 Calibration

Despite quite accurate equipment and procedures are available for the measurement of radar transmitter power, receiver sensitivity and response and even antenna gain, true calibration target tests are the only reliable means of achieving absolute calibration of practical radar systems in the field [86]. These tests call for special calibration targets that have been used since the early days of radar and that consist of spheres covered by metal foil [87], corner reflectors of various sizes [88] and even active repeaters [89].

The internal calibration of our test radars involved laboratory measurements of transmitter power, frequency, pulse shape, detection curve and frequency response of the receiver. The transmitter power was measured from the antenna port using a power meter. The

average power measured by the power meter was related to peak power by measuring the exact pulse shape and pulse repetition frequency as well. Besides these, a wide band diode receiver was used for comparisons. The detection curve of the receiver chain was measured using a signal generator, from which a pulse modulated waveform at the exact PRF of the radar was fed into the antenna port (with the antenna removed), and an oscilloscope to record the detected voltage. A ratio method, which enables periodic calibration at the field [90, 91], was not implemented into any of the constructed test radars to avoid the extra attenuation introduced by the directional coupler. Moreover, the installation of such built-in calibration feature was not absolutely required, since the radar transmitting power variations and frequency drift over a time period of several hours was monitored regularly in laboratory, and the measurement data showed very stable and repeatable operation each time with relative power or sensitivity changes below 0.5 dB and frequency offsets less than 1 MHz. Furthermore, an indirect method to monitor the system stability in the field existed already, since due to the limited isolation of the duplexer a sample of the transmitted pulse was present at the receiver video channel thus providing means to observe the possible variations in the detected pulse amplitude. The laboratory tests provided precise knowledge of the radar parameters, but an absolute calibration called for measurements with targets of known radar cross section. In order to be able to relate received power with a true RCS, the antenna gain pattern as well as unidealities introduced by antenna port matching had to be included in the calibration scheme.

3.4.1 Calibration targets

A perfectly conducting sphere is very attractive as a calibration target because its RCS is constant regardless of attitude as seen form the direction of illumination and does not even change as a function of wavelength as long as the ratio of the circumference of the sphere to the wavelength in use is >10 (above the Mie-region) [92, Ch. 4] - a requirement not too difficult to meet at millimeter wave frequencies. However, the actual RCS value of a sphere is small and normally does not allow accurate level calibrations in an outdoor field environment where severe clutter is met. When using passive calibration targets the backscattered electric field is a combination of the calibration target echo and the fields backscattered from the background. Since the phase difference between the two electric fields can obtain any value between 0 and π, the corresponding calibration error falls between the maximum limits given by

$$\frac{\sigma_m - \sigma_c}{\sigma_c} = \frac{\sigma_b}{\sigma_c} \pm 2\sqrt{\frac{\sigma_b}{\sigma_c}}, \tag{3.14}$$

where σ_m is the measured RCS, σ_c the true RCS of the calibration target and σ_b the RCS of the background echo. From Eq. (3.14) we can see, that if the maximum uncertainty allowed for the calibration is ± 1 dB, the effective background RCS has to be less than 0.01 times the calibration target RCS. Since the RCS of a sphere at optical region is simply πr^2, the huge radius needed to produce the required RCS practically rules out the use of a sphere as a calibration target in situations where the illumination geometry causes the radar beam to be completely or even partially filled with clutter. However, if a sphere can be positioned high above the ground using a low-reflectivity structure, the backscattering from the ground, as well as multipath effects, can be avoided.

Four different calibration spheres, with RCS of -15 dBm^2, -17.5 dBm^2, -21 dBm^2 and -23.5 dBm^2, were used in our experiments. A sphere was mounted between two poles using nylon rope, see Fig. 3.12. The distance between the two poles was set to be enough so that their angular separation as seen from radar position was more than the angular difference between the secondary azimuthal antenna sidelobes. This ensured that the sidelobe-to-sidelobe backscattering from the pole structures would be attenuated enough to avoid disrupting the backscattered calibration target signal. The height of the poles was determined experimentally on a basis of reducing ground illumination by antenna mainlobe and first sidelobe at the calibration target range. The resulting geometry prevents the multipath effects as well. The sphere can also be lifted high above the ground using a weather balloon that has wire bracing to hold it steady, see Fig. 3.13. This method, however, is more laborious to set up and suffers from wind gusts, so it was not used as much as the poles.

The calibration range, when using spheres as targets, must be considered from three viewpoints. Firstly, the far-field criterion must be fulfilled. Due to the small physical dimensions of our calibration spheres, the far-field distance was based on the radar antenna diameter. On the other hand, the range can not be too long, because in order to avoid ground illumination at the calibration target range the mounting poles height would have to be increased with increasing range. Already at a distance of a few hundred meters the poles would be impractically tall.

The achievable measurement accuracy is also a function of signal-to-noise ratio, which sets a limit for the maximum range of calibration arrangement. In a diode detector the rectification of AC signals is provided by the even-order terms in the power-law representation of diode equation [93, Ch. 11]. For small signals the second order term dominates, and therefore the output voltage of a diode detector is proportional to the square of the

Figure 3.12: *A spherical calibration target mounted between two poles using nylon rope. The markings on the rope are for angular distance determination. The sphere position is marked with an arrow.*

Figure 3.13: *A calibration sphere (marked with an arrow) lifted high above the ground using a weather balloon with wire bracing to hold it steady.*

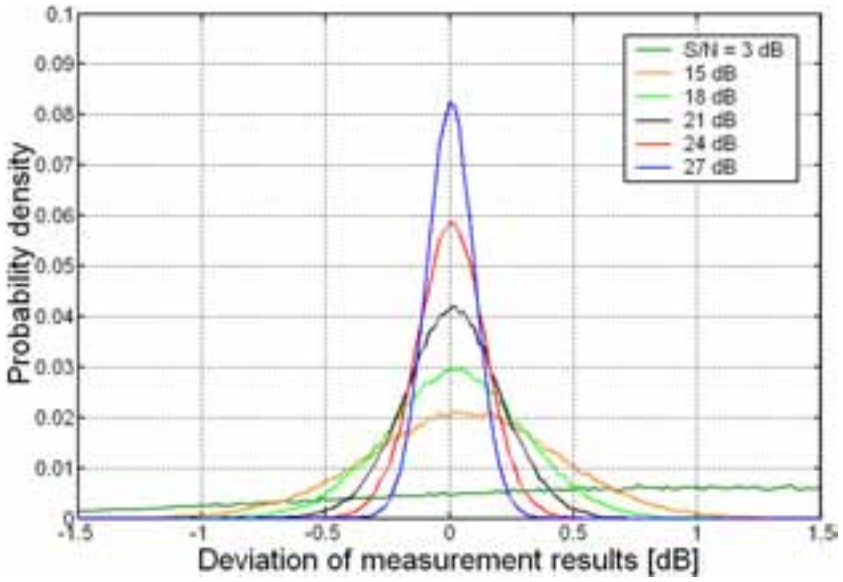

Figure 3.14: *Probability density curves of calibration error due to thermal noise for various signal-to-noise ratios. The calibration target is assumed non-fluctuating and noise has Gaussian distribution.*

input RF voltage. Measurement uncertainty caused by thermal noise can be evaluated in Matlab by adding Gaussian noise to the non-fluctuating target echo signal before squaring and low-pass filtering the IF signal. The resulting envelope voltage represents the noise-contaminated calibration target echo. When the process is repeated for several values of signal-to-noise ratio, a set of probability density curves is obtained. The measurement uncertainty simulations are shown in Fig. 3.14. The results indicate, that for example in case of $S/N = 15$ dB the error in estimation of calibration target RCS for 95% of the time is less than ± 0.7 dB, whereas for $S/N = 24$ dB the measured RCS is practically always within the ± 0.7 dB error bounds. Based on the above evaluation it was found, that in order to achieve better than ± 1 dB calibration uncertainty, the maximum ranges for the smallest and largest calibration sphere were approximately 70 and 150 meters when using our K_a- and V-band radars. At V-band these ranges were all in far field region, whereas the smallest sphere at K_a-band turned out to be unfit for calibration purposes since it would have to be inside the near field zone to fulfill the signal-to-noise ratio requirement. The calibration of our radar systems was typically carried out using the second largest sphere located at 100 meters for K_a-band and the largest sphere located at 70 m for V-band. These provide signal-to-noise ratios of 18 dB for K_a-band and 15 dB for V-band. The corresponding 95% confidence intervals are ± 0.6 dB and ± 0.7 dB.

To be able to perform calibrations at longer radar ranges, a rectangular plate as a target was considered. Rectangular plates are known to produce large radar cross sections, and the analytical form is [92, Ch. 4]

$$\sigma(\theta,\varphi) = \frac{4\pi A^2}{\lambda^2}\left[\frac{\sin(ka\sin\theta\cos\varphi)}{ka\sin\theta\cos\varphi}\frac{\sin(kb\sin\theta\cos\varphi)}{kb\sin\theta\cos\varphi}\right]^2\cos^2\theta, \tag{3.15}$$

where a and b are the plate dimensions, A is the physical area of the plate and k is the

wave number. Reasonable mechanical dimensions of some tens of centimeters give an RCS of several hundred or thousand square meters, but only for perfectly perpendicular incidence. The relative RCS of a square plate in azimuth direction is shown in Fig. 1 of [P7] and the extremely narrow beamwidth of a square plate is further illustrated in Fig. 2 of [P7]. If the radar antenna beamwidth and that of the calibration target are wide enough to cover at least partially the soil or sea surface between them, we may get up to 16 times larger input power to the radar if all the four paths add in phase, as was discussed in 2.1.2. Therefore it is advantageous to have the target's equivalent beam as narrow as practical. This is in our case the main reason of discarding typical corner reflectors, which indeed would give easier alignment possibilities due to their wider main beam widths [94]. Observing all this, a reliable way to align the plate perfectly perpendicular to the radar beam had to be devised.

The calibration target with an alignment system is shown in Fig. 3.15. It consists of a wooden tripod, a two-axis rotating mechanism, the actual calibration plate and an optical sight. Special care has been taken to avoid any metallic surfaces to protrude outside the actual circumference of the rectangular aluminum plate, and therefore the optical sight has been mounted directly behind the plate and only a hole having a radius of 4 millimeters is provided for looking through. The azimuth and elevation axes have nylon threads that enable a complete 360-degree coverage of the horizon and about 30 degrees above and below it. The gear reduction ratio is chosen as 1:100, which allows steady and accurate optimization of alignment with reference to the radar beam direction. Collimation of the optical sight was done with a laser pointer and a tiny mirror attached on the surface of the plate. Naturally, the surface deformations of the plate itself have been kept below $\lambda/32$ - a value not too difficult for such limited maximum dimensions [95]. In order to be able to adjust the calibration target RCS without modifying the collimated alignment system, different absorber collars, which are mounted from above just by two floating hinges, were used. Additionally, the corner diffraction of the plate is reduced by using the absorber collars.

Figure 3.15: *The calibration target with an alignment system consisting of a wooden tripod, a two-axis rotating mechanism, the actual calibration plate and an optical sight. An absorber collar can be used to vary the RCS of the plate and reduce the corner diffraction (left).*

The mechanical alignment in the field turned out to be very repeatable procedure, and calibration ranges up to several kilometers were used. The optical sight approach is very practical and gives an unambiguous way for pointing. Because the beamwidths of the target and illuminating radar are very narrow ($< 1°$), the multipath effects are avoided and therefore the use of high measuring towers is not necessary.

The estimation of the calibration target RCS proved to be difficult without storing and post-processing of the radar data. Due to the square law detection, strong echo voltages appear to be strongly fluctuating when observed on an oscilloscope display (Fig. 3.16). These fluctuations, however, represent received power changes in the order of only 1-2 dB. This phenomenon is illustrated using a $P_{in} - U_{out}$ -detection curve in Fig. 3.17, from which it becomes obvious, that absolute voltage fluctuations for large S/N echoes are larger than for those with smaller S/N, even though the received power distributions would be identical. Averaging over 4 to 16 pulse repetition intervals calms down the radar signal on a display, but true mean values of the received calibration signal were obtained from post-measurement analysis of the captured radar data.

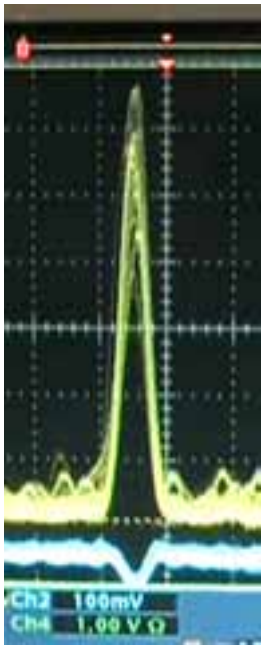

Figure 3.16: *An example of radar echo voltage fluctuations on an oscilloscope display.*

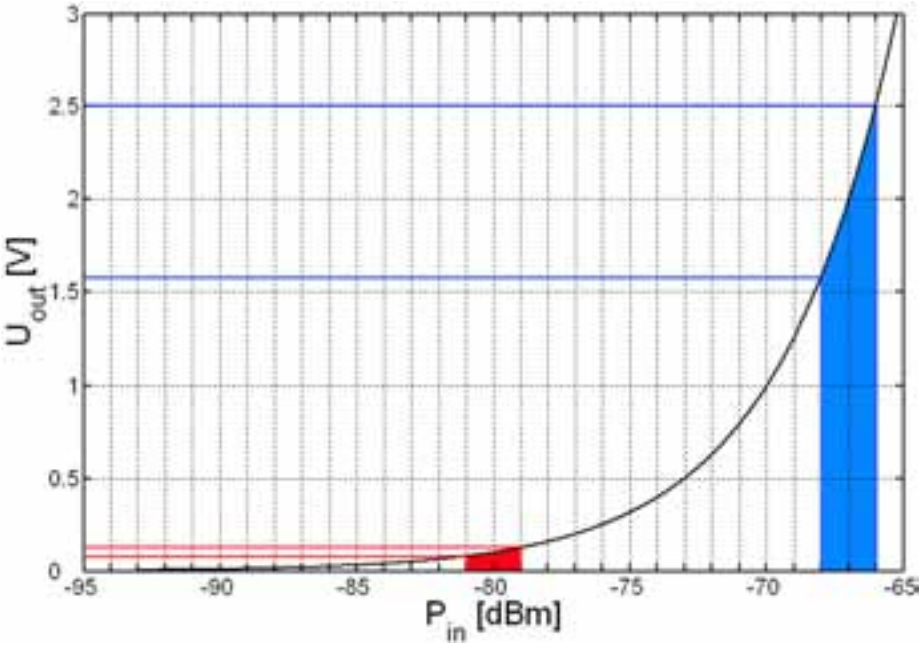

Figure 3.17: *Voltage fluctuations for small and large input power pulses having equal input power distribution illustrated using a $P_{in} - U_{out}$ -detection curve. The red and blue areas show, that power variations of $\pm 1dB$ for large and small mean input power levels result in completely different detector output voltage variations.*

3.4.2 Transmitter calibration

In addition to the use of passive targets, an external calibration action before the start of each field measurement event was also conducted using a stand-alone receiver to monitor the power density radiated by the test radar. The structure of the receiver was made simple using only an LNA and bandpass filter connected to a diode detector followed by

fast wide-band video amplifier to provide the output voltage. The antenna was a circular horn supplemented by a dielectric lens. A photograph of the receiver is shown in Fig. 3.18. The receiver was mounted on a tripod, whose height was adjusted experimentally so that the geometry would prevent severe multipath effects. Due to the wide beamwidth of the calibration receiver antenna, however, multipath propagation from radar antenna sidelobe to the calibration receiver antenna could not be entirely avoided. The power level changes introduced by multipath effects were examined each time by slowly varying the calibration receiver height to see the difference between maximum and minimum signal level. If the difference was more than 1 dB, the actual position of the calibration receiver was moved until the geometry was such that the observed difference was on an acceptable level (≤ 1 dB).

The calibration receiver detection curve, in its part, was measured using a CW transmitter at a center frequency of the receiver bandpass filter. Furthermore, knowing the gain of the calibration receiver antenna and the test radar transmitter power at the antenna port based on laboratory measurements, the maximum gain of the test radar antenna could then be calculated using

$$G_t = \left(\frac{P_r}{P_t}\right)\left(\frac{4\pi R}{\lambda}\right)^2 \frac{1}{G_r}. \tag{3.16}$$

The transmission line loss of the antenna feed as well as the power loss due to SWR $>$ 1 at the antenna interface are effectively included in the value of G_t. In addition to the maximum gain, also the 3 dB and 1.5 dB beamwidths of the test radar antenna mainlobe (see 3.2), as well as the first and second sidelobe level, could be determined when using the calibration receiver method. The measurements were carried out by changing the azimuthal pointing angle of a radar and observing the corresponding changes in power level at the calibration receiver. For the measurement of the elevation beam pattern the

Figure 3.18: *The calibration receiver. The output video voltage of the calibration receiver was sent back to the radar location using a coaxial cable.*

radar was tilted 90 degrees in order to avoid generating multipath interference caused by changes in elevation angle. There was no concern of cross-polarization attenuation since the dynamic range of the calibration receiver is 26 dB, allowing mainlobe beamwidth measurements also in cross-polarization situation.

3.4.3 Active receiver calibrator

In the calibration of air- and spaceborn synthetic aperture radars (SAR) active radar calibrators are widely used over passive targets due to the background condition requirement [96]. The devices are essentially of transponder type, which re-radiate the received waveform back towards the radar using a transmission power level that corresponds to a predefined RCS value. When calibrating a ground-based millimeter wave radar receiver unit, the use of a transponder is not necessary, since the calibration distances are significantly shorter than for typical SAR applications. Therefore the calibration transmitter can be synchronized with the radar pulse unit through a cable connection. A sample of the transmitted waveform can be fed to the calibrator if signal distortion can be avoided, but even if the transmitted waveform has to be generated separately, a hardware solution of a transmitter alone is more straightforward than a complete transponder unit. In order to avoid the mixing of the synthetic calibration signal and the actual backscattered echo from the calibration instrument, a possibility to shift the calibration pulse to a low backscatter area is desirable. This can be accomplished by controlling the transmission instance of the calibrator relative to the radar pulse transmission. On the other hand, since the aim is to calibrate the receiver, the radar transmitter can be turned off in case a pulse shifting control is not available. This, however, prevents getting any ideas of e.g. saturation recovery. During the thesis work preliminary experiments using a calibration transmitter were carried out, but the implementation into practice did not take place yet. An example of our first hardware is shown in Fig. 3.19. Given the three kind of calibration methods used (laboratory measurements, passive targets and calibration receiver), the obtained precision of absolute calibration did not necessitate the use of calibration transmitter.

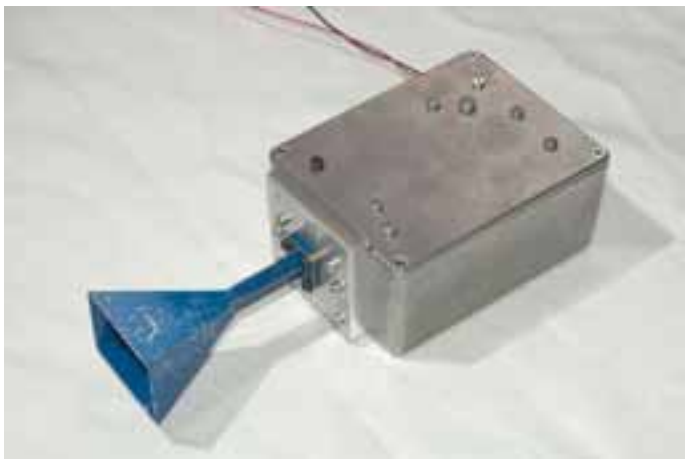

Figure 3.19: *The calibration transmitter prototype. Only preliminary experiments were conducted in the field with this transmitter.*

3.4.4 Uncertainty issues

Solely for the purposes of the measurements presented in this thesis, the following parameters are defined:

Stability. Electrical stability of the instrumentation radar between successive calibrations, typically within a time span of 0.5-2 hours. Based on our calibration data, the stability uncertainty is better than 0.5 dB.

Laboratory measurement uncertainty. The most significant sources of laboratory measurement uncertainties are related to transmitter power measurements and to the determination of detector $P_{in} - U_{out}$ -curve. The power measurement uncertainty is found to be 0.3 dB and detector curve determination 0.2 dB @1V.

Site uncertainty, which takes into account the temporal changes in test environment and unexpected changes in calibration target. For most cases the changes in environment are not a practical issue, since the test sites were chosen to avoid severe sidelobe clutter interference. The calculated uncertainty was found to be below 0.4 dB.

External unknown signals. The presence of an external signal manifests itself as an increase in noise floor. An increase of 3 dB or more in noise level would be easily detected, but such a phenomenon was not encountered during our measurements. Therefore the uncertainty caused by external interference for practical target echo levels (detected video level of $>$1V) is below 0.1 dB.

Weather uncertainty. The effect of temperature on system performance was corrected separately using an experimentally determined correction factor (see Fig. 4.14). The uncertainty in calculation of atmospheric attenuation is below 0.2 dB.

Repeatability. The repeatability, in case we want to measure a same target at different sites, was found to be better than 1 dB.

Based on quantitative analysis of individual error sources, the overall 95% root-mean-square uncertainty of our measurement results is 1.2 dB. Furthermore, the electrical stability between calibrations is better than 0.5 dB.

4 Effects of Scandinavian environment on radar wave propagation

In this chapter the results of backscattering measurements are presented. The data is obtained using the K_a- and V-band (3.3) instrumentation radars and calibration methods described in 3.4. The purpose of collecting backscattering data is to provide tools for developing signal processing algorithms for millimeter wave frequencies, since true radar data is superior to simulated clutter. Furthermore, our data covers some typical illumination geometries which will be encountered using a ground-based radar system, namely perpendicular illumination and very low grazing angles. No backscattering data for V-band can be found in open literature, and the reported K_a-band measurements do not cover low grazing angles or perfectly perpendicular illumination.

The backscattering measurement results presented here depict essentially raw radar data obtained from true clutter sources. Creation of mathematical models based on the measured data or fitting known probability distribution functions into the data have not been attempted, and they are out of the scope of this thesis. Only basic statistical figures are given for each case.

4.1 Data acquisition methods

Radar data in field experiments is conveniently presented in an A-type display using an oscilloscope. The IF- and pulse unit provides a triggering pulse for the oscilloscope, allowing the amplitude and phase channels to be presented simultaneously on the display. However, capturing and storing the radar data can not be accomplished with standard laboratory measurement devices because the amount of samples that need to be captured is huge and an oscilloscope is not capable of transferring the data to PC memory via HP-IB bus with desired speed. In order to be able to analyze raw radar data in Matlab environment, a need for a signal collecting system arose.

The primary data aqcuisition system was based on a PC oscilloscope card CS12100 by the Canadian company Gage Applied Technologies. The card was installed into PCI bus of an ordinary office PC. CompuScope 12100 samples analog signals at speeds up to 100 MS/s with 12 bit resolution and stores the data in an on-board memory. CS12100 uses two monolithic sub-ranging A/D converters, each running at 50 MHz, to provide a dual-channel simultaneous real-time maximum sampling rate of 50 MS/s. The oscilloscope card is controlled by dedicated software, that enables all necessary oscilloscope functions. The card is equipped with an 8 MB on-board memory size. The on-board memory size restricts the data aqcuisition time, which is a function of sampling rate, amplitude resolution and posttrigger sample count. In our case we were able to collect data for a maximum of 1.3 seconds at a time, which was quite enough for backscattering measurements, (Fig. 4.1).

Figure 4.1: *An oscilloscope was used for displaying radar data in real time. The backscattering data was captured for further analysis using a PC-based data acquisition system.*

In order to study the temporal behaviour of radar echoes over a time period of several seconds, longer data acquisition times than the PC-based system was able to provide were needed. This was achieved by simply videotaping the oscilloscope display (Fig. 4.2). Such a method enables to capture 25 snapshots of the radar data in one second, which is sufficient sampling rate for example studies concerning slow-fading effects. Once the video material is stored into a DVD, the radar data can be extracted from the video frame by frame. Rain backscattering and attenuation measurement campaigns lasting for several weeks called for yet another method to collect and store the radar data. Here, an old portable workstation HP-85 performed data logging by reading the time-gated results

Figure 4.2: *Videotaping the oscilloscope display provided a simple method for capturing radar data over a time period of several seconds.*

Figure 4.3: *The data of measurement campaigns lasting uniterruptedly for several weeks was captured and stored using an oscilloscope and a portable workstation.*

from an oscilloscope through an IEEE-488 interface (Fig. 4.3). Raw results were printed immediately on paper and stored as blocks on 3.5 inch disk, whereby at least part of the data would be saved even in the case of total power failure.

4.2 Formulation of clutter statistics

The clutter data was measured from spatial areas within radar line-of-sight in which clutter levels were substantially over the thermal noise level. The radar was positioned and aligned to illuminate a selected clutter cell continuosly so that several thousands of samples could be captured and stored. The backscattering coefficient (σ^0) was derived from recorded clutter data (using Equations (3.6), (3.8) and (3.9)), the results were transformed into a histogram form, and basic statistical attributes were calculated. Together with descriptive information of the terrain or forest type, the histogram and associated statistical attributes were stored into a clutter database. In this thesis a few examples from this huge database are given to describe typical values of σ^0 in different environments characteristic of Scandinavian topography. Histograms are presented and statistical attributes are given in separate tables for each presented case. They include mean and standard deviation, coefficients of skewness and kurtosis as well as the 50-, 95- and 99-percentile levels.

The backscattering coefficient distribution in each histogram is presented with 0.5 dB bins. The amount of samples used to create the histograms is either 2^{13}, 2^{14} or 2^{15}, due to the data aqcuisition system characteristics. The histograms are normalized to view the height

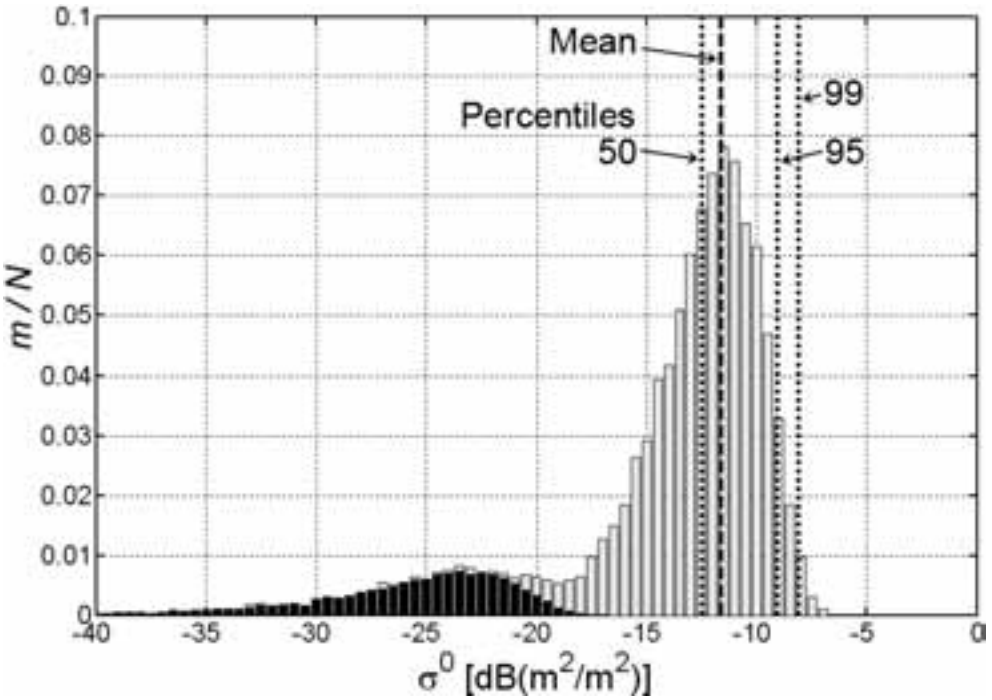

Figure 4.4: *Illustration of a clutter backscattering coefficient histogram. Thermal noise (black bars) shapes the histogram in case clutter echoes are close the sensitivity limit of the receiver. Basic statistical attributes have been marked.*

of the bars as fractions of the total number of samples. When clutter data was measured, it was assured that the echoes are below the top end of the dynamic range of the receiver. Therefore, none of the clutter samples were saturated, and the right end of the histograms represent a true form of the distribution. However, most of the clutter distributions were such that the tails towards the low backscattering end of the histograms were long, and thermal noise floor could not be avoided in all cases [68, Appendix 4C]. The distortion of the clutter backscattering coefficient histograms caused by finite sensitivity of the radar is illustrated in Fig. 4.4, where the receiver noise is shown with black bars. In histograms of sections 4.3 and 4.4 the bars representing receiver thermal noise have been omitted to preserve good readability. The bar heights present the fractional amount of samples as m/N, where N is the total number of samples.

The average clutter conditions have been described by different authors with mean, mode and median values [68]. In this thesis mean values are given. The percentile levels are given for 50%, 95% and 99%, which indicate the relative portion of samples below a given backscattering coefficient value. The mean- and percentile levels are illustrated in Fig. 4.4. The statistical attributes were computed from the individual samples x_i of the raw backscattering coefficient data, and are defined as follows [68, pp. 129-130]:

$$\text{mean} = \bar{x} = \frac{1}{N}\sum_{i=1}^{I} n_i \bar{x_i} \tag{4.1}$$

$$\text{standard deviation} = \text{std}(x) = \left[\frac{1}{N-1}\sum_{i=1}^{I} n_i(\bar{x_i} - \bar{x})^2\right]^{\frac{1}{2}} \tag{4.2}$$

$$\text{skewness} = g_3(x) = \frac{M_3(x)}{[M_2(x)]^{3/2}} \tag{4.3}$$

$$\text{kurtosis} = g_4(x) = \frac{M_4(x)}{[M_2(x)]^2} \tag{4.4}$$

where

$$M_q(x) = \frac{1}{N}\sum_{i=1}^{I} n_i(\bar{x_i} - \bar{x})^q \quad ; q = 2, 3, 4. \tag{4.5}$$

4.3 Backscattering from ground

Low grazing angle backscattering coefficients of three types of soil are presented for V- and K_a-band. Such terrain types, in which the soil material consists almost completely of clay with only minor vegetation on top, are labeled "clay". The label "grass+gravel" refers to a terrain type which has a thick gravel layer as surface material, and vegetation, mainly grass, covers significant portion of the area. A snow-covered ground has been further divided into two main categories, namely "wet"- and "refrozen snow". The division has been made based on an observation, that the backscattering coefficient of snow changes dramatically whenever a melt/refreezing cycle occurs [67, p. 145].

Figure 4.5 presents histograms of the selected cases at V-band, and Figure 4.6 at K_a-band. The corresponding statistical attributes are given in Table 4.1. The open literature con-

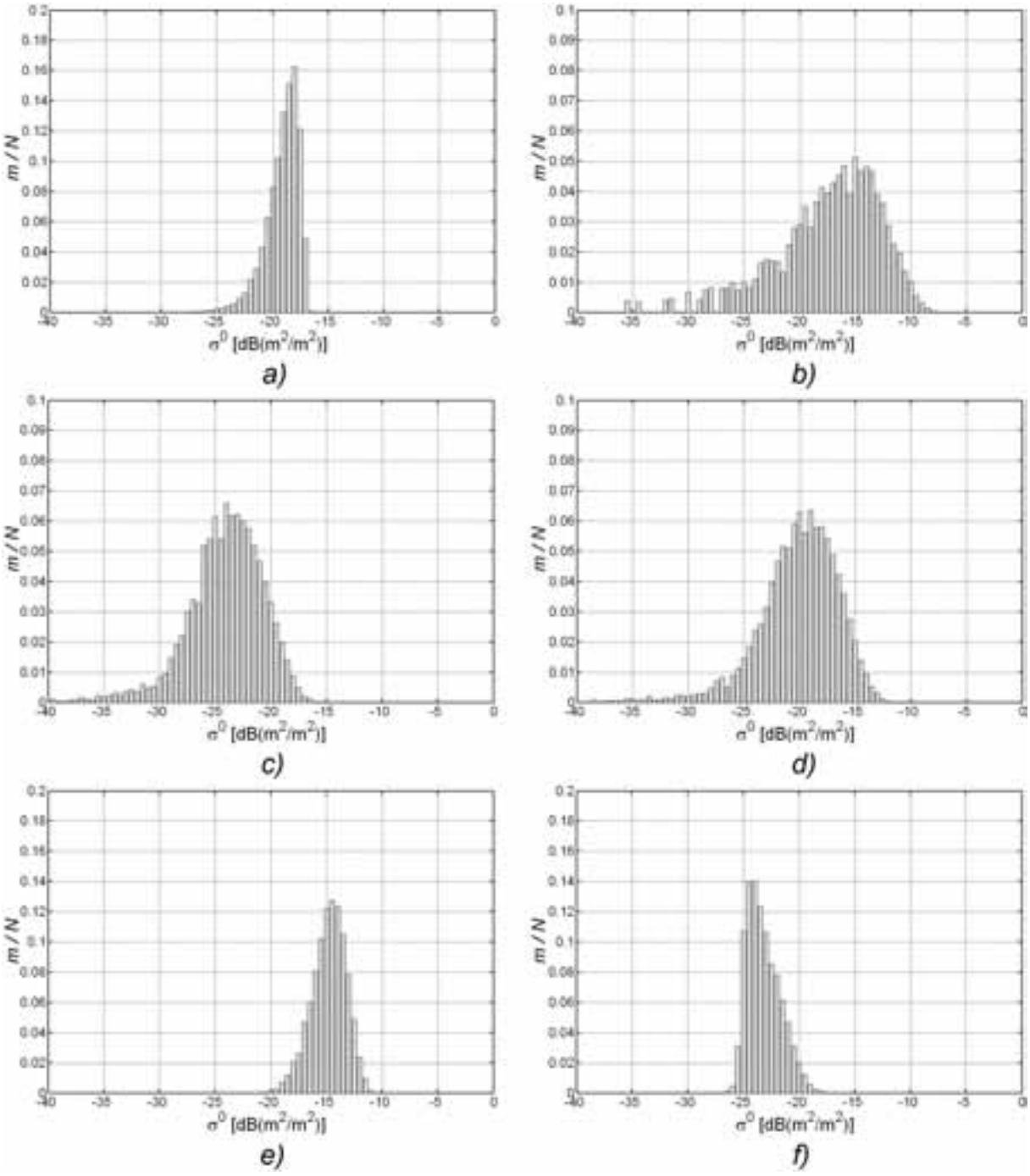

Figure 4.5: *Ground backscattering coefficient values at V-band from our measurements: a) Soil type clay, grazing angle* $\phi = 1.5°$*, b) clay,* $\phi = 3°$*, c) partly gravel and partly grass,* $\phi = 1°$*, d) partly gravel and partly grass,* $\phi = 3°$*, e) refrozen snow,* $\phi = 1°$*, f) wet snow,* $\phi = 1°$*. The statistical attributes of the histograms are presented in Table 4.1.*

tains reports of several experimental millimeter wave ground reflectivity measurement campaigns [67, 97, 98, 99, 100, 101, 102, 103, 104, 105], but extremely low grazing angle data ($\phi < 3°$) has not been reported for K_a-band, and open literature completely lacks results for V-band radar reflectivity. Therefore direct comparisons with previous work are not possible.

Most of the theoretical models proposed by many authors are not valid for low grazing angles, see e. g. [106, 107]. However, ground clutter models for K_a-band proposed by Georgia Tech [67, p. 147] and Kulemin [97, p. 121] extend below grazing angles of 10°, thus providing a possibility to compare our results against these models. In Figure 4.7 the two models and our measurements are plotted for comparison. It can be seen, that Kulemin's model predicts more than 10 dB lower values than what is suggested by our measurements. On the other hand, direct extrapolation of Georgia Tech model gives about 10 dB higher backscattering coefficient values for snow-covered ground than our results indicate, although a good agreement can be found for the difference between wet and refrozen snow, which is in the order of 10 dB according to our measurements and

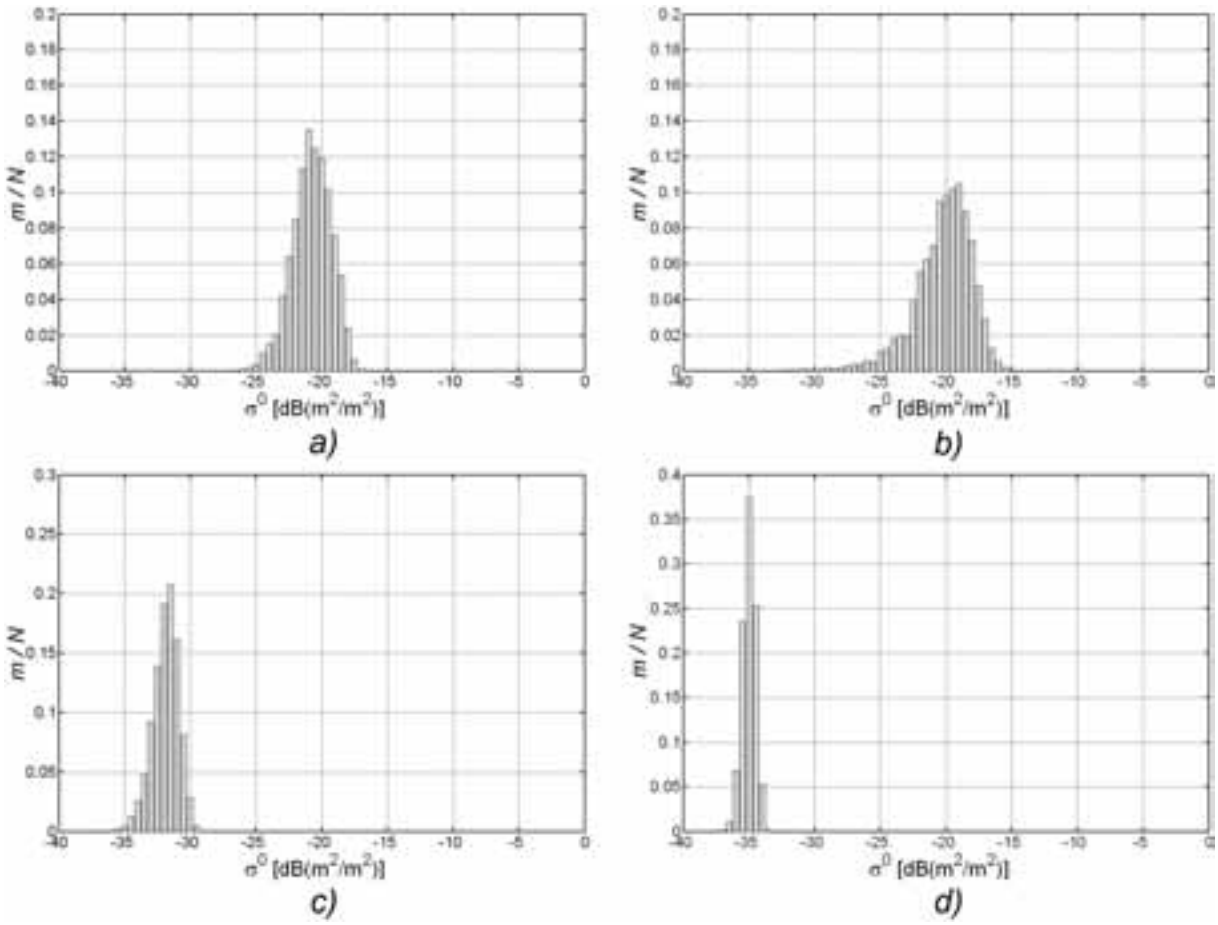

Figure 4.6: *Ground backscattering coefficient values at K_a-band from our measurements: a) Soil type clay, grazing angle $\phi = 1°$, b) clay, $\phi = 1.5°$, c) wet snow, $\phi = 3°$, d) wet snow, $\phi = 1°$. The statistical attributes of the histograms are presented in Table 4.1.*

Table 4.1: *Statistical attributes of ground backscattering coefficient at V- and K_a-band for different soil types from our measurements.*

Figure	Soil type	ϕ [°]	Mean [dB]	Std [dB]	g_3	g_4	50% [dB]	95% [dB]	99% [dB]
V-band									
4.5 a)	Clay	1.5	-18.9	-24.2	-0.276	2.487	-18.8	-18.0	-17.2
4.5 b)	Clay	3	-15.7	-16.0	1.233	5.087	-16.6	-11.1	-9.7
4.5 c)	Gravel+grass	1	-23.0	-24.5	1.299	5.455	-23.8	-19.2	-17.8
4.5 d)	Gravel+grass	3	-19.0	-20.4	1.235	5.228	-19.7	-15.1	-13.7
4.5 e)	Refrozen snow	1	-14.5	-19.2	0.503	3.045	-14.7	-12.5	-11.7
4.5 f)	Wet snow	1	-22.9	-27.0	1.630	6.695	-23.5	-20.4	-19.3
K_a-band									
4.6 a)	Clay	1	-20.5	-25.3	0.511	2.958	-20.7	-18.5	-17.8
4.6 b)	Clay	1.5	-19.7	-23.4	0.474	3.174	-19.9	-17.3	-16.4
3 [P9]	Gravel+grass	3	-21.7	-37.2	0.145	2.748	-21.9	-20.2	-19.8
4.6 c)	Wet snow	3	-31.8	-38.3	0.139	2.950	-31.8	-30.4	-29.9
4.6 d)	Wet snow	1	-35.0	-44.3	0.052	2.982	-35.0	-34.2	-33.9
4 [P9]	Refrozen snow	3	-23.9	-24.9	0.484	3.211	-24.0	-21.5	-20.6

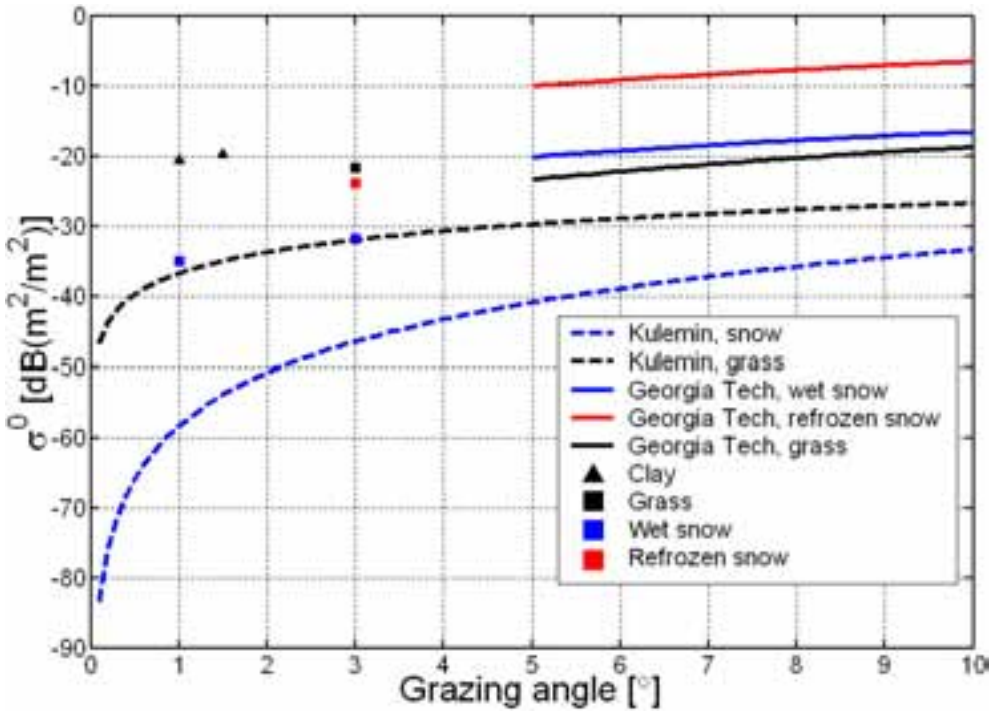

Figure 4.7: *A comparison between our measurement results, Kulemin [97, p. 121] ground backscattering model and Georgia Tech [67, p. 147] backscattering model. The Georgia Tech -model covers grazing angles down to 5°.*

Georgia Tech model. Summertime ground reflectivity in our measurements seems to be higher than what is proposed by the models. An interesting feature is the relation between summertime and wintertime reflectivity. According to our measurements, and Kulemin as well, the summertime reflectivity is always stronger than that of snow-covered ground whereas the Georgia Tech model suggests opposite behaviour.

Generally, the backscattering levels at V-band are stronger by 2-4 dB compared to K_a-band, and narrower statistical distributions are observed at K_a-band than at V-band regardless of clutter type. A terrain consisting mainly of clay seems to produce stronger backscattering (2-4 dB) than a "gravel+grass" -type soil, as was the case also at K_a-band, although the phenomenon at V-band is more pronounced. Snow reflectivity at V-band shows very interesting characteristics compared to summertime ground reflectivity. At grazing angle of 1° the refrozen snow has reflectivity values around -15 dB(m^2/m^2) and wet snow -23 dB(m^2/m^2), see Table 4.1. The difference between these two snow covered ground types is similar to the K_a-band behaviour, but when compared to summertime ground reflectivity, the V-band differs from K_a-band. Refrozen snow reflectivity to backscattering direction at V-band is larger by more than 4 dB than the summertime values whereas at K_a-band the summertime ground reflectivity according to our measurements always exceeds that of any type of snow. A direct scaling of K_a-band values into 60 GHz can not be done, since the behaviour at V-band is quite different from K_a-band behaviour.

4.4 Characteristics of forests and vegetation

In this section backscattering coefficients of distributed clutter under perfectly perpendicular illumination geometry conditions at V- and K_a-band are presented. The selected examples include two types of deciduous bushes, typical Scandinavian forests and single spruce and pine trees. Figure 4.8 presents measured reclectivity histograms for deciduous bushes, coniferous forests and two types of single tree at V-band. Figure 4.9 presents histograms of different forests at K_a-band. The corresponding statistical attributes are given in Table 4.2.

No reflectivity values have been published for perpendicular incidence at typical millimeter wave radar frequencies. Publications, such as [108], have concentrated on airborne measurements of forest backscattering. Maximum grazing angles used in remote sensing are in the order of 70°. Furthermore, airborne sensors see mostly the tree-tops since they illuminate the forests from above, which is completely different situation than when a ground-based sensor illuminates forests. Therefore there is no data in literature available for comparison at V- or K_a-band.

The measurement results of perpendicular illumination of dense coniferous forests show 4 dB higher backscattering coefficient values for K_a-band than for V-band. This is contrary to ground clutter case, where V-band reflectivity was generally higher than that of K_a-band. The standard deviations of backscattering coefficient data are very similar for both bands, which also differs from ground clutter case. It seems that our observations don't encourage a straight extrapolation of previously obtained 70° grazing angle data of [67] or [109] towards higher grazing angle values. If such an attempt is made, the extrapolated

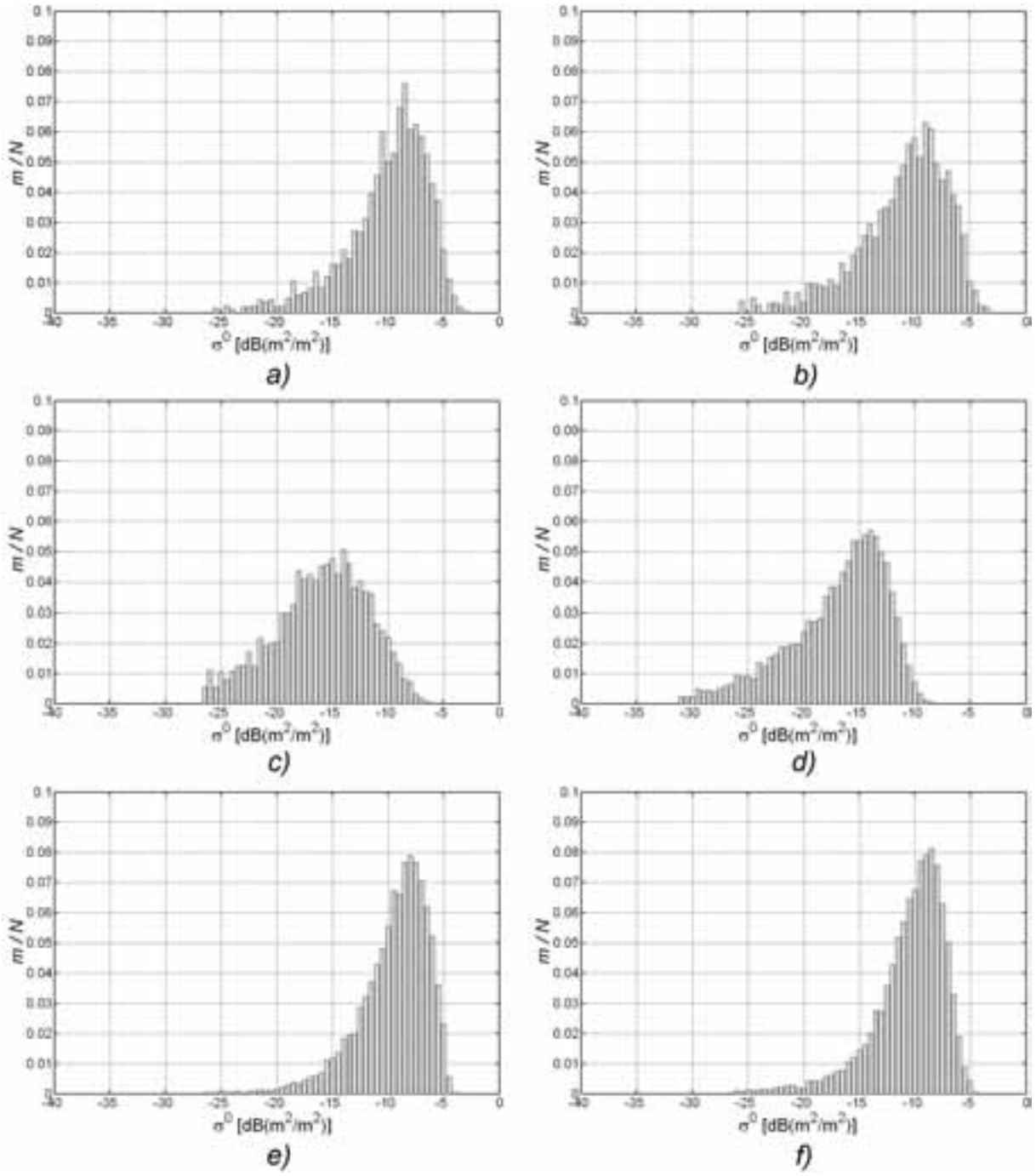

Figure 4.8: *Backscattering coefficient values of perpendicular incidence at V-band from our measurements: a) deciduous bush, b) deciduous bush, c) dense coniferous forest, d) dense coniferous forest, e) single spruce tree, f) single pine tree. The statistical attributes of the histograms are presented in Table 4.2. Measurements of a) and b) as well as c) and d) were conducted on separate occasions.*

values tend to be 5-10 dB too low. This can be due to inaccuracies of the models caused by the fact that measured perpendicular illumination results have not been available at the time the models were created.

The temporal variations of clutter echoes from forests and other vegetation are larger than in ground clutter situation, since the twigs, leaves and needles of bushes and trees move with wind. The spectral shape of vegetation clutter has been examined by a number of authors, but mainly for frequencies less than 10 GHz. However, Currie [67] makes an attempt to associate millimeter wave spectral shapes with the findings of others at lower microwave frequencies. The low- and high frequency spectral shapes are shown to follow Gaussian and Lorentzian functions of the form:

$$W(f) = W_0 e^{-a_1 f^2/f_c^2} \quad \text{(Gaussian)} \tag{4.6}$$

$$W(f) = \frac{a_2}{1 + (f/f_L)^n} \quad \text{(Lorentzian).} \tag{4.7}$$

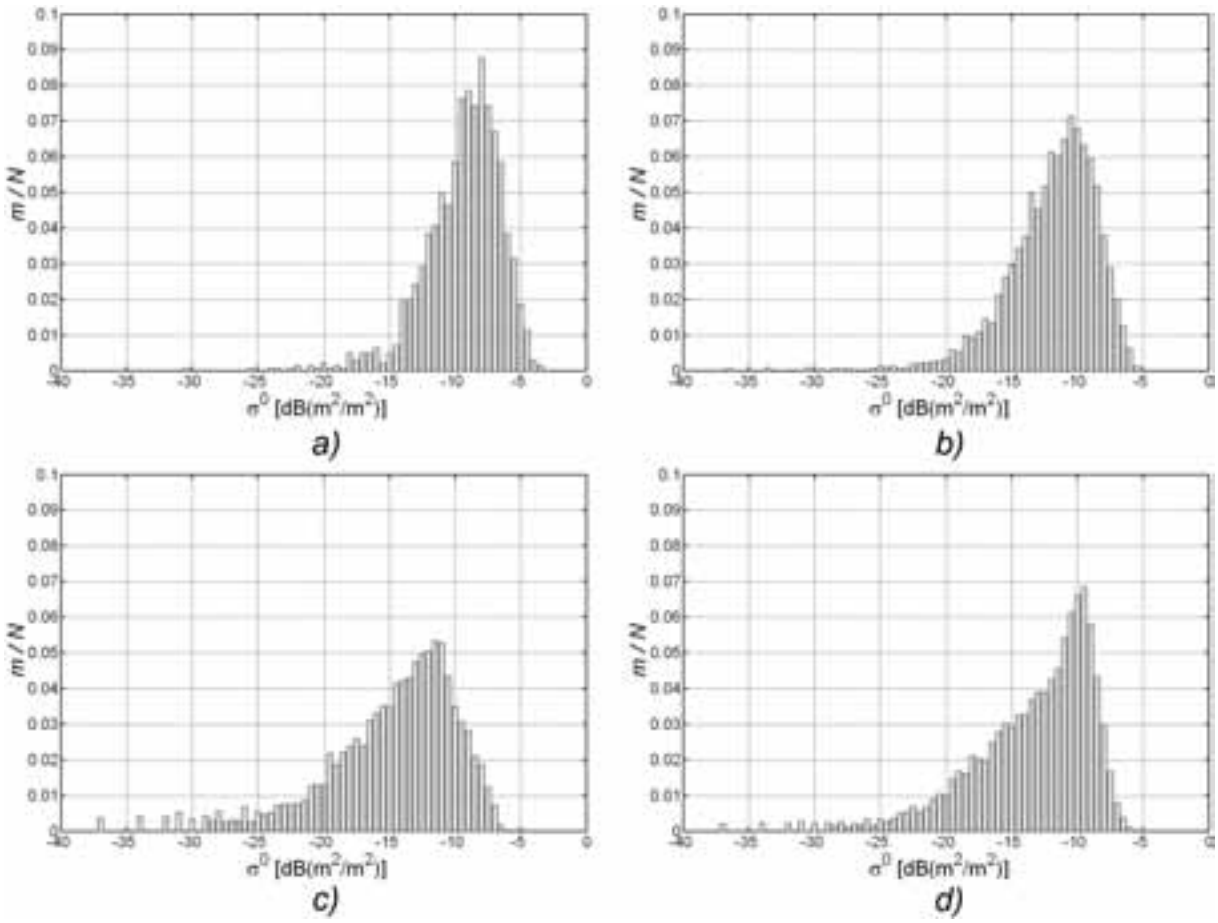

Figure 4.9: *Backscattering coefficient values of perpendicular incidence at K_a-band from our measurements: a) Dense coniferous forest, b) dense coniferous forest, c) forest dominated by pine trees, d) forest dominated by pine trees. The statistical attributes of the histograms are presented in Table 4.2. Measurements of a) and b) as well as c) and d) were conducted on separate occasions.*

Table 4.2: *Statistical attributes of perpendicular backscattering coefficient at V- and K_a-band for different bush, forest and tree types based on our measurements.*

Figure	Target type	Mean [dB]	Std [dB]	g_3	g_4	50%	95%	99%
V-band								
4.8 a)	Deciduous bush	-8.9	-10.8	0.756	3.247	-9.3	-5.5	-4.3
4.8 b)	Deciduous bush	-9.6	-11.0	0.984	3.766	-10.3	-5.8	-4.7
4.8 c)	Forest, coniferous	-14.3	-14.7	1.740	6.793	-15.7	-9.7	-8.1
4.8 d)	Forest, coniferous	-15.3	-16.4	1.001	3.891	-16.0	-11.3	-10.2
4.8 e)	Single tree, spruce	-8.7	-12.5	0.245	2.605	-8.7	-6.3	-5.7
4.8 f)	Single tree, pine	-9.7	-13.6	0.354	2.796	-9.8	-7.3	-6.6
K_a-band								
4.9 a)	Forest, coniferous	-8.6	-11.2	0.764	3.526	-9.0	-5.5	-4.5
4.9 b)	Forest, coniferous	-10.9	-12.9	0.856	3.501	-11.4	-7.4	-6.4
4.9 c)	Forest, pines	-12.8	-13.6	1.149	4.0	-13.8	-8.5	-7.3
4.9 d)	Forest, pines	-11.7	-13.1	0.643	2.8	-12.3	-8.1	-7.1

The spectral dependencies of windblown trees are characterized with 3 dB points for both functions (f_G, f_L), the exponent n of Lorentzian and a cross-over level, which is the level (below the DC component) at which the two functions cross. Table 4.3 summarizes the values proposed by Currie and the values suggested by our measurements. An example of the measured spectrum of a coniferous forest for low- and moderate wind conditions is presented in Figures 4.10 and 4.11. The Gaussian and Lorentzian function that best fit the data are shown as black curves. The spectral dependency values suggested by Currie and our measurements seem to differ quite considerably in the behaviour of high frequency components. The low frequency part of the spectrum, characterized by Gaussian shape, shows little discrepancies as well as the values for Lorentzian f_L. According to

Table 4.3: *Measured spectral dependencies of tree backscattering at K_a-band according to Currie [67] and our measurements.*

Wind	Gaussian f_G [Hz]	Lorentzian f_L [Hz]	Cross-over level [dB]	n
Currie				
Low	2.8	7	15	3
High	2.8	21	15	2.5
our measurements				
Low	2.8	10	10	1.2
Moderate	2.95	19	9.4	1.2

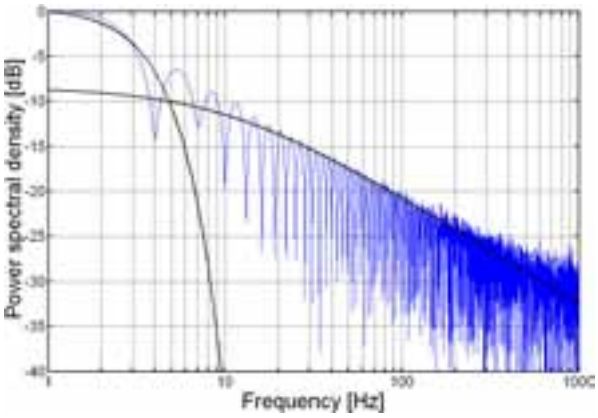

Figure 4.10: *Measured spectrum of a coniferous forest for low wind conditions at K_a-band. The low frequency part of the spectrum shape follows a Gaussian function, whereas the higher components magnitude decays on a slope described by a Lorentzian function.*

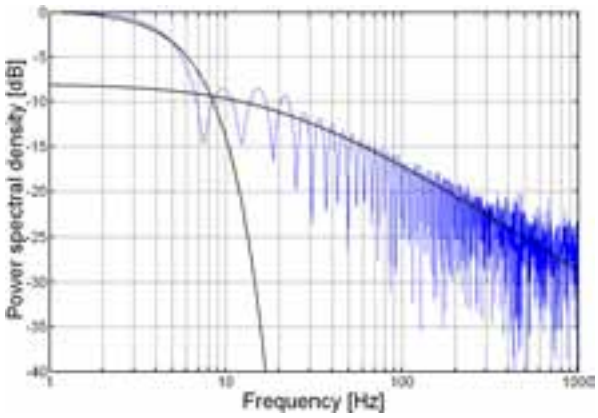

Figure 4.11: *Measured spectrum of a coniferous forest for moderate wind conditions at K_a-band. The low frequency part of the spectrum shape follows a Gaussian function, whereas the higher components magnitude decays on a slope described by a Lorentzian function.*

our measurements, however, the cross-over level is higher and the decay slope of high frequency components is not as steep as in Currie's findings. This means, obviously, that the level of frequencies at the vicinity of DC component even after an MTI-type canceller is significant, thereby degrading the signal-to-noise ratio of slow targets. The origin of stronger high frequency components than in Currie's measurements might be related to coniferous vegetation, but since the exact forest type measured by Currie is not known a meaningful comparison can not be made.

As can be found in Figures 4.10 and 4.11, the Gaussian shape does not characterize the low frequency part of the spectrum perfectly. It has been discussed in [110], although in connection to lower frequency clutter data, that certain modified exponential shapes that have the width of a Gaussian shape, but whose tails decay much faster than Gaussian, would characterize low-frequency components of windblown clutter data more accurately. However, since research work concerning fitting amplitude distributions and power spectral density functions into measured data is outside the scope of this thesis, an in-depth analysis is omitted and will be a topic of further research projects.

4.5 Rain backscattering

In order to study rain backscattering and attenuation, a short range, two-way test system operating at K_a-band was constructed. Basic elements of the system were a quasi-monostatic pulse radar, calibration target and data logging device. The radar hardware is described by Eskelinen in [111, pp. 196-199]. The calibration target consisted of a flat plate and a rotating cylindrical absorber with an opening on one side. While the absorber material of the rotating cylinber was facing the radar, background echoes were recorded.

A calibration echo from the metal plate could be received once per every revolution when the rotating cylinder had its opening facing the radar. Several thousands of pulses were averaged to obtain the two-way path loss corresponding to background and calibration target situations. An example of the raw data is presented in Fig. 4.12. The test site was constructed so, that the radar path was free of obstacles, and at the calibration target distance the main beam of the transmitting and receiving horn antennas were not touching the ground.

Figure 4.13 illustrates an example of processed results obtained under dry and rainy conditions. The blue graph depicts the backscattering level of background echoes relative to transmitted pulse power, and the red one the level of calibration target relative to transmitted pulse power. It can be seen, that due to the sidelobe-to-sidelobe vegetation clutter, exact estimates of attenuation and volumetric backscattering coefficient could not

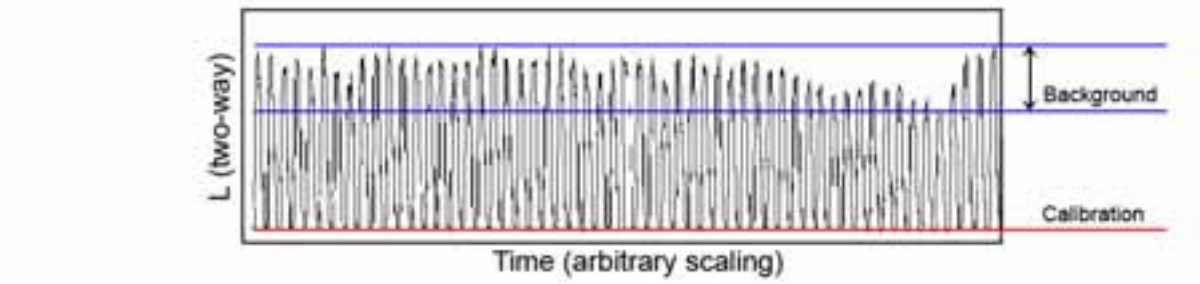

Figure 4.12: *Raw data illustrating the behaviour of calibration echos (bottom of the graph) and background level (top of the graph) on successive revolutions of the absorber cylinder. Data is measured with a quasi-monostatic test radar on a short range test site.*

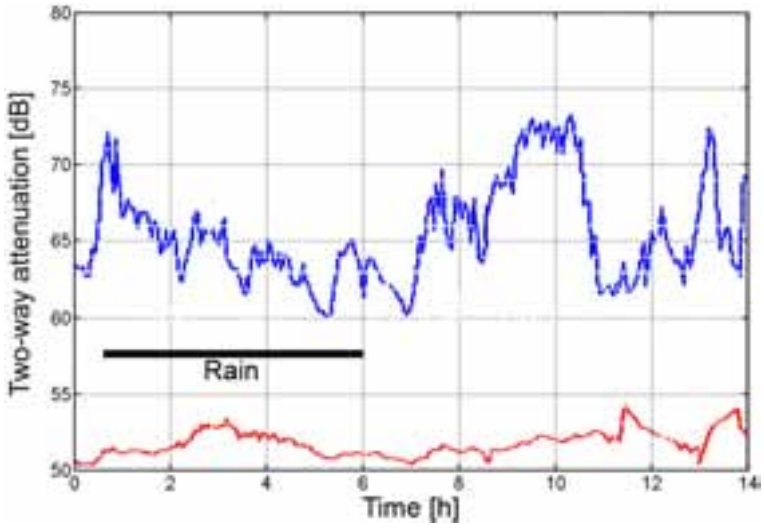

Figure 4.13: *An example of radar data obtained with a quasi-monostatic test radar under dry and rainy conditions in our measurements. The blue graph depicts the backscattering level of background echoes relative to transmitted pulse power, and the red one the level of calibration target relative to transmitted pulse power.*

be made on a basis of this data. The test showed, that in order to be able to reliably measure volumetric backscattering coefficient values, the radar antennas should be pointed upwards to the sky to avoid ground and vegetation clutter. The next test period, in fact, was carried out according to this principle. The results of this case are shown in Fig. 5 of [P1]. The recorded data showed, that the effective RCS during snowfall was increased 1-2 dB compared to effective RCS of thermal noise level with the current test setup. This indicated a maximum volumetric backscattering coefficient in the order of $\eta \approx 10^{-4}$. Still, the sidelobe clutter was present in the data causing effectively very varying noise background behaviour in the receiver. In order to reduce main beam width and antenna sidelobe level, further measurements were carried out using a monostatic test radar with a parabolic antenna.

An interesting phenomenon was observed in certain extremely cold conditions and particularly during the early dawn hours. As can be seen in Fig. 5 of [P1], the effective RCS of sky backscattering rapidly increases although the sky is visually clear in cases when the night temperature has been around -30°C or less. The reason can be found in Figs. 6 and 7 in [P1], which show simultaneous measurements of vertical temperature and humidity profiles. The heavy meteorological inversion layer, which in this case extended down to about 25 meters from ground, changes the characteristics of the two-way propagation path. The resulting increase in equivalent RCS of noise level is in the order of 10 dB. The so called angel-echoes are a known phenomenon at traditional radar frequencies (1-10 GHz), arising from areas having strong refraction index gradients, but previous reports of the phenomenon at millimeter wave frequencies are not known.

The next measurement campaign was carried out using a monostatic K_a-band test radar with its parabolic antenna pointed slightly upwards (10°). A vegetation-free test site and low sidelobe level of the antenna ensured minimal ground clutter interference. A temperature correction was performed for the detected amplitude to account for the system performance variations due to outside temperature changes. The correction factor was

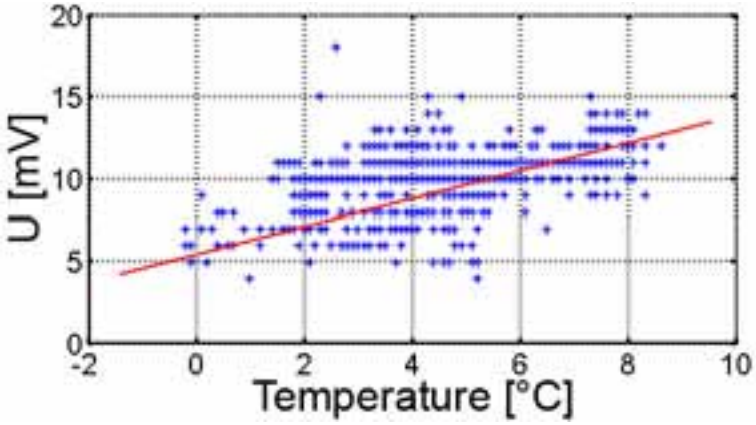

Figure 4.14: *The detected noise level amplitude as a function of the outside temperature was measured. A temperature correction factor was found by least squares fitting a slope to the measured data.*

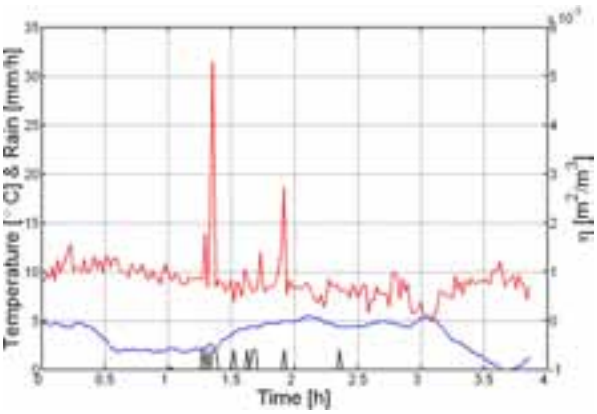

Figure 4.15: *Volumetric backscattering coefficient of rain (red curve) at K_a-band. Air temperature and rain intensity are shown with blue and black curves.*

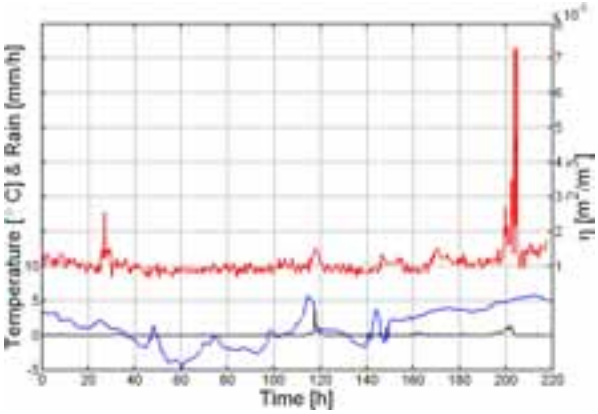

Figure 4.16: *Volumetric backscattering coefficient of rain (red curve) at K_a-band. Air temperature and rain intensity are shown with blue and black curves.*

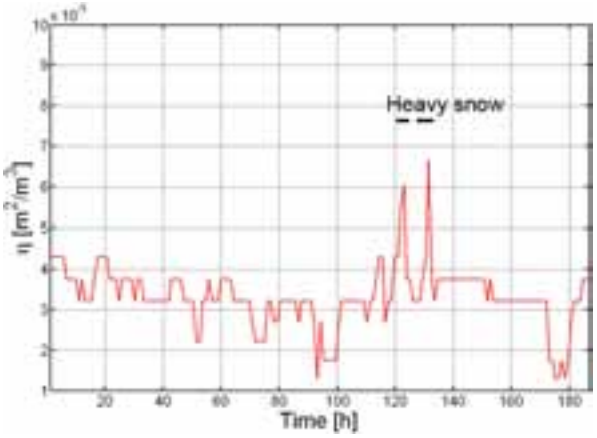

Figure 4.17: *Volumetric backscattering coefficient of snow at K_a-band. The occasions of heavy snowfall are indicated.*

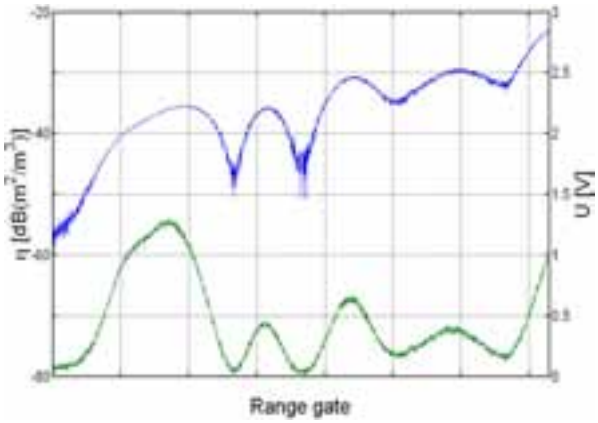

Figure 4.18: *A snapshot of an oscilloscope display during heavy rain shower (green curve) together with the corresponding volumetric backscattering coefficient (blue curve) at K_a-band.*

calculated using test results shown in Fig. 4.14. At the time of the rain measurements, the backscattering level was obtained by averaging over a time period of 20 minutes. During a six week test period in the autumn of 2003, the number of rainy days was less than expected at this time of year. Results of the few rain periods encountered are presented in Figs. 4.15, 4.16 and 4.17. The observed volumetric backscattering coefficient values range from $\eta = 1.4 \cdot 10^{-5}$ to $\eta = 7.3 \cdot 10^{-5}$ for rain and are between $\eta = 6 \cdot 10^{-6}$ to $\eta = 7 \cdot 10^{-6}$ for snow. The weather data is not collected at the exact location of the radar, but from a weather station two kilometers from the test site, which is the reason why the correlation between rain data and radar data is not perfect. The exact rain intensities at a given time are not known, but the nearby weather station recorded rain intensities

between 1-4 mm/h during the measurement campaign. Our rain measurements correlate well with the values reported by others. Currie [67] and Kulemin [97] summarize measurement results for K_a-band. Their findings for rain intensities between 1-4 mm/h are: $\eta = 1 \cdot 10^{-5}$ to $\eta = 1 \cdot 10^{-4}$ (Currie) and $\eta = 1.8 \cdot 10^{-5}$ to $\eta = 9.5 \cdot 10^{-5}$ (Kulemin). Our measured values are within these boundaries. There are no reports of snow backscattering at K_a-band, but the measurement results at 94 GHz show a 5 dB difference between snow and rain backscattering under same equivalent rain intensity conditions, the snow being less reflective. Not knowing the equivalent rain rate of our snow measurements it is difficult to evaluate the exact difference between snow and rain backscattering, but according to our results the backscattering coefficient of snow is smaller than that of rain by 4-10 dB.

Figure 4.18 illustrates a snapshot of a radar return during a heavy rain shower measured at different location than the results presented in Figs. 4.15, 4.16 and 4.17. At the time the data was captured, the radar antenna was pointing at ground 100 meters away. The range cells at which only rain clutter is present produced detected video voltages between 1.1-1.27 V, which correspond to $\eta = -37$ ... $\eta = -36$ dB[m^2/m^3]. Although no averaging is performed here, the values correlate well with previously observed volumetric backscattering coefficients of rain.

5 Examples of target RCS in millimeter wave bands

5.1 Target RCS prediction methods

As was described in section 3.4, geometrically simple objects are used for radar calibration since their radar cross section can be calculated with precision good enough for calibration purposes. The generally used equations for prediction of RCS of simple objects, such as a rectangular plate (Eq. 3.15), are, however, approximations. Exact analytical methods for the calculation of RCS of even simple objects involves solving either differential or integral equations, that describe the scattered waves under boundary conditions governed by Maxwell's equations. Even though exact solutions can be achieved in some cases, true targets require a use of more or less approximate methods, such as geometrical optics, physical optics and physical theory of diffraction [112]. The evaluation of RCS of targets is needed from two viewpoints. Firstly, radar engineers can use these figures to estimate the detection probabilities and overall radar performance in different circumstances. Secondly, in the field of military technology, RCS calculations are an essential part of the design processes, since the minimization of RCS of aircrafts as well as naval ships and armored vehicles is required.

The approximate methods of RCS prediction assume conditions where the target size is more than ten times the incidence wavelength. At millimeter wave frequencies this condition is easily fulfilled, since the targets are often hundreds of times larger than the wavelength of radar transmission. This allows to model the complex targets as consisting of separate parts, which all scatter the incident wave independently of remaining parts. The total scattered field, and thus the RCS, is obtained by integrating the induced fields of indivudual scatterers over the total surface of a target in question. In practice, though, the different parts of a target are dependent on each other and so the calculation must be extended to account for the multiple reflections arising from the shapes of a target. Often true targets have corners or other specific structures which are excellent backscatterers. Such structures cause "hot-spots" to the RCS fingerprint of a target, and especially high-resolution radars can discriminate targets based on these characteristic features.

Geometrical optics is a ray-tracing method that is solely dependent on a local radii of curvature at a specular point. A severe shortcoming of the method is that it predicts infinite values for flat or singly curved surfaces. Physical optics overcomes the problem of infinities by approximating the induced surface currents, which then act as sources for the scattered electromagnetic field. The approximation of a complex target RCS is insufficient, however, if the diffraction effects from the edges of target shapes are not in-

cluded into the results. Physical theory of diffraction was developed to take into account edge diffraction. Still, many phenomena exists that influence the total RCS of an object, such as surface travelling waves and creeping waves, that are not included in any of the methods mentioned above.

The number of commercially available RCS prediction softwares is limited, and often the analytical methods the softwares use are not well documented. A typical approach is to use a suitable combination of elementary methods to calculate the surface currents using a user selectable grid size. As the grid size is decreased, the time required for computation increases rapidly. At millimeter wave frequencies, due to the relation between wavelength and physical dimensions of a target, the required size of the individual elements of the grid often becomes smaller than allowed by the program. Even though very precise CAD-models of targets could be, and have indeed been, created, the simulations at millimeter wave frequencies can not be run with the precision achieved for S- or C-band simulations. An example of an output of a simulation software is given in Fig. 5.1. It presents the RCS of a 6 meters long cylindrical target with four fins and a cone on one end and paraboloid on one end at 1 cm wavelength. The software is BSS [113]. The minimum wavelength allowed by the program is 1 cm, which restricts its use at millimeter wave frequencies.

As was discussed in section 2.1.3, the far-field of physically large targets at millimeter wave band can be even tens of kilometers. Therefore organizing proper field measurements can be challenging. If a proper simulation software tool is not available, and true measurements can not be conducted, a compact antenna test range, such as described in [114], can be used for measuring a down scaled models of the targets. The target is scaled in size to correspond the very high frequency used in test range. The accuracy of this method is governed by the precision with which the target model is made, including the surface material parameters. Also, the quality of the illuminating field is important, particularly its planarity around the test target. An example of an RCS measurement result

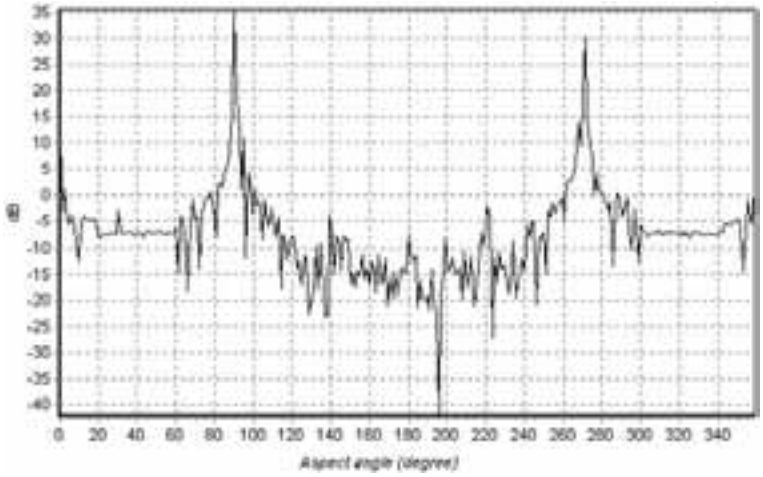

Figure 5.1: *An example of output of a BSS simulation software [113]. It presents the RCS of a 6 meters long cylindrical target with four fins and a cone on one end and paraboloid on the other at 1 cm wavelength.*

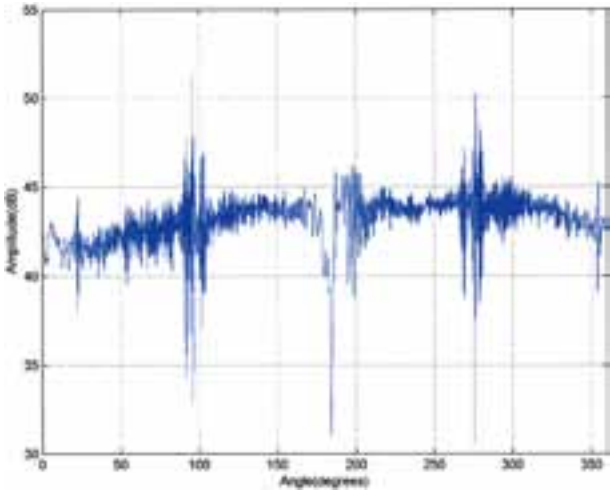

Figure 5.2: *An example of an RCS measurement result obtained using a hologram-based compact antenna test range [114]. The down scaled target is similar to that in Fig. 5.1. The measurement was conducted by Radio Laboratory at Helsinki University of Technology.*

of a similar cylindrical object than in simulation of Fig. 5.1 obtained using a hologram-based compact antenna test range is shown in Fig 5.2. The measurement was conducted by Radio Laboratory at Helsinki University of Technology.

RCS prediction methods at millimeter wave frequencies become even more complicated when the success of RCS reduction techniques is evaluated. There are two main paths for RCS reduction, namely object shaping and use of absorbing materials. Object shaping involves using surfaces that are aligned to minimize reflections into backscattering direction, and avoiding complex structures that cause multiple reflections. Simulating such stealth targets poses the same problems that are encountered in connection to non-stealth targets. The effect of absorbers on the surface of targets, on the other hand, may be virtually impossible to simulate accurately due to the extremely complicated calculations involved. The coating of targets with absorption materials aims to reduce the induced surface currents or match the effective impedance of the outermost layer of targets with that of surrounding air (377Ω) to attenuate the amplitude of scattered fields. Especially at millimeter wave frequencies such absorbing materials that would be suitable for coating of real targets are difficult to manufacture [115]. Therefore down-scaling of coated targets for compact indoor test range measurements is practically not possible. In order to evaluate the RCS of the entire object, true field measurements are the only feasible option.

The requirement of far field condition must not necesserily be met in outdoor test ranges if the purpose is to study the target RCS at true operational distances from the radar. Some targets, like a commercial airliner, reach the far field limit far beyond the maximum detection range of a typical millimeter wave radar. Therefore the problems encountered in connection with simulation softwares and compact test ranges can be overcome by creating an RCS database with a true radar and true targets at authentic operational distances. The portable millimeter wave test radars presented in this thesis are very suitable instruments for carrying out such measurement tasks.

5.2 Examples of observed RCS values

The RCS of a cross-country vehicle (Fig. 5.4) at K_a-band as a function of aspect angle was measured in an outdoor test range. The measurement was carried out on an open field without using an expensive turntable. The vehicle was driven very slowly on a flat surface and it was steered to follow a circle with smallest possible turning radius. The vehicle was continuously tracked with the test radar that was positioned at a distance of one kilometer from the target. The aspect angle of the vehicle was constantly monitored, and 720 samples per revolution were collected. The obtained RCS trace is shown in polar form in Fig. 5.3. The front of the vehicle is towards the 0° aspect angle. The mean RCS calculated over all aspect angles is 7.4 dBm^2, and the specular maxima from the sides of the vehicle have an RCS of 19 dBm^2.

An RCS plot of a jeep at 35 GHz, measured by FGAN research institute using a turntable, is presented in [116]. Although the measured vehicles and the illumination angle are not identical, the overall RCS level in our and FGANs RCS plots is similar. The specular maxima in our measurements are about 6 dB higher than in FGANs results, but the mean value of the jeep seems to be larger than our Land Cruiser's, although the difference is marginal. Their measurements show less variations between minima and maxima than our results. Since the measured targets are not the same, however, reasonable comparisons can not be made. The feasibility of the simple measuring technique shown by this example allows to carry out RCS measurements of real targets in real operational environments. Expensive investments are not needed, and RCS data can be collected from a distance that represents a situation that would be operationally expected.

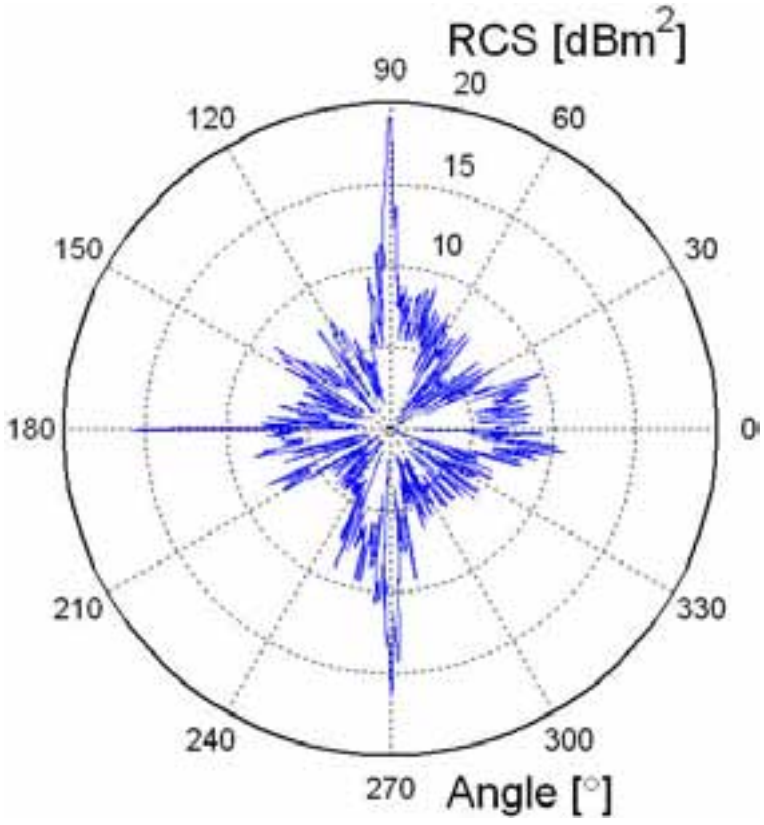

Figure 5.3: *RCS of a Toyota Land Cruiser (see Fig. 5.4) at K_a-band as a function of aspect angle. The measurement was carried out on an open field by continuosly tracking the vehicle that was driven very slowly on a flat surface and steered to follow a circle with smallest possible turning radius. Measuring distance was one kilometer, and radar antenna was at a height of 1.7 meters. The front of the vehicle is towards the 0° aspect angle.*

Figure 5.4: *Photograph of the Toyota Land Cruiser that was used for RCS measurement of Fig. 5.3.*

An example of a situation where the effective RCS of a target can not be simulated reliably is shown in Fig. 5.5, where our RCS measurements of an airplane are presented. The target in question was a Boeing 737-100 commercial airliner, whose far field distance due to the physical dimensions of the plane (length 28.65 m, wing-span 28.35 m) at K_a-band is almost 200 km. The RCS of such a target within a millimeter wave radar coverage (0-20 km) is highly dependent on range due to the complicated and distorted shape of the backscattered wavefronts, since the radar is deep inside the targets near field region. Furthermore, the distance at which the antenna mainlobe beamwidth in meters exceeds the targets largest dimension may be several kilometers. In this case having $\theta_{3dB} = 1°$, the minimum range where the target is completely illuminated by radar main beam is 1640 m. The measurement was conducted for a receding plane, so the observed RCS values are from the tail of the target. As can be seen from Fig. 5.5, the RCS between ranges from 1000 to 2200 meters increases with range, thus producing a nearly constant radar video voltage. Measurement results for distances over 2200 meters are not shown, since the aspect angle of the plane changed after that. The increase of RCS with range was, however, still present in the data, but the increase slope in relation to thermal noise floor was not as steep as between 1000 and 2200 meters.

Measurements of the RCS of a human being at K_a-band are not reported in literature. Our results suggest a mean value of -24.8 dBm^2, which is much lower than the reported values for 9 GHz (-3...+0.8 dBm^2) [13, p. 11.16], 24 GHz (-20...0 dBm^2) [117] and 76 GHz (-8.1 dBm^2) [118]. Our measurement result of a man periodically waving hands show fluctuations caused by this movement in the order of 5 dB, see Fig. 5.6. The moment when the person had hands in upright position show RCS values that fall within a window of 1.5 dB. This interesting measurement shows, that a person will be difficult to detect against ground clutter background when the range increases unless the radar resolution cell is adjusted (see section 3.2). The effect of movement is clearly visible in the results,

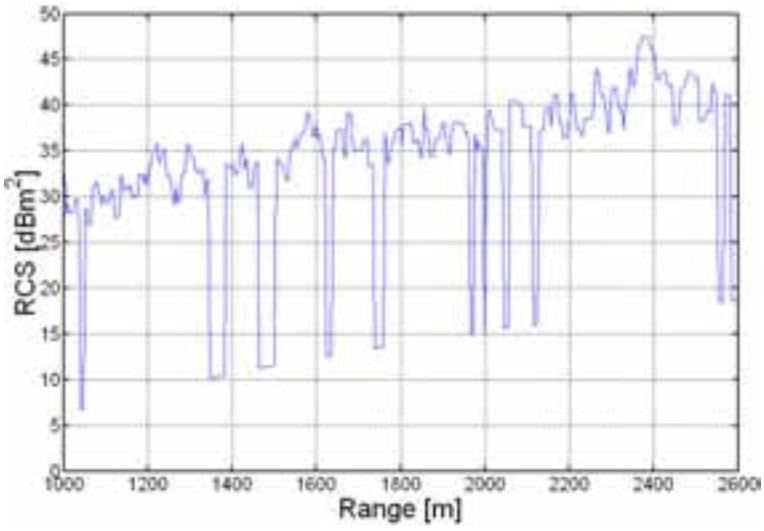

Figure 5.5: *A measurement of Boeing 737-100 commercial airliner showing the RCS behaviour as a function of distance due to operation at near field region. The measurement was conducted using a K_a-band radar.*

which may provide enough information for signal processing to be able to discriminate a moving person from typical clutter background. In stationary situations a person will not be detected from significant distances even with an extremely high-resolution radar due to the low RCS of human being.

The backscattering and attenuation caused by an explosion of a shaped charge at K_a-band was measured. The explosion took place above the ground, and the reflections and attenuation caused by the shock wave ionized front in the direction of the shaped explo-

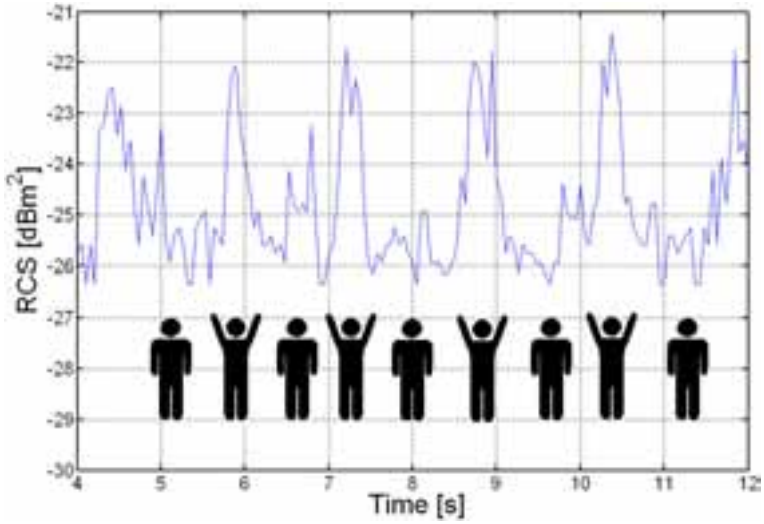

Figure 5.6: *RCS measurement of a human being periodically waving hands. A mean value of -24.8 dBm^2 at K_a-band was measured.*

sion was measured. The explosion volume contained very small amounts of particles of soil and and other solid explosion products, and consisted mainly of rapidly ionized air, a plasma layer. The reflectivity data of the plasma, based on our measurements, as a function of elapsed time after detonation is shown in Fig. 5.7. Unfortunately, at the time of the measurements, our test radar had not yet reached its final assembly stage, so the available dynamic range was limited to little over 20 dB. Therefore some portion of the reflectivity data in Fig. 5.7 is slightly clipped from the top. The measurement range at the test site was fixed, so moving the radar a bit further was not possible. However, due to the fact that the clipping was not severe, the data is still useful.

The volumetric reflection coefficient increases to the level of $\eta = -30$ dB(m^2/m^3) after 150 ms from the moment of explosion, and stays at that level for about 400-450 ms, after which it starts to decay. According to Kulemin [97], the temperature corresponding to the plasma resonance frequency exists for 80-100 ms after the explosion, after which a rapid decrease in refraction index occurs. According to our and Kulemin's measurements, though, the backscattering level remains at high levels for much longer time than 100 ms. Kulemin reports a volumetric reflection coefficient of $\eta = -17$ dB(m^2/m^3) at K_a-band 600 ms after the explosion. Their group had measured an explosion of a non-shaped trotyl charge, and the radar was pointed directly at the center of the explosion.

Simultaneously with the reflectivity measurements, the attenuation caused by explosion was measured. A calibration target was positioned on a radar line of sight so that the explosion volume that was being investigated was directly between the radar and the target. An example of a single measurement event is shown in Fig. 5.8, where the successive backscattering echoes from both, the explosion volume (blue curve) as well as the calibration target (green curve), are averaged over a period of 4 ms. Both curves show

Figure 5.7: *A scattering plot presenting the volumetric backscattering coefficient values of an explosion volume at K_a-band as a function of elapsed time after detonation of a shaped charge.*

Figure 5.8: *An example of an explosion volume backscattering and attenuation measurement at K_a-band. The blue curve is the backscattering from the explosion volume and green curve is the two-way attenuation caused by it. The moment of explosion is at $t = 0.36$ s.*

Figure 5.9: *The two-way attenuation of an explosion volume as a function of the explosion volume backscattering level.*

the relative level compared to a situation before the detonation. The attenuation as a function of the explosion volume backscattering level is shown in Fig. 5.9. The average of the maximum two-way attenuation values, according to our measurements, is 8 dB. The peak attenuation values have been in the order of 13 dB, which corresponds well with Kulemin's [97] findings (12-16 dB).

5.3 Fluctuations of target RCS

Two examples of target RCS fluctuations are presented. Figure 5.10 presents the probability density function and the cumulative probability density function of a stationary cross-county vehicle. The illumination time was 0.4 seconds with a K_a-band radar. The dashed curves represent corresponding Swerling model IV pdf and cumulative pdf. The Swerling model pdf has been scaled for readability, and does not correspond with the y-axis. The cumulative pdf is in scale. As can be seen, the Swerling model fails to describe the behaviour of the RCS distribution of a stationary vehicle, predicting a much wider distribution of target RCS than was measured. This example illustrates the need to create a completely new database of the statistical behaviour of various targets in order to be able to design powerful signal processing methods for a millimeter wave radar.

Another example in Fig. 5.11 shows the measured pdf and cumulative pdf of a Cessna 172 hydroplane. The pdfs are shown relative to the mean RCS level of the plane. The illumination time was 0.33 seconds with a K_a-band radar. Again, the corresponding Swerling

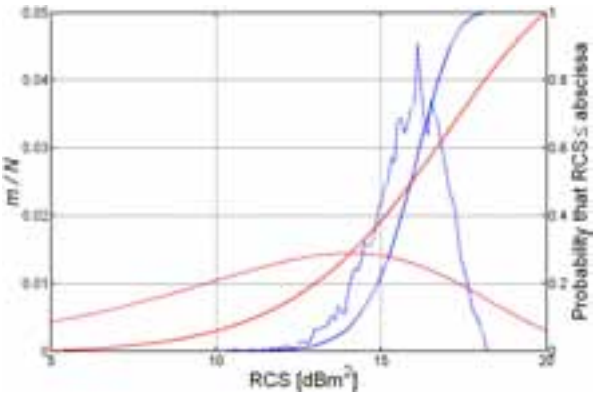

Figure 5.10: *An example of a stationary cross-country vehicle RCS distribution. The blue curves present the measured pdf (dashed) and cumulative pdf (solid). The red lines are the corresponding Swerling IV model pdf and cumulative pdf. The Swerling model cumulative pdf is in scale, but the pdf has been scaled down to enhance the readability of the graph, and does not correspond with the y-axis (left). The y-axis of the cumulative pdf is on the right.*

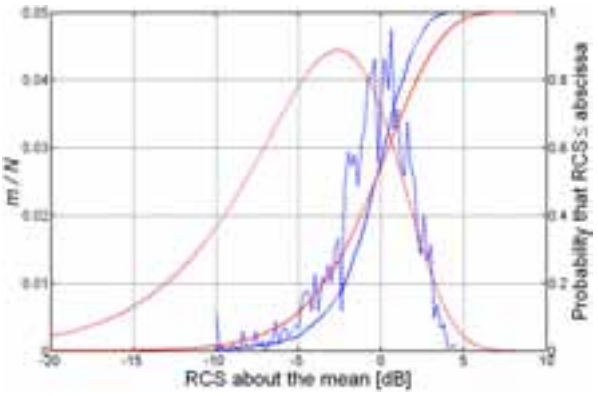

Figure 5.11: *An example of a Cessna 172 hydroplane RCS distribution. The blue curves present the measured pdf (dashed) and cumulative pdf (solid). The dashed lines are the corresponding Swerling IV model pdf and cumulative pdf. The Swerling model cumulative pdf is in scale, but the pdf has been scaled down to enhance the readability of the graph, and does not correspond with the y-axis (left). The y-axis of the cumulative pdf is on the right.*

IV model pdf and cumulative pdf are shown with dashed curves, with the Swerling model pdf being scaled for readability. The cumulative pdf is in scale. In this case the Swerling model fits the measured distribution better than in case of a stationary vehicle, but still predicts wider distribution than was observed.

5.4 Effective RCS and multipath propagation

K_a-band radar wave propagation was studied in a long road canyon where the measurement path is up to several kilometres long, completely straight and bordered on both sides by tall, dense forest vegetation immediately at its left and right edges (see Fig. 1 in [P11]). Our target was a regular station wagon car (Fig.2 in[P11]). The aim of the measurement was to verify the "lens effect" discussed in [81, pp. 61-65] and to examine the effect of multipath propagation on target RCS. The lens factor r_L is defined as follows:

$$r_L = \frac{1}{\sqrt{1 + \frac{2R_{r1}R_{r2}}{(R_{r1}+R_{r2})R_L \sin\phi}}}, \tag{5.1}$$

where R_{r1} and R_{r2} are the range from the radar to the ground reflection point and the range from ground reflection point to target, respectively. The radius of the local curvature of the ground is R_L, which is positive value for convex ground and negative for concave one. Before the start of our measurements at the long road site, the road shape relative to radar location was measured using a theodolite. The result of the road shape measurement is shown in Fig. 5.13 (green curve). The shape of the road was used to determine the local radii of curvature corresponding to the different target ranges. The method is illustrated in Fig. 5.12. First the slope factors of straight lines (AB and BC) between the specific point under consideration (B) and its adjacent points (A,C) were determined. After that two straight lines AB´ and BC´ perpendicular to the lines AB and BC were set to intersect the lines AB and BC in the middle. The intersection point of AB´ and BC´ marked the center of the local curvature, from which the radius R_L was calculated. The points with convex curvature always cause dispersion of the radar wave thus decreasing the multipath effect. The concave portions, on the other hand, have

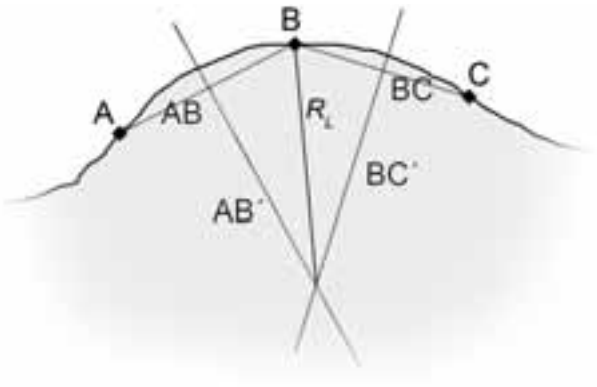

Figure 5.12: *Illustration of the method for estimating a local radius of curvature.*

an effect of focusing the radar signal. A Matlab-routine of the described method was implemeted.

At certain ranges the target was partially or even completely masked by the bulges of the road. This shadowing effect was taken into consideration by calculating the relative portion of the vehicle area that was visible from the radar site at different ranges. The predicted target echo return as a function of range is shown in Fig. 5.13. The dashed blue curve shows the target echo power predicted by a basic form of the radar equation (Eq. 2.4). The power level is normalized to correspond with the saturation level of our test radar. The solid blue curve represents the expected target echo, when the shadowing effect, lens factor (Eq. 5.1) and multipath propagation factor (Eq. 2.14) have been taken into account.

The measurement results are shown in Fig. 5.14. The black curves are the radar equation (dashed), and the radar equation with shadowing, lens factor and multipath propagation factor taken into account (solid). The coloured curves show the target echo power from three independent measurements. As can be seen, the measured results are very close to the values predicted by theory. A radar equation alone, or the radar equation with multipath propagation factor included, can not explain the seemingly anomalous behaviour of target echo. The lens factor must be included in order to obtain more accurate predictions of target echo amplitude at certain topographical environment. In [81] the lens factor theory was verified at significantly shorter ranges (less than 50m). Our results show the functionality of the "lens effect"-theory also in connection to longer radar ranges and multiple successive concave or convex portions.

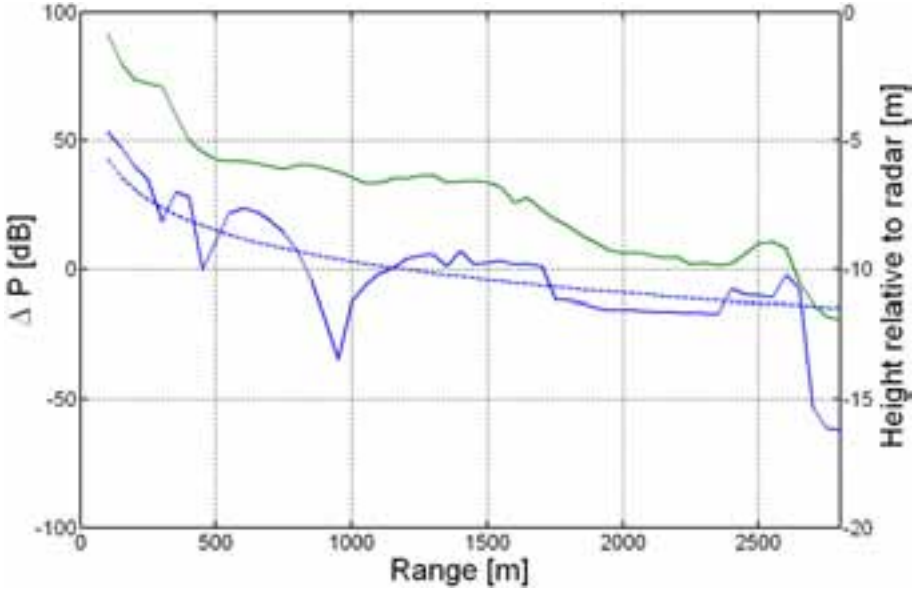

Figure 5.13: *The road profile of the long road canyon is shown with the green curve. The dashed blue curve shows the target echo power predicted by a basic form of the radar equation, and the solid blue curve represents the expected target echo when the shadowing effect, lens factor and multipath propagation factor have been taken into account.*

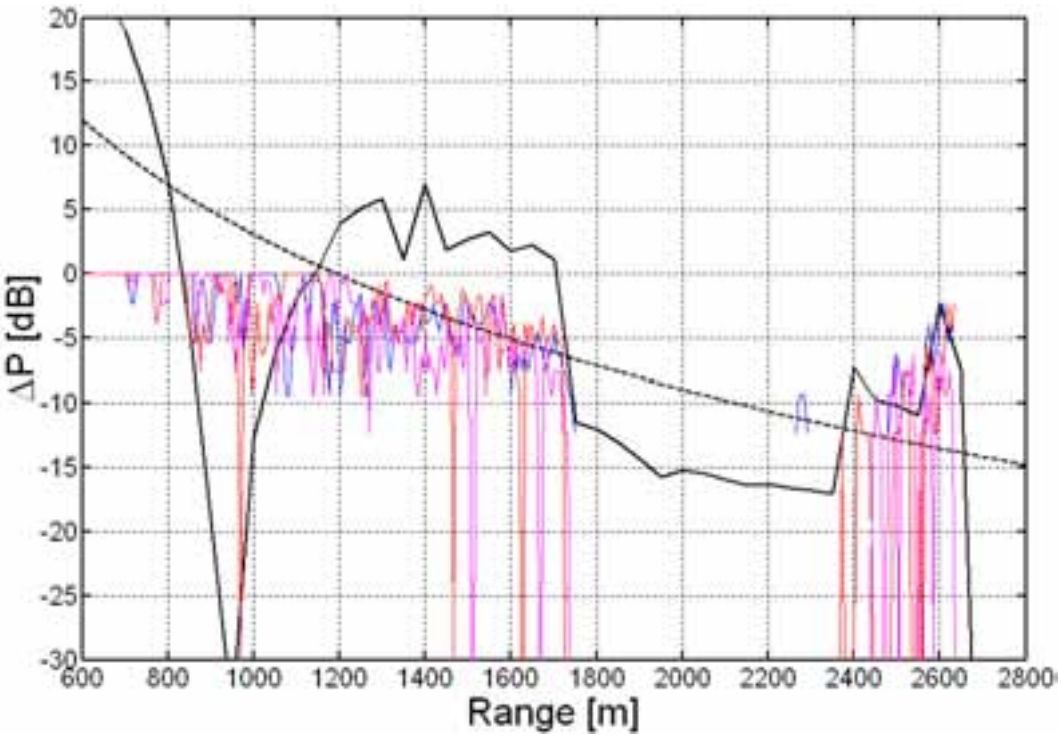

Figure 5.14: *Three independent measurements showing the target echo power, relative to the receiver saturation level, at a long road canyon. The black curves are the radar equation (dashed), and the radar equation with shadowing, lens factor and multipath propagation factor taken into account (solid).*

There are, however, differencies between theory and practical measurements results. Especially at ranges between 1200-1700 m the measured target echo is 5-7 dB lower than what is predicted by theory. Also between ranges 1750-2350 m the theoretical value for received power level is about -15 dB below radar saturation level, but in the field measurements the target at these ranges was completely lost. These differencies can be related to complicated propagation phenomena, which would require more extensive measurement results to be solved. Furthermore, the road profile was measured using 50 m steps in range, which in its part may cause minor inaccuracies in determination of local radii of curvature. The shadowing effect was taken into account assuming that the target RCS is a function of square of the visible physical area. This assumption may most likely be wrong, but due to the aforementioned difficulties involved with using RCS simulation softwares at millimeter wave frequencies (see 5.1), the major contributors of the test vehicles RCS are not known. Therefore a linear dependency was used in calculations.

The effect of multipath propagation does not only concern target RCS fluctuations. A major difficulty is related to the estimation of the elevation angle of a target. In the illumination geometry of a ground based radar, as was discussed in section 2.1.2, the reflected component is practically always present. Depending on the radar antenna height, target height and target range, the strongest echo may occur at an elevation angle somewhere between the real target and the image of the target below the horizon. This causes se-

vere troubles especially for automatic tracking systems, which constantly align the radar antenna towards a too low elevation angle when tracking ground based or low flying targets. An illustration of the alignment error is depicted in Figures 5.15 and 5.16, where photographs taken through the carefully collimated optical sight of our radar show the actual direction of the radar antenna main beam in a situation where the target echo is at maximum level. The elevation angle in both cases is lower than what the actual target elevation angle is.

Figure 5.15: *An illustration of the elevation angle alignment error of a radar caused by multipath propagation as seen through the optical viewfinder of our radar.*

Figure 5.16: *An illustration of the elevation angle alignment error of a radar caused by multipath propagation as seen through the optical viewfinder of our radar.*

6 Notes on processing algorithms to millimeter wave radars

Clutter statistics presented in Chapter 4 combined with target RCS characteristics presented in Chapter 5 provide tools for the design of radar signal processing algorithms. As was discussed in section 2.3, the statistical features of clutter and targets in amplitude and frequency domain govern the fine-tuning process of signal processing methods in strive for maximization of target detection probability while constraining the number of false alarm on an acceptable level. An effective work on this challenging field of radar technology is enabled by thorough field measurements of clutter and target backscattering as well as radar wave propagation in various operational situations. In this chapter additional notes concerning certain issues that have to be taken into account in the development of signal processing methods are discussed.

6.1 Effects of mobile platforms

In Doppler processing techniques the spreading of target and clutter echoes in frequency domain due to system phase noise and oscillator instabilities results in power leakage to the adjacent Doppler bins. This may deteriorate the theoretical velocity resolution obtainable by the given combination of illumination time and pulse repetition frequency. In addition to the degradation of velocity resolution, the phase noise sidebands may completely prevent target detection, e.g. in case when a slowly moving target is buried under ground clutter sidebands. A mobile platform causes further degradation of the radar oscillator performance, which can not be reliably modeled only with computer simulations. Dynamic simulation tools for moving vehicles are available, but in order to study the oscillator performance in the true operating conditions of the moving platform, extensive and well-prepared experimenting out in the field is required. Mobile radar systems face the challenge of shocks and vibration caused by their operating environment, e.g. rough terrain (see Fig. 1 in [P10]), which may severely degrade the performance of frequency-generating device. During the thesis work, a practical test arrangement for mobile radar oscillator stability measurements in real operational environment was outlined and assembled [P10].

Interesting phenomena related to the shapes of the frequency probability density functions of the oscillator under test were observed in our field measurements. Our test cases involved four different modes of operation of the platform. In two of the cases the vehicle was not moving, but had engine turned off in one and running in the other case. In the two remaining cases the vehicle was moving very slowly (less than 20 km/h) and with a speed of 50 km/h. Examples of the results are shown in Fig. 3 of [P10]. Our observation was that the oscillator performance was poorest at driving speed of 50 km/h and in situation

where the engine was idling. The idle motion vibrations have indeed stronger effect on the oscillator than a slow driving speed, which is clearly seen when comparing graphs (c) and (d) with graph (e) of Fig. 3 in [P10]. These measurement results depict the oscillator behaviour during a time period of 30 seconds. Measurements of oscillator stability over longer time periods were not conducted, since typical radar processors seldom utilize more than 1-5 seconds of radar data. The frequency stability of a mobile millimeter wave radar could be enhanced by the use of vibration absorbers and/or high quality crystal oscillators. In any case, the system phase noise performance in different modes of operation of the radar platform have to be considered when defining the performance requirements of a radar system. The effectiveness of even highly sophisticated signal processing methods is partially dictated by the quality of oscillators of the radar system.

6.2 Stationary and moving target detection

As was discussed in section 2.3, the traditional method for discriminating moving targets from stationary man-made objects or ground clutter is the use of an MTI-filter. This approach is not suitable for a high PRF millimeter wave radar, since e.g. an unmodified three-pulse MTI canceller [13, Ch. 15] attenuates 30 percent of the unambiguous Doppler frequencies of the received signal at least or more than 10 dB, see Fig. 2.17. As an example, let us consider a K_a-band radar utilizing a pulse repetition frequency of 20 kHz, which has its unambiguous Doppler velocities between 0 and 43 m/s. A three pulse MTI-filter would reduce the signal level of targets having velocities less than 13 m/s at least 10 dB, which is not acceptable. Therefore a Doppler filter bank, a real-time implementation of FFT or equivalent methods that do not lose data must be considered.

Even though the unambiguous velocity range of a K_a-band radar having PRF of 20 kHz is quite enough for ground based targets, much higher radial velocities are currently met in air surveillance systems. The unambiguous velocity range can be extended without sacrificing unambiguous range measurement ability by changing the transmitter frequency from pulse to pulse or alternatively staggering the pulse repetition intervals [32]. These methods provide an unevenly sampled data set, from which the true radial velocity can be extracted even though the average sampling rate would be below Nyqvist criterion [119]. A drawback of uneven sampling is the difficulty in estimation of power spectral density, which is extremely challenging to implement into real-time systems. Instead, only a single frequency component that best fits to the interpulse phase shifts and time lags is estimated. The obtained frequency represents the average velocity of the given radar cell and depends on the signal-to-noise ratios of the individual Doppler velocity components in that radar cell. Thus the method can not discriminate different velocity components within the unevenly sampled data set, but the average velocity component of a radar resolution cell containig target and clutter can differ enough from surrounding cells occupied by clutter alone to allow the radar to distinguish a target from clutter background.

In case of stationary targets, the amplitude and frequency information of the radar echoes in most cases are insufficient for detection. The amplitude of a target may be in the order of or even less than that of surrounding clutter, and Doppler frequencies of ground clutter and a stationary target overlap in the spectrum. Image processing techniques can

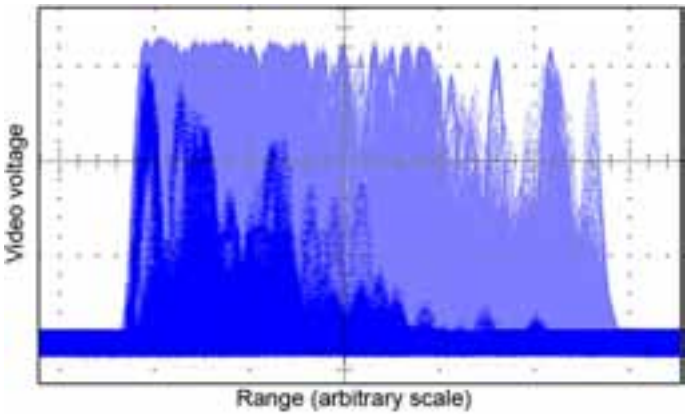

Figure 6.1: *An example of radar echo of an approaching cross-country vehicle measured with horizontal (background, light-blue) and vertical (front) polarizations at K_a-band.*

be used, but only in connection with high-resolution radars, in which the target extends into several resolution cells. Radar polarimetry can be used to improve the probability of detection and to reduce the false alarm rate. For distinguishing a target in background clutter, the polarimetric features of both the target and clutter must be characterized and employed in target detection. The polarimetric characteristics are often structure dependent. For example, the existence of strong cross-polarized component in the radar backscatter usually provides a unique target signature. A polarimetric radar transmits coherently with two orthogonal polarizations, e.g. linear horizontal and linear vertical, and receives the backscattered echoes on the same two polarizations. This results in four received channels where both the amplitude and relative phase are measured. The measured signals in these four channels represent all the information needed to measure the polarimetric scattering properties of the target. In order to be able to characterize different target and clutter types, polarimetric measurements are needed. An example of radar echo of an approaching cross-country vehicle measured with horizontal and vertical polarizations at K_a-band is shown in Figure 6.1. If a complex 2 x 2 polarimetric matrix is to be obtained, the cost and size of a radar system is increased as four separate receivers are needed. If the use of a single antenna is required, also the antenna feed arrangement becomes more complicated and may result in increased loss of aperture illumination efficiency. Additionally, according to our preliminary experiments, the different polarimetric scattering matrix components in practical situations may be differ more than 15 dB, which may prevent the radar from obtaining some of the polarization signatures of weak target echoes.

Due to the high data output rate of our test radars, basic data compression algorithms were tested in order to reduce the amount of data to be captured for later analysis. Comparison between the two methods showed, that a conventional *"N-out-of-M"* -approach did not provide the desired levels of P_d and P_{fa} [P3]. The data compression method that worked more reliably, and had the advantage of preserving the average value of the compressed echoes, used an approach where the radar echo was accepted if the average of eight consecutive pulses exceeded the preset threshold value. This method provided good data compression ratios while preserving the targets of interest. Data compression was needed in connection with experiments involving operational aspects of radar use rather than in specific clutter or target measurements.

7 Summary of publications

In paper [P1] the design outlines due to our field test arrangements are discussed and our portable monostatic and bistatic millimeter wave test instrumentation radars are presented. A phenomenon related to the increse of visually clear sky backscattering level in connection to meteorological inversion layers at extremely cold conditions (below -30°C) is presented. The heavy meteorological inversion layer, illustrated by the humidity and temperature profiles, changes the characteristics of the two-way propagation path and the resulting increase in equivalent RCS of noise level is in the order of 10 dB. The so called angel-echoes are a known phenomenon at traditional radar frequencies (1-10 GHz), arising from areas having strong refraction index gradients, but previous reports of the phenomenon at millimeter wave frequencies are not known.

Paper [P2] describes our K_a- and V-band instrumentation radars in more detail. Results of our clear sky backscattering measurements are presented, in which variations up to 5 dB around mean value were observed. Preliminary measurement results concerning the lens-effect theory discussed in [81] showed, that the theory is valid also for relatively rough terrain environment.

In paper [P3] our two basic data compression algorithms were tested with real millimeter wave radar data. Data compression algorithms were required to reduce the amount of data to be captured for later analysis in connection with experiments involving operational aspects of radar use rather than in specific clutter or target measurements. Comparison between the two methods showed, that a conventional *"N-out-of-M"* -approach did not provide the desired levels of P_d and P_{fa}. The data compression method using an approach where the radar echo was accepted if the average of eight consecutive pulses exceeded the preset threshold value was shown to produce good data compression ratios while preserving the targets of interest.

A novel radar pulse width optimization method is presented in paper [P4]. Very narrow bandwidths will generally give low noise levels, whereas the observed clutter amplitude increases if we employ longer pulses thereby effectively increasing the "noise" floor in the radar receiver thereby degrading the minimum detectable RCS. The limits that clutter returns and thermal noise alone set on the maximum range of detection for a specific target RCS can be calculated for different radar pulse widths. We show in paper [P4] and in section 3.2 of this thesis, that these maximum range curves converge to produce a solution for the optimal pulse width for a radar configuration in given clutter conditions.

In paper [P5] the tactical requirements as well as operational and environmental constraints related to the upgrading of armored vehicle sensor systems are discussed. Vertical acceleration values of a vehicle chassis due to driving in rough terrain and using the main weapon are presented.

In paper [P6] an oscillator prototype for a millimeter wave radar is presented. We present a theoretical discussion of the oscillator phase noise implications to radar signal processing. Preliminary measurements conducted onboard a moving vehicle showed the applicability of the oscillator prototype as a primary frequency generating device of a moving millimeter wave radar system.

Paper [P7] describes our simple rectangular plate millimeter wave radar calibration target constructed for absolute calibration of our test radars. With a precise mechanical alignment mechanisms and an optical sight the measured V-band calibration uncertainty was found to be less than 0.5 dB and pointing resolution better than 0.05 degrees. Additional absorber collars provide an easy way of adjusting the actual RCS and effectively reduce edge diffraction effects.

In paper [P8] the synchronization possibilities of a bi- or multistatic radar are discussed, and the use of an HF radio link is proposed as a solution. A ranging error analysis as a function of synchronization error is given.

In paper [P9] completely new V-band clutter backscattering measurements and new results obtained at K_a-band are presented. The illumination geometries, extremely low grazing angles ($< 5^\circ$) and perpendicular incidence, were selected to correspond with typical situations encountered using a ground-based radar. The measured clutter sources included different terrain types, typical Scandinavian forests and trees, and wet- and refrozen snow covered ground.

In paper [P10] an outline of a practical test arrangement for mobile radar oscillator stability measurements in real operational environment as well as results of our field test measurements are presented. The measured frequency probability density functions of the oscillator under test in four different modes of operation of the radar platform showed, that oscillator performance is poorest at high driving speeds (50 km/h) in rough terrain and when the vehicle motor is idling. The author is not aware of previous reports of such phenomenon.

In paper [P11] the K_a-band radar wave propagation was studied in a long road canyon where the measurement path is up to several kilometres long, completely straight and bordered on both sides by tall, dense forest vegetation. The importance of including shadowing effects caused by road profile, multipath propagation factor and the lens factor due to successive concave and convex portions of the road, into radar range prediction calculations were demonstrated by our measurement results. The validity of the lens-effect theory [81] was verified in long radar ranges.

8 Discussion and conclusions

The purpose of the work described in this thesis was to create tools for radar performance estimation in true operational environments and to demonstrate the feasibility of millimeter wave band for radar applications. Radar wave propagation and backscattering was studied in different environments using real radar data obtained from field measurement campaigns, carried out using the test instrumentation radars constructed within our research group.

In Chapter 2 theoretical background concerning the use of a ground based millimeter wave radar system is outlined. Emphasis is on multipath propagation, which essentially always effects the performance of a ground based radar regardless of the target location (on ground or airborne). Furthermore, due to the short wavelengths (< 1 cm) of millimeter wave band, the definition of far field criterion has to be based on target dimensions rather than the radar antenna diameter. This fact can not be overlooked, as was shown in Fig. 5.5 and related discussion, although apparently in the work presented in [81] it has been incorrectly neglected.

In Chapter 3 the V-band test instrumentation radar used for conducting measurements during the thesis work is presented, and the test radar for K_a-band is presented in [P2]. A novel pulse width optimization technique is presented in section 3.2 together with discussion of the radar antenna beamwidth definition. The radar resolution cell is defined by antenna beamwidth and main lobe shape and by radar pulse width and shape. When measuring the backscattering coefficient of clutter, the nonuniform illumination by an antenna main beam can be accounted for using a beam shape correction factor, which in case of a Gaussian antenna main beam shape was shown to be equal to using 1 dB points for determining the radar antenna beamwidth. Furthermore, it was shown, that an optimal radar pulse width can be found for different combinations of target RCS and background clutter reflectivity. Since the thermal noise floor is governed by the noise bandwidth of the receiver and the effective clutter backscattering level is governed by clutter reflectivity and instantaneously illuminated clutter cell area, the pulse width selection is an essential factor in radar range maximization. In the latter part of Chapter 3, calibration issues are discussed and the specific calibration methods used for calibrating our test radars are described.

In chapter 4 an overview of our data acquisition methods used in capturing and storing radar data is given. Measurement results of radar clutter in typical illumination geometries encountered using a ground-based radar are presented for K_a- and V-band. Our low grazing angle clutter backscattering measurements as well as measurements at perpendicular incidence are completely new, and therefore comparisons with previous measurement results of others are not possible. Comparison of our measurement results with ground clutter models presented in [67] and [97] show distinct differencies, thereby necessitating

dedicated measurement campaigns in order to be able to reliably estimate radar performance in true operational environments. Our measurements of vegetation spectrum show, that the spectral dependency values suggested by Currie [67] and our measurements seem to differ quite considerably in the behaviour of high frequency components. New spectral dependency values are proposed, and the summary can be found in Table 4.3. A previously unknown phenomenon related to clear sky backscattering in connection to heavy meteorological inversion layers is presented. Furthermore, in Chapter 4 new volumetric backscattering coefficients of rain and snow at K_a-band are given. The results for rain suggested by our measurements correlate well with previous work presented in literature. Our measurement results of snow backscattering are completely new.

Examples of target RCS values are given in Chapter 5, and measurements of the effects of radar propagation at millimeter wave frequencies are presented. The "lens effect"-theory discussed in [81] was shown by our measurements to be valid also at longer radar ranges than was presented in [81] and in connection with multiple successive concave or convex portions of terrain profile. Also, completely new radar signal attenuation and backscattering measurement results from explosions of shaped charges are presented. The results showing volumetric bakscattering coefficient and attenuation of the plasma in explosion volume after the detonation are summarized in Figures 5.7 and 5.9.

Future work involves improving the field portable data acquisition equipment in order to be able to measure temporal characteristics of clutter and targets. The importance of polarimetry is addressed in several sources of radar signal processing literature, and this aspect of clutter and target measurements will be included in the future work. Methods enabling a direct assimilation of rain backscattering data with observed rain intensities will be improved. Furthermore, the clutter database will be further enlarged to cover also sea clutter backscattering in different wind conditions.

The clutter and target measurement results described in this thesis enable effective work in design and testing of millimeter wave radar signal processing algorithms. Using the real radar data, developing of algorithms can be done in software-environment, and preliminary tests can be conducted without any hardware implementation. If the amount of available radar data is large, algorithms can be extensively tested for data captured in completely different circumstances and with varying clutter backgrounds and target scenarios. The performance of processing algorithms achieved using real radar data in development stage is more effective than in case only simulated data is used.

As the final conclusion of this thesis, the following was achieved:

1) The feasibility of a compact millimeter wave radar has been demonstrated in true environmental conditions and several hardware solutions have been evaluated in conjunction with practical field measurements.

2) Results of completely new backscattering measurements of soil, vegetation and snow covered ground at V-band are presented.

3) New results of K_a-band backscattering measurements of soil, vegetation and snow at extremely small and large grazing angles are presented.

4) New rain and snowfall backscattering measurement results are presented at K_a-band. Completely new radar signal attenuation and backscattering measurement results from explosions of shaped charges are presented.

5) Measurement results showing an unknown phenomenon of variations in clear-sky backscattering of millimeter wave radar signal in correlation with the existence of a low level inversion layer in the atmosphere are presented.

6) A novel and easy-to-use approach for radar pulse width optimization has been introduced.

7) Results of measurements aimed to verify a special radar signal propagation phenomenon called "lens-effect" are presented and discussed. The suggested theory is shown to be valid also at long radar ranges and in connection with multiple successive concave or convex portions of terrain profile.

Bibliography

[1] M. Skolnik, *Introduction to Radar Systems*, McGraw-Hill, Singapore, 1981.

[2] L. Brown, *A Radar History of World War II - Technical and Military Imperatives*, Institute of Physics Publishing, London, UK, 1999.

[3] F. Losee, *RF Systems, Components and Circuits Handbook*, Artech House, Norwood, USA, 1997.

[4] T. Teshirogi and T. Yoneyama (eds.), *Modern Millimeter Wave Technologies*, IOS Press, Tokio, Japan, 1999.

[5] P. Ingwersen and W. Lemnios, "Radars for Ballistic Missile Defense Research", *Lincoln Laboratory Journal*, Vol. 12, No. 2, 2000, pp. 245-266.

[6] W. Camp, J. Mayhan and R. O'Donnell, "Wideband Radar for Ballistic Missile Defense and Range-Doppler Imaging of Satellites", *Lincoln Laboratory Journal*, Vol. 12, No. 2, 2000, pp. 267-280.

[7] Longbow FCR and Missile Fact Sheet, http://www.missileandfirecontrol.com/our_news/factsheets/factsheet-LONGBOW.pdf, Lockheed Martin Corporation, 2003.

[8] M. Streetly (ed.), *Jane's Radar and Electronic Warfare Systems, 11^{th} edition (1999-2000)*, DPA, London, UK, 2000.

[9] B. Rivers (ed.), "Americas Report: New Self-Protection System for Ground Vehicles Demonstrated", *The Journal of Electronic Defense* , Vol. 26, No. 9, September 2003, p. 18.

[10] F. Bremer and P. van Genderen (eds.), *Radar Development in the Netherlands*, Thales Nederland, Netherlands, 2004.

[11] C. Foss, "Chrysanthemum comes to light", *Jane's Intelligence Review*, September 1, 1996, p. 402.

[12] H. Ivanov, "Russian anti-tank system set for fielding", *Jane's Defence Weekly*, Vol. 39, No. 7, February 2003, p. 11.

[13] M. Skolnik (ed.), *Radar Handbook, 2^{nd} edition*, McGraw-Hill, New York, USA, 1990.

[14] M. Moruzzis, P. Saulais, T. Tat and T. Huei, "Automatic Target Classification for Naval Radar", *Proceedings of the IEE International Radar Conference 2004*, Toulouse, France, Oct. 2004, 5 p.

[15] C. Balanis, *Antenna Theory, 2^{nd} edition*, John Wiley & Sons, New York, USA, 1997.

[16] S. Drabowitch, A. Papiernik, H. Griffiths, J. Encinas and B. Smith, *Modern Antennas*, Chapman & Hall, Cambridge, UK, 1998.

[17] P. Bhartia and I. Bahl, *Millimeter Wave Engineering and Applications*, John Wiley & Sons, New York, USA, 1984.

[18] F. Nathason, *Radar Design Principles, 2^{nd} edition*, McGraw-Hill, New York, USA, 1991.

[19] M. Golio (ed.), *The RF and Microwave Handbook*, CRC Press, Boca Raton, USA, 2001.

[20] D. Barton, C. Cook and P. Hamilton (eds.), *Radar Evaluation Handbook*, Artech House, Norwood, USA, 1991.

[21] J. Doble, *Introduction to Radio Propagation for Fixed and Mobile Communications*, Artech House, Norwood, USA, 1996.

[22] ITU-R: "Recommendation ITU-R P.676-5 Attenuation by atmospheric gases", *ITU-R Recommendation 1995 P Series*, 1996.

[23] H. Liebe, P. Rosenkranz and G. Hufford, "Atmospheric 60-GHz Oxygen Spectrum: New Laboratory Measurements and Line Parameters", *Journal of Quantitative Spectroscopy and Radiative Transfer*, Vol. 48, No. 5-6, Nov.-Dec. 1992, pp. 629-43.

[24] J. van Vleck and V. Weisskopf, "On the Shape of Collision-Broadened Lines", *Reviews of Modern Physics*, Vol. 17, No. 2-3, 1945, pp. 227-36.

[25] R. Olsen, D. Rogers and D. Hodge, "The aR^b relation in the calculation of rain attenuation", *IEEE Transactions on Antennas and Propagation*, Vol. 26, No. 2, February 1978, pp. 318-329.

[26] D. Barton, *Radar System Analysis and Modeling*, Artech House, Norwood, USA, 2005.

[27] J. Jackson, *Classical Electrodynamics*, John Wiley & Sons, New York, USA, 1999.

[28] R. Sullivan, *Microwave Radar: Imaging and Advanced Concepts*, Artech House, Norwood, USA, 2000.

[29] B. Matkin, J. Mullins and T. Ferster, "Bistatic Reflectivity Measurements at X, Ku, Ka and W-Band Frequencies", *Proceedings of 2001 IEEE Radar Conference*, Atlanta, USA, May 2001, pp. 404-409.

[30] E. Li and K. Sarabandi, "Low grazing incidence millimeter-wave scattering models and measurements for various road surfaces", *IEEE Transactions on Antennas and Propagation*, Vol. 47, No. 5, May 1999, pp. 851-861.

[31] B. Mahafza, *Radar Systems Analysis and Design using Matlab*, Chapman & Hall/CRC, Boca Raton, USA, 2000.

[32] P. Lacomme, J-P. Hardange, J-C. Marchais and E. Normant, *Air and Spaceborne Radar Systems: An Introduction*, SciTech Publishing, Norwich, USA, 2001.

[33] B. Welsh and J. Link, "Accuracy criteria for radar cross section measurements of targets consisting of multiple independent scatterers", *IEEE Transactions on Antennas and Propagation*, Vol. 36, No. 11, November 1988, pp. 1587-1593.

[34] L. Hendrick, "Analytical investigation of near zone/far zone criteria", *Proceedings of Radar Reflectivity Measurement Symposium*, Springfield, USA, July 1964, pp. 5-19.

[35] P. Beasley, A. Stove, B. Reits and B. As, "Solving the problems of a single antenna frequency modulated CW radar", *Proceedings of 1990 IEEE International Radar Conference*, Arlington, USA, May 1990, pp. 391-395.

[36] J. Kim, S. Ko, S. Jeon, J. Park and S. Hong, "Balanced topology to cancel Tx leakage in CW radar", *IEEE Microwave and Wireless Components Letters*, Vol. 14, No. 9, September 2004, pp. 443-445.

[37] I. Komarov and S. Smolskiy, *Fundamentals of Short-Range FM Radar*, Artech House, Norwood, USA, 2003.

[38] S. Piper, "Frequency-Modulated Continuous Wave Systems", Chapter 12 in: J. Scheer and J. Kurtz (ed.), *Coherent Radar Performance Estimation*, Artech House, Norwood, USA, 1993.

[39] S. Piper, "FMCW range resolution for MMW seeker applications", *Proceedings of 1990 IEEE Southeastcon*, New Orleans, USA, April 1990, pp. 156-160.

[40] H. Röhling, M.-M. Meinecke, "Waveform design principles for automotive radar systems", *Proceedings of 2001 CIE International Conference on Radar*, Beijing, China, October 2001, pp. 1-4.

[41] S. Hovanessian, N. Marechal and L. Ostroy, "Doppler analysis of low PRF radars", *Proceedings of 1996 IEEE Aerospace Applications Conference*, Aspen, Colorado, February 1996, pp. 129-138.

[42] J. Marcum, "A statistical theory of target detection by pulsed radar", *IEEE Transactions on Information Theory*, Vol. 6, No. 2, April 1960, pp. 59-267.

[43] A. Ferrari, C. Berenguer and G. Alengrin, "Doppler ambiguity resolution using multiple PRF", *IEEE Transactions on Aerospace and Electronic Systems*, Vol. 33, No. 3, July 1997, pp. 738-751.

[44] J. Misiurewicz, "Unambiguous Doppler frequency estimation in MTI radar", *Proceedings of Radar97*, Edinburgh, UK, October 1997, pp. 530-534.

[45] K. Hondl and M. Eilts, "Evaluation of Doppler Velocity Dealiasing Techniques for Low-Nyquist Velocity Data", *Proceedings of 26th Conference on Radar Meteorology (American Meteorological Society)*, Norman, USA, May 1993, pp. 59-61.

[46] P. Prinsen, "Elimination of Blind Velocities of MTI Radar by Modulating the Interpulse Period", *IEEE Transactions on Aerospace and Electronic Systems*, Vol. 9, No. 5, September 1973, pp. 714-724.

[47] D. Schleher, *MTI and Pulsed Doppler Radar*, Artech House, Norwood, USA, 1991.

[48] A. Boehmer, "Binary pulse compression codes", *IEEE Transactions on Information Theory*, Vol. 13, No. 2, April 1967, pp. 156-167.

[49] E. Fowle, "The design of FM pulse compression signals", *IEEE Transactions on Information Theory*, Vol. 10, No. 1, January 1964, pp. 61-67.

[50] H. Deng, "Effective CLEAN algorithms for performance-enhanced detection of binary coding radar signals", *IEEE Transactions on Signal Processing*, Vol. 52, No. 1, January 2004, pp. 72-78.

[51] N. Willis, *Bistatic Radar*, Artech House, Norwood, USA, 1991.

[52] M. Jackson, "The Geometry of Bistatic Radar Systems", *IEE Proceedings*, Vol. 133, Part F, No. 7, December 1986, pp. 604-612.

[53] C. Bovey and C. Horne, "Synchronization aspects for bistatic radars", *Proceedings of IEE International Conference on Radar 1987*, London, UK, October 1987, pp. 22-25.

[54] L. Kesheng, "An analysis of some problems of bistatic and multistatic radars", *Proceedings of the International Radar Conference 2003*, Adelaide, Australia, September 2003, pp. 429-432.

[55] R. Larson, A. Maffett, R. Heimiller, A. Fromm, E. Johansen, R. Rawson and F. Smith, "Bistatic Clutter Measurements", *IEEE Transactions on Antennas and Propagation*, Vol. 26, No. 6, November 1978, pp. 801-804.

[56] L. Osadciw and J. Slocum, "Clutter Processing Using K-Distributions for Digital Radars with Increased Sensitivity", *Proceedings of IEEE Radar Conference 2002*, Long Beach, USA, April 2002, pp. 237-242.

[57] D. Meyer and H. Mayer, *Radar Target Detection*, Academic Press, New York, USA, 1973.

[58] J. Echard, "Estimation of Radar Detection and False Alarm Probability", *IEEE Transactions on Aerospace and Electronic Systems*, Vol. 27, No. 2, March 1991, pp. 255-260.

[59] D. Shnidman, "Radar Detection Probabilities and their Calculation", *IEEE Transactions on Aerospace and Electronic Systems*, Vol. 31, No. 3, July 1995, pp. 928-950.

[60] D. Drumheller and H. Lew, "Pade approximations to Rician statistical functions", *IEEE Transactions on Aerospace and Electronic Systems*, Vol. 35, No. 4, October 1999, pp. 1421-1428.

[61] G. Corazza and G. Ferrari, "New Bounds for the Marcum Q-Function", *IEEE Transactions on Information Theory*, Vol. 48, No. 11, November 2002, pp. 3003-3008.

[62] S. Parl, "A new method of calculating the generalized Q-function", *IEEE Transactions on Information Theory*, Vol. 26, No. 1, January 1980, pp. 121-124.

[63] L. Scharf, *Statistical Signal Processing: Detection, Estimation and Time Series Analysis*, Addison Wesley, New York, USA, 1991.

[64] J. DiFranco and W. Rubin, *Radar Detection*, Artech House, Dedham, USA, 1980.

[65] R. Raghavan, "A model for spatially correlated radar clutter", *IEEE Transactions on Aerospace and Electronic Systems*, Vol. 27, No. 2, March 1991, pp. 268-275.

[66] P. Swerling, "Probability of Detection for Fluctuating Targets", *IEEE Transactions on Information Theory*, Vol. 6, No. 2, April 1960, pp. 269-308.

[67] N. Currie, R. Hayes and R. Trebits, *Millimeter Wave Radar Clutter*, Artech House, Norwood, USA, 1992.

[68] J. Billingsley, *Low Angle Radar Land Clutter: Measurements and Empirical Models*, William Andrew Publishing, Norwich, USA, 2002.

[69] M. Long, *Radar Reflectivity of Land and Sea, 3^{rd} edition*, Artech House, Norwood, USA, 2001.

[70] M. Stone and G. Banner, "Radars for the Detection and Tracking of Ballistic Missiles, Satellites and Planets", *Lincoln Laboratory Journal*, Vol. 12, No. 2, 2000, pp. 217-244.

[71] G. Minkler and J. Minkler, *CFAR*, magellan Book Company, Baltimore, USA, 1990.

[72] P. Gandhi and S. Kassam, "Analysis of CFAR Processors in homogeneous background", *IEEE Transactions on Aerospace and Electronic Systems*, Vol. 24, No. 4, July 1988, pp. 427-445.

[73] G. Alfano, A. De Maio and E. Conte, "Polarization diversity detection of distributed targets in compound Gaussian clutter", *IEEE Transactions on Aerospace and Electronic Systems*, Vol. 40, No. 2, April 2004, pp. 755-765.

[74] L. Novak, M. Sechtin and M. Cardullo, "Studies of target detection algorithms that use polarimetric radar data", *IEEE Transactions on Aerospace and Electronic Systems*, Vol. 25, No. 2, March 1989, pp. 150-165.

[75] V. Tuzlukov, *Signal Processing Noise*, CRC Press, Boca Raton, USA, 2002.

[76] P. Tsakalides, F. Trinic and C. Nikias, "Performance assessment of CFAR processors in Pearson-distributed clutter", *IEEE Transactions on Aerospace and Electronic Systems*, Vol. 36, No. 4, October 2000, pp. 1377-1386.

[77] R. Rifkin, "Analysis of CFAR performance in Weibull clutter", *IEEE Transactions on Aerospace and Electronic Systems*, Vol. 30, No. 2, April 1994, pp. 315-329.

[78] E. Al-Haussaini, "Performance of an ordered statistic CFAR processor in log-normal clutter", *Electroni Letters*, Vol. 24, No. 7, March 1988, pp. 424-425.

[79] J. Guan, Y. He and Y. Peng, "CFAR detection in K-distributed clutter", *Proceedings on Fourth International Conference on Signal Processing, ICSP'98*, Beijing, China, October 1998, pp. 12-16.

[80] B. Armstrong, "A comparison of conventional, adaptive and hybrid Doppler processing techniques", *Proceedings on COMSIG'92*, Cape Town, South Africa, September 1992, pp. 127-134.

[81] R. Schneider, *Modellierung der Wellenausbreitung für ein bildgebendes Kfz-Radar*, Dissertation for Dr.-Ing, Universität Fridericiana Karlsruhe, June 1998, pp. 6-10.

[82] A. Kosov, W. Randeu, H. Schreiber and D. Sculachev, "Ka-band Radar, Intended for Avalanche Detection and Monitoring", *Proceedings of European Microwave Week 2000*, Paris, France, October 2000, pp. 317-320.

[83] F. Ulaby, R. Moore and A. Fung, *Microwave Remote Sensing: Active and Passive,* vol.II, Artech House, Norwood, USA, 1982.

[84] Q. Wang and S. Gogineni, "A numerical procedure for recovering scattering coefficients from measurements with wide beam antennas", *IEEE Transactions on Geoscience and Remote Sensing*, Vol. 29, No. 5, May 1991, pp. 778-783.

[85] V. Richard, J. Kammerer and H. Wallace, "Rain backscatter measurements at millimeter wavelengths", *IEEE Transactions on Geoscience and Remote Sensing*, Vol. 26, No. 3, May 1988, pp. 244-252.

[86] J. Hyyppä, M. Mäkynen and M. Hallikainen, "Calibration accuracy of the HUTSCAT airborne scatterometer", *IEEE Transactions on Geoscience and Remote Sensing*, Vol. 37, No. 3, May 1999, pp. 1450-1454.

[87] B. Rode, "Early German experiments on radar backscattering of aircraft", Chapter 36 in *Radar Development to 1945* (R. Burns ed.), IEE Radar, Sonar, Navigation and Avionics Series 2, London, UK, 1988.

[88] N. Currie and E. Brown (eds.), *Principles and Applications of Millimeter-Wave Radar*, Artech House, Norwood, USA, 1987.

[89] P. Lecomte and W. Wagner, "ERS Wind Scatterometer Commissioning and in-flight Calibration", *Proceedings of a Joint ESA-Eumetsat Workshop on Emerging Scatterometer Applications - From Research to Operations*, Noordwijk, Netherlands, October 1998, pp. 261-270.

[90] K. Chet, C. Kuan and C. Teik, "Development of a ground-based radar fpr scattering measurements", *IEEE antennas and Propagation Magazine*, Vol. 45, No. 2, April 2003, pp. 36-42.

[91] F. Rostan, "The calibration of the MteOp/Advanced Scatterometer (ASCAT)", *Proceedings of the IEEE Geoscience and Remote Sensing Symposium, IGARSS 2000*, Vol. 5, Honolulu, USA, July 2000, pp. 2206-2208.

[92] J. Crispin and K. Siegel (eds.), *Methods of Radar Cross-Section Analysis*, Academic Press, New York, USA, 1968.

[93] I. Bahl and P. Bhartia, *Microwave Solid State Circuit Design*, John Wiley & Sons, New York, USA, 1988.

[94] G. Ferrara, F. Mattia and F. Posa, "Backscattering study on non-orthogonal trihedral corner reflectors", *IEE Proceedings on Microwaves, Antennas and Propagation*, Vol. 142, No. 6, December 1995, pp. 441-446.

[95] H. Eskelinen and P. Eskelinen, *Microwave Component Mechanics*, Artech House, Norwood, USA, 2003.

[96] M. Shimada, H. Oaku and M. Nakai, "SAR Calibration Using Frequency-Tunable Active Radar Calibrators", *IEEE Transactions on Geoscience and Remote Sensing*, Vol. 37, No. 1, January 1999, pp. 564-573.

[97] G. Kulemin, *Millimeter-Wave Radar Targets and Clutter*, Artech House, Norwood, USA, 2003.

[98] Y. Kuga, A. Nashashibi and F. Ulaby, "Clutter measurements by millimeter-wave radars", *Proceedings of Telesystems Conference 1991*, Vol. 1, Atlanta, USA, March 1991, pp. 347-351.

[99] B. Snuttjer and R. Narayanan, "Millimeter-wave backscatter measurements in support of surface navigation applications", *Proceedings of Geoscience and Remote Sensing Symposium 1996, IGARSS 96*, Vol. 1, Lincoln, USA, May 1996, pp. 506-508.

[100] T. Lane, C. Scheer and N. Currie, "An overview of MMW radar reflectivity", *Proceedings of IEEE National Radar Conference 1988*, Ann Arbor, USA, April 1988, pp. 235-240.

[101] N. Currie, J. Echard, M. Gary, A. Green, T. Lane and J. Trostel, "Millimeter-wave measurements and analysis of snow-covered ground", *IEEE Transactions on Geoscience and Remote Sensing*, Vol. 26, No. 3, May 1988, pp. 307-317.

[102] R. de Roo, F. Ulaby, A. El-Rouby and A. Nashashibi, "MMW radar scattering statistics of terrain at near grazing incidence", *IEEE Transactions on Aerospace and Electronic Systems*, Vol. 35, No. 3, July 1999, pp. 1010-1018.

[103] E. Baars and H. Essen, "Millimeter-wave backscatter measurements on snow-covered terrain", *IEEE Transactions on Geoscience and Remote Sensing*, Vol. 26, No. 3, May 1988, pp. 282-299.

[104] F. Ulaby, A. Nashashibi, et. al., "95-GHz scattering by terrain at near-grazing incidence", *IEEE Transactions on Antennas and Propagation*, Vol. 46, No. 1, January 1988, pp. 3-13.

[105] L. Williams, J. Gallagher, D. Sugden and R. Birnie, "Surface snow properties effect on millimeter-wave backscatter", *IEEE Transactions on Geoscience and Remote Sensing*, Vol. 26, No. 3, May 1988, pp. 300-306.

[106] F. Ulaby, P. Siquera, A. Nashashibi and K. Sarabandi, "Semi-empirical model for radar backscatter from snow at 35 and 95 GHz", *IEEE Transactions on Geoscience and Remote Sensing*, Vol. 34, No. 5, September 1996, pp. 1059-1065.

[107] U. Wegmuller and C. Matzler, "Rough bare soil reflectivity model", *IEEE Transactions on Geoscience and Remote Sensing*, Vol. 37, No. 3, May 1999, pp. 1391-1395.

[108] H. Kim, J. Johnson and H. Baertlein, "Ka band backscatter measurements and modeling of tree foliage", *Proceedings of Geoscience and Remote Sensing Symposium 1998, IGARSS 98*, Vol. 4, Jossain, July 1998, pp. 2086-2088.

[109] F. Ulaby and M. Dobson, *Handbook of Radar Scattering Statistics for Terrain*, Artech House, Norwood, USA, 1989.

[110] P. Lombardo and J. Billingsley, "A new model for the Doppler spectrum of wind-blown radar ground clutter", *Proceedings of IEEE Radar Conference 1999*, Boston, USA, April 1999, pp. 142-147.

[111] P. Eskelinen, *Introduction to RF Equipment and System Design*, Artech House, Norwood, USA, 2004.

[112] E. Knott, K. Shafer and M. Tuley, *Radar Cross Section*, Artech House, Norwood, USA, 1985.

[113] S. Gorshkov, S. Leschenko, V. Orlenko, S. Sedyshev and Y. Shirman, *Radar Target Backscattering Simulation, Software and User's Manual*, Artech House, Norwood, USA, 2002.

[114] J. Säily, *Instrumentation of a submillimeter wave hologram compact antenna test range*, Dissertation for the degree of Doctor of Science in Technology, Helsinki University of Technology, Radio Laboratory, 2003.

[115] C. ZhiPing, Z Qi and X. Shan-Jia, "Experiment research on MM wavelength radar absorbing materials", *IEEE Antennas and Propagation Society International Symposium*, Vol. 3, July 1999, pp. 1970-1973.

[116] G. Biegel, H. Essen and D. Nüßler, "Validation of RCS Signature Simulations of Ground Targets at Millimeter Wave Frequencies", *Proceedings of International Radar Symposium IRS 98*, Vol. 1, Munich, Germany, September 1998, pp. 413-420.

[117] S. Milch and M. Behrens, "Pedestrian Detection with Radar and Computer Vision", http://www.smartmicro.de/Pedestrian_Detection.pdf, 7 pages. (16.4.2005).

[118] N. Yamada, Y. Tanaka and K. Nishikawa, "Radar cross section for human body in 76 GHz band", *Proceedings of IEICE General Conference*, Tokyo, Japan, March 2004, B-1-26, 6 pages.

[119] M. Sachidananda and D. Zrnic, "Clutter Filtering and Spectral Moment Estimation for Doppler Weather Radars Using Staggered Pulse Repetition Time", *Journal of Atmospheric and Oceanic Technology*, Vol. 17, No. 5, May 2000, pp. 323-331.